Nonlinear Dynamics in Superconducting Stripline Resonators and Interference Devices

Baleegh Abdo

Nonlinear Dynamics in Superconducting Stripline Resonators and Interference Devices

Research Thesis

In Partial Fulfillment of the
Requirements for the
Degree of Doctor of Philosophy

Baleegh Abdo

Submitted to the Senate of
the Technion - Israel Institute of Technology

Eiar,5770 Haifa May, 2009

This Research Was Done Under The Supervision of Prof. Eyal Buks in the Department of Electrical Engineering

The Generous Financial Help of the Technion and the Ministry of Science, Culture and Sports is Gratefully Acknowledged

I would like to express my deep gratitude to my advisor Prof. Eyal Buks for the continuous support, the valuable knowledge, the deep scientific insight, and the enormous dedication.

Many thanks are owed also:

To Prof. Miles Blencowe, Prof. Levi Schächter and Prof. Gadi Eisenstein for fruitful discussions and generous support.

To our highly skilled and innovative lab engineers from whom I learned a lot: Oleg Shtempluck and Valery Kochetkov.

To my colleagues who have contributed tremendously to the success of this work: Eran Segev, Oren Suchoi and Gil Bachar.

To Stav Saitsev, Fei Xue and Daniel Berman for inspiring scientific discussions and casual talks.

To my eldest brother Hisham for his ongoing encouragement and friendship along the way.

And to all who contributed to this work and were not mentioned.

Dedication

To my beloved mother Nohad and to the memory of my late father Sami

Contents

List of Figures

Chapter 1

Introduction

1.1 Superconductors

Low surface resistance, high power density, low losses at microwave frequencies, and high quality factors are only a partial list of extraordinary electrical properties that superconductors possess, and which make them superior candidates over normal metals, in a wide range of high performance RF applications.

The discovery of high temperature superconductors (HTS) materials in 1986 had not only enhanced this technological trend and made many applications feasible in less cost and maintenance effort, but it also had succeeded to draw a renewed research attention to the superconducting phenomena in general and to nonlinear effects in superconductors in particular.

Nonlinear effects in superconductors can play a negative or positive role depending on the purpose of the application. Whereas passive RF devices suffer from degradation of performance as a result of nonlinear effects, some active parametric devices on the contrary benefit from them.

Furthermore, a medium is considered nonlinear in case its physical properties become amplitude dependent. As such superconductors are considered nonlinear, as their electrical properties (i.e. the resistance and inductance) are rf current dependent due to Meissner effect which is a fundamental property of superconductors.

Nonlinear behavior in superconductors can be dominated by intrinsic or extrinsic effects depending on the method of deposition, superconductor structure and the operating conditions.

Moreover, in contrast to extrinsic effects which can be minimized by improving the material quality, intrinsic effects which are geometry and deposition dependent can be minimized only to a certain level. Hence, setting many times a least limit to nonlinearity expected from superconductor devices [1].

1.2 Applications

1.2.1 General Review

Superconductors along the years have found their way to a wide range of fields and into various highly accurate, sensitive devices such as strong low power magnets, magnet monopole detectors, flux memory elements [2], kinetic inductance memory cells [3], ultra fast single photon detectors in the infra red [4], high Q resonators for material characterization and filtering [5],[6], low loss and high isolation Nb circulators [7], NbN delay lines [8],[9], and also serve as a coating for accelerating rf cavities [10].

The dramatic discovery of HTS in 1986 intensified this trend and promoted many new practical applications. HTS have been used to implement digital devices as reported in Refs. [11],[12], and are expected to replace passive normal metal microwave devices for wireless communication systems in the future[1] [13].

Examples of such RF devices include: high performance bandpass filters with low insertion loss [14],[15],[16], HTS microstrip patch antennas [17],[18], HTS coplanar waveguides with lower transmission losses than metal layers [19], low loss and high performance YBCO ferrite phase shifters for radar applications.

1.2.2 Applications Based on Nonlinear Effects

Among the devices that are based on nonlinear effects of superconductors - in addition to those which were mentioned previously such as photon detectors- there are the Josephson junction device, the parametric-gain superconductor resonator and the parametric phase-sensitive amplifier.

Whereas the Josephson junction is one of the leading candidates for the implementation of the so called quantum bit (qubit) in quantum computa-

[1] Such as cellular and satellite communication systems.

tion(QC) [20],[21], the parametric-gain superconductor resonator is one of the strong candidates for the purpose of coupling and reading out these qubits.

Parametric phase-sensitive amplifiers on the other hand can potentially exceed the so-called *standard quantum limit* imposed on the noise level of phase-insensitive amplifiers [22, 23]. Such devices may allow the generation of quantum squeezed states of the electromagnetic field, in which the noise in one amplitude component is reduced below that of vacuum fluctuations [24].

1.3 Nonlinear Effects Reported in the Literature

Most of the superconducting devices and applications mentioned in (1.2.1) suffer from performance degradation as a result of nonlinear effects such as power dependency that limits the maximum power level injected, harmonic generation, intermodulation distortion, resonance skew and nonlinear dissipation. Hence, these undesired nonlinear side-effects of superconductors have been the subject of a large number of intensive studies which aimed mainly to achieve four objectives:

1. Reveal the origins of nonlinear effects in superconductors.
2. Identify the dominant factors that increase these effects.
3. Propose theoretical models that explain the underlying mechanisms of nonlinear behavior observed in superconductors.
4. Explore ways to overcome and minimize these effects.

Despite the intensive experimental efforts and the various theoretical models proposed to date there is still no comprehensive coherent picture as to the origins of nonlinear behavior in superconductors, this is partially because:

1. There are multiple non-linear mechanisms which make generalization very difficult. Among the various nonlinear sources one can name: intrinsic nonlinearity, pair-breaking, defect points, damaged edges, substrate material, weak links, designed or naturally occurring Josephson

junctions, global and local heating effects, rf and dc vortex penetration and motion.

2. There are a variety of preparation and characterization techniques employed by different groups which prevent direct comparisons between different samples and effects.

One of the important models which accounts for some of the nonlinear effects is the weak link model. A novel study on weak links, point defects , insulating planes, vortex penetration, fluxoid motion and other nonlinear mechanisms in granular superconductors was conducted by Halbritter [25],[26]. Rf residual surface resistance was presented therein as well, as a figure of merit for the homogeneity of superconducting surfaces [25].

In Ref. [27] Golosovsky *et al.* examined nonlinear microwave properties of superconducting Nb microstrip resonators and applied a dimensionless parameter $r = \Delta R_s(P)/\Delta X_s(P)$ in order to identify the dominant nonlinear mechanism (where P corresponds to the input power and R_s, X_s correspond to the real and imaginary parts of the surface impedance of the microstrip respectively). The r parameter was also employed as a characteristic signature for the different nonlinear mechanisms in Ref. [28].

Additional important contributions which can be mentioned in this context include:

1. Generalizing the concept of complex conductivity in order to describe nonlinear behavior of superconductors [29].

2. Providing an explanation for the rf superconducting properties and electrical resistivities of reactively sputtered NbN, in terms of NbN columnar structure and material composition [30],[31],[32].

3. Suggesting a simple model which accounts for microwave losses in thin superconducting films caused by columnar defects [33].

4. Proposing a coupled grain model which employs the Josephson Junction effect in order to explain extrinsic effects [34], [35]. Followed by a generalized coupled grain model proposed in Ref. [36].

5. Interesting attempts to verify the theoretical models which attribute nonlinear effects to weak links functioning as built-in Josephson junctions, have been carried out in Refs. [37],[38]. In these references, the

authors embedded a small Josephson junction at the middle of a half wave YBCO stripline, and exploited the fact that the first mode has a maximum effect on the Josephson junction while the second mode has a negligible effect, in order to differentiate the properties of the junction from those of the film. A similar technique was applied in Ref. [39] but instead of a Josephson junction, a grain boundary was grown in the middle of the resonator and the influence of the grain boundary angle was studied.

6. The nonlinear Meissner effect (NLME) (being an intrinsic effect) was discussed by Yip *et al.* in 1992 [40] and also by T. Dahm *et al.* in 1997 [41] and 1999 [42]. In the former publication Dahm *et al.* applied intermodulation theory to HTS microstrip resonators dominated by NLME, whereas in the latter publication, the authors investigated the nonlinear current response under NLME. Observation of this nonlinear effect in YBCO thin films was reported in Ref. [43].

1.3.1 Duffing nonlinearity

Duffing-like nonlinearity which is characterized by skewed resonance curves, pronounced shift of resonance frequency and hysteresis behavior has been studied and reported by several research groups. Back in 1970, Halbritter [44] developed a perturbation theory which solves Maxwell equations in the nonlinear limit in an attempt to explain Duffing-like nonlinearity observed in superconductor resonators.

A nonlinear transmission line model for superconducting resonators exhibiting Duffing nonlinear behavior was introduced in Refs. [45],[46].

Moreover, the Duffing-like behavior was observed in different superconducting resonators employing different geometries and materials, it was observed in a HTS parallel plate resonator [47], in a Nb microstrip resonator [48], in a Nb and NbN stripline resonators [49], in a YBCO coplanar-waveguide resonator [50], in a YBCO thin film dielectric cavity [51], and also in a suspended HTS thin film resonator [52].

To account for the Duffing-like nonlinearities which were observed in Ref. [47] and Ref. [48]. Numerous heating models were successfully developed therein. Transient and steady states of the nonlinear response were further examined in Ref. [51]. In addition, weak link theory was employed to explain the Duffing-like nonlinearity observed in Ref. [49] and was shown to be

consistent with the experiments.

Extrinsic effects such as grain boundaries were found to govern the characteristics of relatively high power behavior of YBCO resonators in Ref. [50]. Saturation of intermodulation products were reported also as an additional sign of strong nonlinearity [50].

Intensive effort was invested as well in extending microwave performance to higher powers by means of (1) studying the influence of impurity doping and varying oxygen content on nonlinear effects in YBCO films [53],[54], (2) investigating the influence of the substrate and its topography on the nonlinear behavior [55],[56], and also (3) by developing the fabrication process and tuning relevant parameters [57],[58].

Other nonlinear effects were reported by Portis *et al.* [17] where they observed frequency hysteresis behavior and notches that develop on both sides of the frequency response curve of their HTS microstrip patch antenna above certain incident power level accompanied by resonance frequency shift and Q factor decrease. Similar results were reported also by Hedges *et al.* [59] in their YBCO stripline resonator, and by Wosik *et al.* [60] in their thin YBCO film dielectric cavity. All three studies attributed the observed nonlinear behavior to abrupt changes in the resistive loss of weak links, thermal quenching and weak link switching to normal state.

1.4 Nonlinear Effects

Nonlinear effects have significant implications on various fields of science and technology. To some extent, the stronger the nonlinearity is, the greater is its potential applications.

In the first part of our research, we study superconducting stripline resonators with emphasis on nonlinear effects. The nonlinear effects measured in our resonators are relatively strong. As described in Refs. [61, 62, 63, 64, 65, 66, 67], our measurements reveal some novel nonlinear effects such as power and frequency hysteresis, nonlinear coupling, high intermodulation gain and self-modulations.

1.5 Intermodulation Amplifier

Intermodulation measurement is considered one of the effective tools for the detection and characterization of nonlinear effects in superconductors working in the microwave domain [41, 68].

In a standard intermodulation measurement two equal tones at frequencies f_1 and f_2 which fall within the resonance bandwidth, are injected into the resonator. Due to the nonlinearity of the device, frequency mixing occurs and new signals are generated at $nf_1 + mf_2$ where n and m are integers (the order of each harmonic is determined by the sum $|n| + |m|$). The signals generated at frequencies $2f_1 - f_2$, $2f_2 - f_1$ (corresponding to the third order) are called the idler, and usually standard intermodulation analysis focus on them.

In our intermodulation measurements, however, following the IMD theoretical predictions in manuscript [69], we inject unequal tones, one intense field referred to as pump at f_p, and one small amplitude tone referred to as signal at $f_p + f$, where f corresponds to a small frequency offset, whereas the output idler tone is generated at $f_p - f$.

In our measurements [63] we demonstrate how our nonlinear NbN superconducting resonators can serve, under certain conditions in the vicinity of a bifurcation point, as intermodulation amplifiers.

1.6 Self-Sustained Modulations

"Self-sustained-modulations" is a fascinating novel nonlinear effect observed in our nonlinear superconducting resonators. A thorough and comprehensive study of this effect both in the time and frequency domain has been carried out by our group in Refs. [65, 66, 67]. However, all published results were measured in NbN superconducting stripline resonators incorporating microbridges. In this section, in contrast, we show some unpublished results measured in our NbN superconducting stripline resonators containing naturally grown weak-links residing at the boundaries of the columnar structure of NbN films [62].

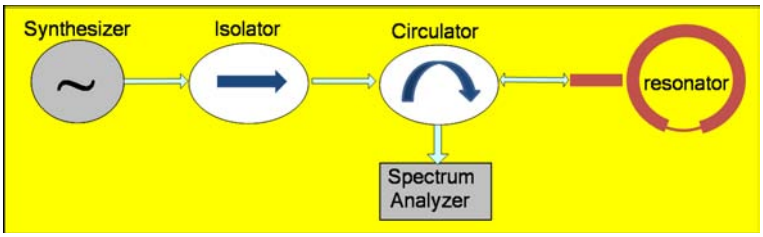

Figure 1.1: A basic self-modulations measurement setup.

1.6.1 A brief background

The phenomenon of self-sustained modulations can be explained in the following manner: Due to the dependence of the stored energy inside the resonator on the resonance frequencies and the damping rates of the resonator, and the dependence of both these parameters on the impedance of the weak link, the system may have, in general, up to two locally-stable steady-states, corresponding to the superconducting (SC) and normal conducting (NC) phases of the weak link (see manuscript [67]). The stability of each of these phases depends on both the power and frequency parameters of the injected pump tone. In general there exist four different stability zones (please refer to Fig. 4 [70] and Fig. 3 [67]). Two are monostable zones, where either the SC phase or the NC phase is locally stable. Another is a bistable zone, where both phases are locally stable. The third is an astable zone, where none of the phases are locally stable. Consequently, when the resonator is biased into the latter zone, the weak link is expected to oscillate between the two phases. As the reflection coefficient of the resonator differs significantly between these two phases, the oscillations translate into self-modulations (SM) of the reflected pump tone. The onset of this instability, namely the bifurcation threshold (BT), is defined as the boundary of the astable zone.

1.6.2 Experimental Setup

The SM experiments are performed while the devices are fully immersed in liquid Helium. The basic experimental setup, used for the SM experiments, is schematically depicted in Fig. 1.1. The resonator is stimulated with a single monochromatic pump tone, and the reflected power off the resonator is measured with a spectrum analyzer.

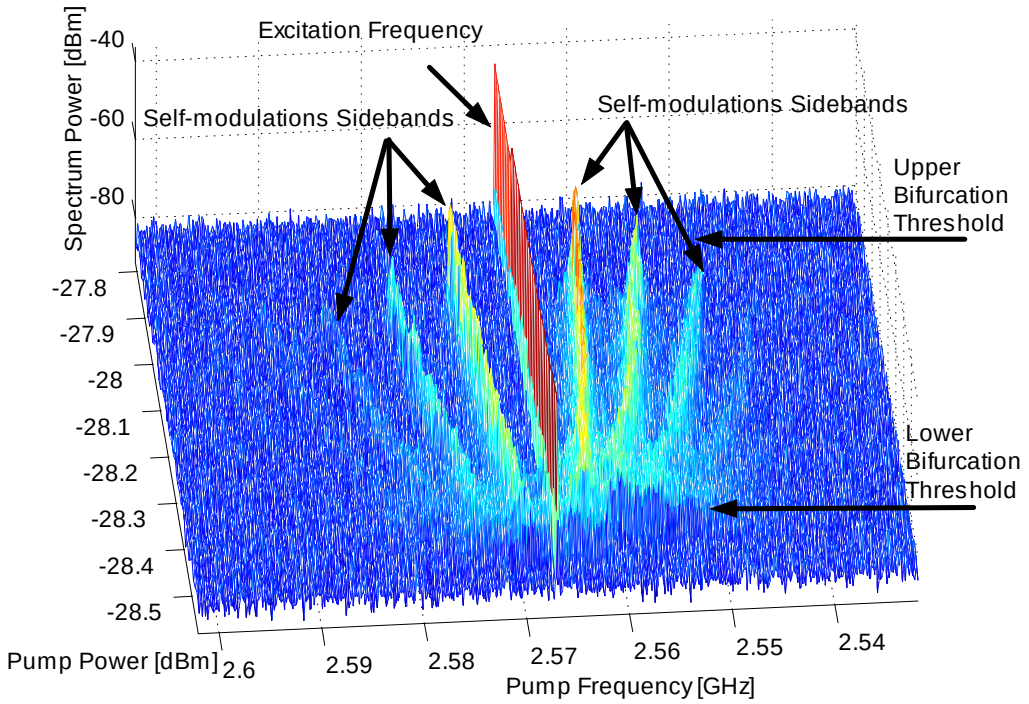

Figure 1.2: Typical experimental result of SM phenomenon in the frequency domain as a function of pump power. The excitation frequency is 2.567 GHz. The plot shows also the existence of two bifurcation thresholds.

1.6.3 Typical Measurement Results

A typical SM measurement is shown in Fig. 1.2 (for a certain device). At "low" input pump powers, approximately below -28.4 dBm, and at "high" input powers, approximately above -27.9 dBm, the response of the resonator is linear, namely, the reflected power off the resonator contains a single spectral component located at the frequency of the stimulating pump tone. Between these regions, there exists a narrow power range, in which SM of the reflected power off the resonator occur. The SM frequency, defined as the frequency difference between the pump and the primary sideband, increases as the pump power increases.

This fact is also manifested in Fig. 1.3 where SM frequency is drawn as a

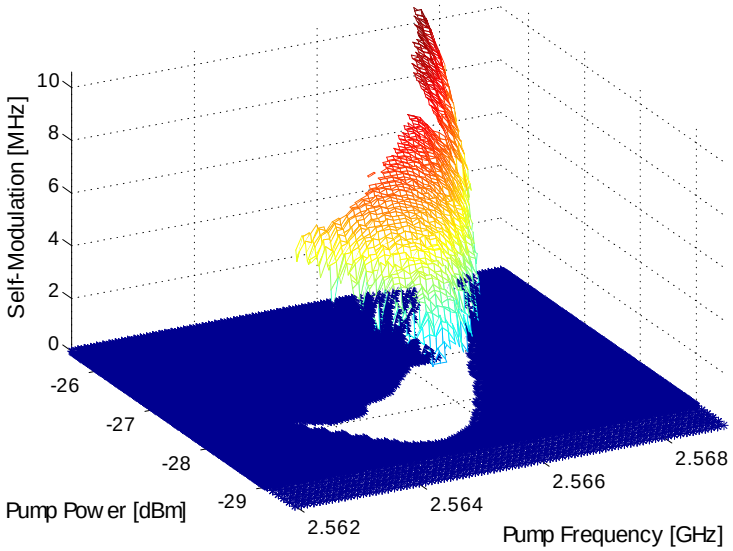

Figure 1.3: SM frequency as a function of pump power and pump frequency corresponding to the fundamental mode of the resonator.

function of the pump power and the pump frequency, outlining visually the boundaries of the astability zone. Furthermore, as can be seen in the Fig. 1.3 and Ref. [67] the SM can extend for tens of megahertz on both sides of the resonance frequency.

1.7 Stochastic Resonance

Stochastic resonance (SR) is another nonlinear effect that we have succeeded to demonstrate in our superconducting stripline resonators. In its simple form stochastic resonance implies that a certain amount of white noise can appreciably amplify small periodic modulating signals acting on bistable systems. As a result, one of the distinguished fingerprints of SR phenomenon is a peak observed in the signal to noise ratio (SNR) curve as a function of the input noise intensity, corresponding to some nonzero noise intensity. This counterintuitive amplification in SNR curve is generally explained in terms of a coherent interaction between the modulating signal and the stochastic

noise entering the system [71].

To elucidate this concept further, consider a double well potential which corresponds to some metastable system (Fig. 1.4). If one applies a small modulating force to the system, the double well potential would be tilted periodically towards one of the wells. Naturally, the system in each half cycle would prefer to be at the minimum energy state, but this is not necessarily the case due to the presence of a potential barrier. However, with the addition of white noise hopping events from one well to another become possible. In case the noise intensity is "low", the hopping events are rare and as such they are not synchronized with the modulating signal. Conversely, in case the noise intensity is "large", the hopping events become frequent and consequently screen the modulating signal. Whereas, for a certain amount of noise (D_{SR}) in the "intermediate" range, corresponding to one hopping event each half cycle, the noise is synchronized with the modulating signal and consequently a peak in the SNR is attained.

Thus, in general, *stochastic resonance* occurs when the frequency of the deterministic periodic signal ($\Omega/2\pi$) modulating the double-well potential of the system matches half the hopping rate between the bistable states $\Gamma(D)$, where D measures the intensity of the noise (assumed to be zero-mean, white Gaussian noise). That is $\Omega = \pi\Gamma(D_{\mathrm{SR}})$. In other words, during each half time cycle of the drive ($T_\Omega = 2\pi/\Omega$) a single noise-induced hopping event takes place,

$$T_\Omega/2 = \Gamma^{-1}(D_{\mathrm{SR}})$$

which is usually referred to as the *time-scale matching condition* for stochastic resonance, where $\Gamma(D)$ in general follows a Krammars-like transition rate of the form:

$$\Gamma(D) = \Gamma_0 \exp(-\frac{\Delta V}{D})$$

where ΔV is the height of the potential barrier separating the two bistable states, and Γ_0 is the attempt rate.

Further details on the subject and a broader survey can be found in the attached copies of Refs. [70, 72, 73], and also in the discussion chapter. However, it is worthwhile pointing out in this regard that SR phenomenon is not limited to classical systems or classical noise, but it also applies in principle to semiclassical and quantum systems. In fact there have been

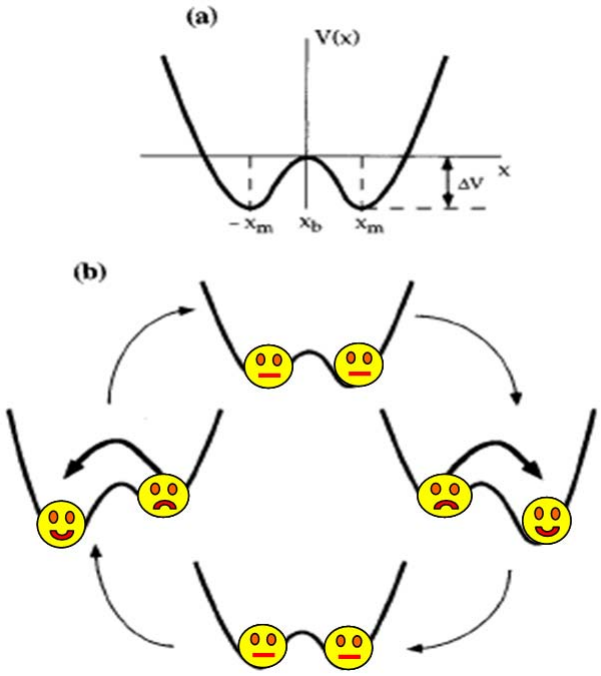

Figure 1.4: Illustration describing stochastic resonance in a metastable system with a symmetric double well. (a) A sketch of the double-well potential. The minima are located at $\pm x_m$ whereas the two wells are separated by a potential barrier ΔV. (b) A cartoon showing a cyclic variation of the double-well potential. In the presence of periodic driving, the double-well potential is tilted back and forth, thereby raising and lowering successively the potential barriers of the right and the left well, respectively. A suitable dose of noise (i.e., when the period of the driving approximately equals twice the noise-induced escape time) will make the "sad face" happy by allowing synchronized hopping to the globally stable state (strictly speaking, this holds true only in the statistical average). After L. Gammaitoni *et al.* [71].

numerous attempts recently in order to generalize SR effect and possibly extend it to the quantum realm [74, 75]. Interestingly, one of these recent studies deals with SR phenomena in qubit arrays [76].

1.8 Escape Rate of Metastable States

Escape rate theory plays a key role in explaining the behavior of various metastable systems in nature [77]. Ranging from biology to chemistry, physics [78, 79] and engineering.

Likewise, in our research we study the phenomenon of noise-assisted escape rate of metastable states in a driven superconducting microwave resonator due to thermal instability. Interestingly, some of the derived predictions are quite unique.

For further details on the subject and a broader survey please refer to the attached copy of our manuscript [72].

1.9 Intermodulation and Parametric Amplification

Recently, there has been a renewed and broad interest in the area of parametric and intermodulation amplifiers based on Josephson junctions. Pioneering work in this field has been conducted by B. Yurke and his collaborators at Bell laboratories in the late eighties and early nineties [23, 24, 80], where the authors demonstrated for the first time thermal and vacuum noise squeezing using a Josephson parametric amplifier (JPA), which consisted of a dc-SQUID connected to two superconducting transmission lines and an LC resonator in parallel. To date, various configurations and novel implementations of such amplifiers have been realized and tested. Among these variations one can name briefly, a series array of 1000 Josephson junctions embedded in a coplanar waveguide [81], a lumped element dc-SQUID inductively coupled to a quarter wave resonator [82], a superconducting coplanar-waveguide resonator terminated by a dc-SQUID [83] and a coplanar waveguide transmission line whose center conductor is composed of a series array of dc-SQUIDs [84, 85].

A large part of the renewed and growing interest in such amplifiers can be attributed mainly to two high-profile developments that occurred in recent

years namely, the capability to read out the quantum state of a superconducting qubit, and detect the position of a nanomechanical resonator both using microwave photons.

1.9.1 Figures of merit

The figures of merit commonly used to characterize amplification schemes in general, and phase sensitive amplifiers in particular can be summarized as follows:

1. **Gain:** characterizes the amplification ratio between the signal at the output and the signal at the input.

2. **Bandwidth:** the frequency range over which the amplifier gain is considerable (usually the reference gain corresponds to 3 dB below the maximum gain). In practice, this figure of merit is extracted by measuring the gain as a function of the frequency offset applied between the pump and the signal. In the case of a resonance amplifier this quantity coincides to a large extent with the linewidth of the resonance.

3. **Dynamic range:** conventionally this merit refers to the input power range over which a given amplifier operates as desired. In the case of an intermodulation or parametric amplifier, this parameter corresponds to limits set on the order of magnitude of the signal power with respect to the pump power. Usually above certain value of the signal, the gain is suppressed.

4. **Resonance tunability:** in the case of a resonator implementation, one way to enlarge the bandwidth of the device is via achieving resonance frequency tunability. In Ref. [84] for example where the central strip is comprised of a series of dc-SQUIDs, the resonance frequency is adjusted via external magnetic flux by about 4 GHz (between 4 and 7.8 GHz).

5. **Added internal noise:** this parameter represents the amount of noise which the amplifier itself generates inherently and adds to the circuit.

6. **Back-reaction:** basically this quantifies the undesired impact of the amplifier on the input. In the ideal case back-reaction is zero, that is the amplifier does not interfere with the input or destroy/demolish the quantum state. However, this requirement is not possible, thus large

efforts are invested in minimizing this quantity as much as possible. To a large extent, this figure of merit is still considered an open question with respect to various amplification schemes.

Moreover, the main advantages of a JPA are: (1) it provides a considerable gain, (2) operates close to the quantum limit (much better than any HEMT or semiconductor based amplifier), (3) allows phase sensitive amplification.

Whereas, the main disadvantages of a JPA are: (1) it has a narrow-band in frequency, (2) has a relatively small dynamic range.

1.10 Intermode Coupling

Large and intensive efforts have been invested in the course of this work in an attempt to couple a flux-qubit made of aluminum to a superconducting resonator made of niobium/aluminum [2], where the superconducting resonator plays the role of a cavity quantum electrodynamics, while the flux-qubit - being essentially a two-level system- mimics the behavior of an artificial atom [86].

The motivation for realizing such integrated systems is two-fold: first, in this configuration it can be shown theoretically [87, 88, 89] that by driving the resonator externally with a detector signal coupled to the qubit (non-resonantly, but rather via a maxima location of the magnetic field of the fundamental mode), the effective resonance frequency which can be measured by monitoring the resonance response depends strongly on the state of the qubit. Thereby, providing in principle a non-destructive readout scheme for the state of the qubit; second, by introducing a "small" probe signal to the resonator which is also strongly coupled to the qubit inductively but at a different resonance frequency, it can be shown by analyzing the coupled system that a single photon added to the signal mode results in a shift in the effective resonance frequency of the detector mode [87, 89, 90]. Hence, allowing in principle performing a quantum non-demolition measurement of discrete Fock states (the photon number) of the resonator in the microwave domain [90, 91].

To that end, several integrated systems have been fabricated and tested in our lab using a variety of methods. However, in spite of the intensive

[2] For more details on the subject please refer to the fabrication section.

efforts invested in this area, the fabricated devices did not yield significant results for various reasons.

Nevertheless, we have successfully demonstrated recently intermode coupling and intermode dephasing in a superconducting stripline resonator integrated with a nano-bridge dc-SQUID [92]. Mainly due to two significant advantages of such integrated system: (1) the dc-SQUID has a flux degree of freedom which can be utilized in order to maximize and minimize its nonlinear response, (2) the Kerr-like nonlinearity exhibited by the dc-SQUID, despite being a Duffing nonlinearity, is quite suitable for the purpose of controlled intermode coupling and dephasing [90, 92].

Chapter 2

Experimental Setup

2.1 Stripline Geometry

The resonators were designed and assembled in a standard stripline geometry [1].

The dielectric substrates used were either (1) sapphire (34 mm X 30 mm X 1 mm) which are known for their high chemical stability, mechanical strength and low loss tangent at microwave frequencies [18], or (2) high resistivity silicon wafers (34 mm X 30 mm X 0.5 mm) coated with a 100 nm layer of SiN on both sides.

All of the superconducting resonators measured were housed inside a gold plated oxygen-free high conductivity (OFHC) copper Faraday cases.

The superconducting resonators were either dc-magnetron sputtered (Nb and NbN) or evaporated (Aluminum) on one of the dielectric substrates of the stripline configuration, whereas the superconducting ground planes were sputtered on the inner covers of the OFHC cases.

Microwave power signals are fed to the resonators via SMA launchers which are SMA female connectors from the outside and spring-like feed-lines from the inside which are pressed against the feedlines of the resonator [93].

[1] Please see schematic cross section shown in Fig. 1 Ref. [62].

2.2 The Cryogenic Setups Used

In the course of our work we have used three different cryogenic setups depending on the device and the application:

1. The resonator case was connected by its input to a 0.142" semi-rigid coax cable and immersed into liquid helium contained in a Cryofab dewar. In this configuration the ambient temperature is 4.2 K.

2. The resonator case was mounted on a sample holder of a homemade insert [2] which was pumped and immersed into liquid helium bath contained in an Oxford instruments dewar. A setup configuration which enabled both varying the ambient temperature and applying magnetic field.

3. In order to operate and measure the integrated systems consisting of a superconducting resonator (Nb/Al) and a (dc/rf) SQUID made of aluminum, ultra-low temperatures are required ($T \ll T_c \simeq 1.2\,\mathrm{K}$). Thus a large part of the work has been carried out using a dilution refrigerator (a digital photo of the system is enclosed, see Fig. 2.1).

2.2.1 Thermal noise reduction overview

To minimize thermal noise entering the system, special care should be taken in heat sinking and filtering all dc control lines. For this purpose, three possible techniques may be applied in addition to low pass filtering at room temperature. One is using powder filters, which are known to be effective in attenuating broadband noise [94]. The second is using microstrip filters implemented on a dielectric substrate via photolithography [95]. The third is using lossy heat sinked coaxial cables incorporated in the dilution system in order to carry dc.

An adequate heat sinking should be applied to the microwave semi-rigid cables as well. One way is establishing a good physical contact between the outer conductor of the semi-rigid cables and the sample holder at each stage. Another way is incorporating properly-heat-sinked directional couplers along the microwave input path.

[2] For further details on the design and ingredients of this insert please refer to my master's thesis.

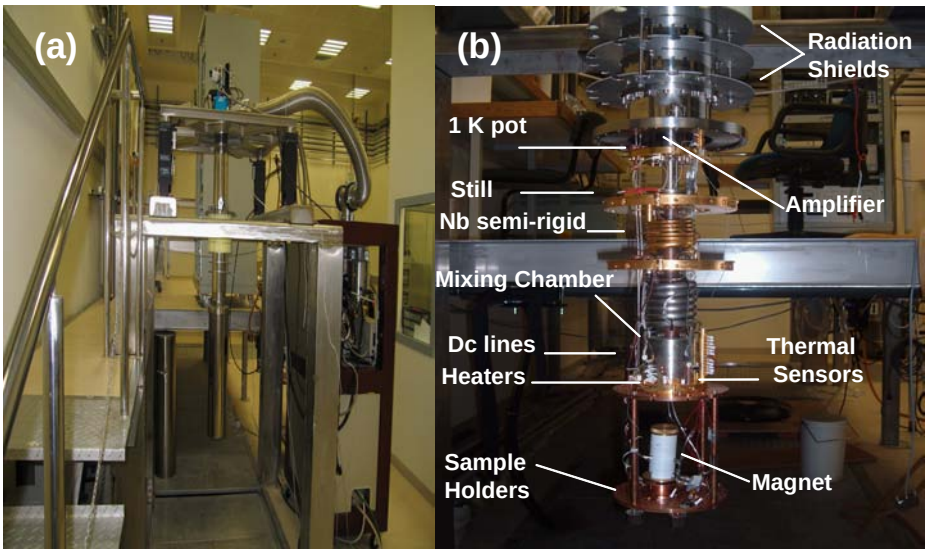

Figure 2.1: Digital photographs taken at our lab (a) Dilution refrigerator. (b) Dilution insert.

In case further heat sinking is needed for the inner conductor of the semi-rigid as well, a short section of the outer conductor and the dielectric layer of the semi-rigid can be stripped away and filled instead with epoxy, that is in order to enhance the heat conductance between the stage and the inner conductor [96].

Chapter 3

Fabrication Process

3.1 Niobium Nitride stripline resonators

The fabrication process of our NbN superconducting stripline resonators consists of five main steps:

1. **Cleaning:** The sapphires were subjected to **Pirrana** and **RCA** cleaning processes for 10 minutes each.

2. **Sputtering:** The sputtering was done using a TFSP-448 DC magnetron sputtering system. The distance between the Nb target and the sapphire was set to about 80 mm. All resonators were deposited near room temperature following the footsteps of Refs. [97],[98],[99], no external heating was applied, but it is quite reasonable to assume that the substrate temperature reached about 90 °C or 100 °C during sputtering due to plasma heating and discharge process. The system was usually pumped down -prior to sputtering- to $3 - 8 \cdot 10^{-8}$ torr base pressure (achieved overnight). The sputtering was done in Ar/N_2 atmosphere [100], the relative flow ratio of the two gases into the chamber and the total pressure of the mixture were controlled by mass flow meters and a variable throttle valve on the cryogenic pump. The sputtering usually started with a two minute presputtering at the selected plasma conditions before removing the shutter and depositing on the substrate. The deposition rate was monitored using a Xtal crystal, the total film thickness was determined by the deposition rate, deposition

time and an appropriate tooling factor. Following deposition the wafers were usually left to cool down for about 10 minutes before they were removed from the chamber.

3. **Photo-Lithography:** First the sheet resistance of the sputtered films were measured by Veeco fpp-5000 four-point probe in room temperature. After cleaning the sapphire with methanol and DI water, it was baked for 10 minutes on a 250 °C plate to enhance the surface adhesion of the NbN before applying 4533 positive photo-resist at 4500 rpm for 60 s. Following photo-resist spinning, the sapphire was prebaked in the oven at 90 °C for 10 min to dry out the photo-resist before photo-lithography. The photo-lithography was done using MJB3 mask-aligner with exposure time set to 12.5 s. Afterwards the photo-resist was developed using 326 developer for 30 s or alternatively 312 developer. To harden the photo-resist so that it can be used as a protective mask during ion-milling, the sapphire was post-baked in the oven at temperature 90 °C for an extra 30 - 40 min.

4. **Ion-milling:** The redundant NbN not covered by the photo-resist mask was etched using Ar ion-milling. During the process the sapphire was clamped to a rotating stage to ensure uniform etching. The process duration was mainly set by a trial and error process.

5. **Photo-resist stripping:** To strip the photo-resist mask used in ion-milling and expose the patterned resonator, the sapphire was immersed in NMP solution at 140 °C for 30 min, and afterwards exposed to high flow of acetone gas.

3.2 Aluminum resonators integrated with a dc-SQUID

We describe herein in more detail the fabrication process employed in order to implement Al resonator coupled to a dc-SQUID (described and measured in manuscript [101]).

The device is implemented on a high-resistivity 34 mm X 30 mm X 0.5 mm silicon wafer coated with a 100 nm thick layer of SiN. As a preliminary step and in order to enhance electrical contact to rf-launchers, thick gold pads (300 nm) are realized at the peripheral of the wafer. This is achieved using a

three-stage process which consists of UV lithography, gold evaporation and lift-off. Subsequently, three layers of PMMA (2 layers of 495/A6 and one of 950/A2) with a total thickness of 700 nm are spined and baked alternately. Following this step, e-beam lithography is applied in which both the macroscopic resonator and the microscopic Josephson gaps are written at the same session. Following a developing stage, a two angle shadow evaporation of aluminium [102] -with an intermediate stage of oxidation- implements the resonator as well as the two $Al/AlO_x/Al$ Josephson junctions comprising the dc-SQUID. The total thickness of the aluminium evaporated is 80 nm (40 nm at angles $\pm 36^0$ relative to the perpendicular of the substrate). Whereas the tunneling barrier of the junctions is formed by applying a gas mixture of argon (80%) and oxygen (20%) at a pressure of 26 m torr for 12 minutes. Finally a lift-off process concludes the fabrication of the integrated system.

3.2.1 E-beam lithography in more detail

Two different magnifications were applied during the e-beam lithography of the devices, magnification 35 for the macroscopic sections of the resonator and magnification 500 for the SQUID. Moreover, three calibration processes were carried out prior to each lithography process (1) calibration of the motor in relative to the sample, (2) calibration of magnification 35, (3) calibration of magnification 500. The calibrations were done on fixed gold crosses implemented on the wafer in a preliminary step. Each calibration yielded four parameters, a stretch parameter, a rotation angle and x-y offsets and ultimately all these parameters were taken into account in the final program file automating the process. The e-beam current applied in the lithography of the macroscopic and microscopic sections was 7 nA and 50 p A respectively.

3.2.2 Negative resist recipe for gold pads

1. Baking on a 110 °C hot plate for 10 min.
2. Coating the sample with AZ5214E negative photo-resist at 5000 rpm for 60 s.
3. Pre-baking on a 110 °C hot plate for 60 s.
4. UV lithography using chrome mask. Exposure time in the range 1.9-2.2 s.

5. Post-baking on a 125 °C hot plate for 120 s.
6. UV lithography without any mask. Exposure time 8 s.
7. Developing using 312 developer for about 45 s followed by soaking in DI water.
8. Oxygen plasma etching for 60 s.
9. Evaporating a thin layer of titanium and a thick layer of gold in-situ.
10. Applying lift-off procedure using NMP and acetone.

3.3 Aluminum resonators integrated with three-Junction SQUIDs

The fabrication process applied in order to implement Al resonators coupled to rf-SQUIDs is very much similar to the process applied in the fabrication of aluminum resonators coupled to dc-SQUIDs. The main difference lies in the layout and the existence of a coupling gap between the resonators and the SQUIDs.

3.4 Niobium resonators integrated with three-Junction SQUIDs

We describe herein in more detail the fabrication process applied in order to implement Nb resonator coupled to an rf-SQUID (i.e. Fig. 3.1).

1. **Cleaning:** The silicon wafers were cleaned thoroughly using solvents (acetone, methanol and isopropanol) in an ultra-sound bath. Afterwords the wafers were washed by DI water and dried.
2. **Sputtering:** this stage consisted of three sequential sputtering steps applied in-situ (inside the sputtering machine), (1) sputtering of AlN 50 Å (an optional protective layer), (2) sputtering of Nb 1300 Å, (3) sputtering of AlN 200 Å (mask layer).

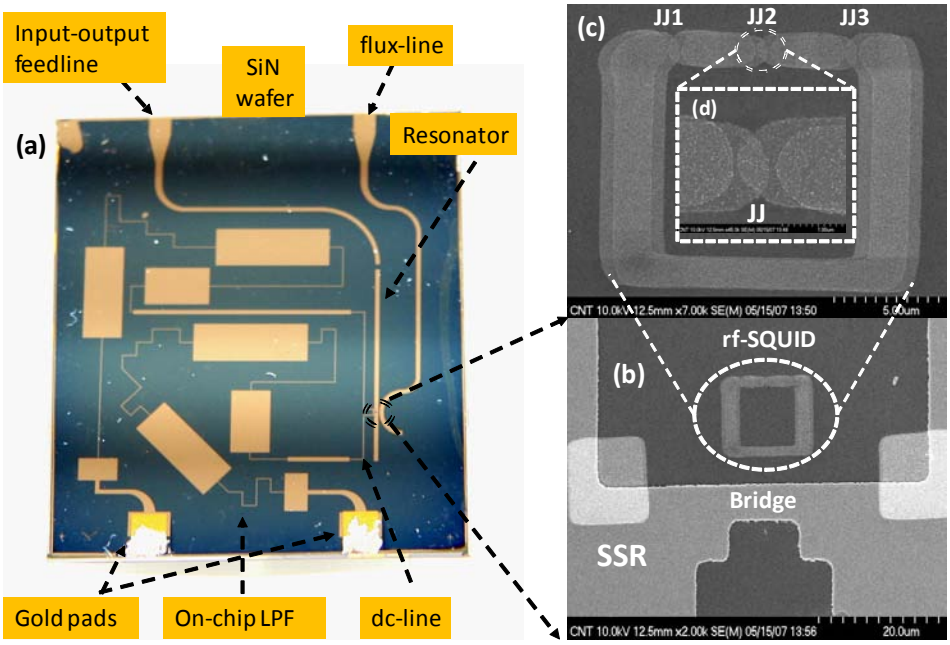

Figure 3.1: (a) An optical image showing one of the integrated systems (resonator-flux qubit) that have been fabricated. (b), (c) and (d) Zoom-in scanning electron micrographs (b) A flux qubit coupled to a superconducting stripline resonator (SSR) made of Nb via a narrow bridge positioned along the resonator at a predetermined location. (c) A zoom-in micrograph of the flux qubit containing three Josephson junctions. (d) A zoom-in micrograph of the Josephson junction at the middle.

3. **Gold pads:** after stripping the thin layer of AlN covering the bottom part of the wafer using photo-resist developer (wet-etching), and placing an appropriate mechanical mask on top of the wafer in order to form the pads, 100 Å of titanium was evaporated followed by evaporation of a thick layer of gold on the order of 3000 Å in-situ. The titanium was evaporated in order to enhance adhesion between niobium and gold.

4. **Electron-beam lithography 1 (bridge formation):**

   (a) PMMA spinning: two layers of PMMA 495 A6 were spined at 4000 rpm for 1 min each (the exact value of spinning rate was sometimes varied for different devices). One layer of PMMA 950 A2 was spined at 5000 rpm for 1 min (the exact value of spinning rate was sometimes varied for different devices). The wafer was baked at 180 °C on a hot plate for 5 minutes, prior to each spinning step and following the formation of the last layer. The spinning parameters yield a total PMMA thickness in the range 6500-8400 Å (The common/preferred value is about 7000 Å).

   (b) Bridge formation: a narrow section along the resonator is written using E-beam lithography.

   (c) Development: the sample is rinsed in MIBK (methylisobutylketone) for 1 min, followed by 20 s in iso-propanol.

5. **Etching 1 (bridge formation):**

   (a) Electron Cyclotron resonance (ECR) etching for 30 s in order to get rid of the top AlN mask defined by the e-beam lithography process.

   (b) PMMA stripping: the sample is immersed in NMP and heated on a hot plate at 140 °C for more than one hour.

   (c) Applying reactive ion etching (RIE) for 10 min, which eventually creates the bridge section along the resonator. In this step the AlN layer functions as a mask.

6. **UV lithography:** Resist deposition: following a baking stage on a hot plate at 110 °C for 5-10 min, a layer of 4533 photo-resist was spined at 4000 rpm for 1 min. Pre-baking in a 90 °C oven for 10 min. The

layout of the resonator was implemented using UV lithography. Prior to exposure, the resonator mask was carefully aligned with the bridge section formed earlier. Following an exposure time ranged between 11-18 s (depending on the photo-resist) the sample was developed using 312 or 326 developer for more than 1 min in order to ensure that the AlN layer beneath the dissolved photo-resist has been totally etched. Afterwards the photo-resist was stripped by immersing the sample in NMP solution heated on a hot plate at 140 °C for more than 1 h.

7. **Etching 2 (resonator and flux-line formation):** ECR etching of the redundant Nb for 100 s. Consequently the resonator layout defined by the UV lithography mask is realized. Following this stage the sample was rinsed in a developer in order to wet etch the AlN mask.

8. **Electron-beam lithography 2 (SQUID):**

   (a) PMMA deposition: three-layer PMMA deposition. The sample was dried on a hot plate for 5 min. Two bottom layers of PMMA 495 A6 were deposited at 3000 rpm for 1 min. One top layer of PMMA 950 A2 was deposited at 5000 rpm for 1 min (total PMMA thickness 650 nm-750 nm). The sample was baked on a hot plate at 180 °C for 5 min following the deposition of each PMMA layer.

   (b) The SQUID was written using e-beam lithography following an accurate alignment with the resonator bridge section formed earlier. The e-beam current was 200 p A, the dozes applied were in the range 180-250 $\mu\,\mathrm{C}/\,\mathrm{cm}^2$, whereas the magnification used was in the range 500-2000 (depending on the device).

   (c) Developing stage: the sample was developed in a MIBK solution for 1 min. Afterwards, it was rinsed in iso-propanol for 20 s.

9. **Aluminum shadow evaporation (formation of Al/AlO_x/Al junctions)**

   (a) Evaporation of 50 nm layer at 38 degrees relative to the perpendicular.

   (b) Oxidation stage: applying a gas mixture of argon (80%) and oxygen (20%) at pressure 0.15 torr for 12 minutes (the pressure tested, varied in the range $0.03 - 0.15$ torr).

(c) Evaporation of 30 nm layer at -38 degrees relative to the perpendicular.

10. **Lift-off:** the PMMA was stripped by immersing the sample in NMP solution at 140 °C for more than 1 h and then soaking the sample in acetone or applying "delicate" ultra-sonic vibrations.

Chapter 4

Measurements and Results

4.1 Observation of bifurcations and hysteresis in nonlinear NbN superconducting microwave resonators

Observation of Bifurcations and Hysteresis in Nonlinear NbN Superconducting Microwave Resonators

Baleegh Abdo, *Student Member, IEEE,* Eran Arbel-Segev, Oleg Shtempluck, and Eyal Buks

***Abstract*—In this paper, we report some extraordinary nonlinear dynamics measured in the resonance curve of NbN superconducting stripline microwave resonators. Among the nonlinearities observed: aburpt bifurcations in the resonance response at relatively low input powers, asymmetric resonances, multiple jumps within the resonance band, resonance frequency drift, frequency hysteresis, hysteresis loops changing direction and critical coupling phenomenon. Weak links in the NbN grain structure are hypothesized as the source of the nonlinearities.**

***Index Terms*—Bifurcations, hysteresis, jumps, microwave resonators, nonlinear effects, NbN.**

I. Introduction

NONLINEAR effects in superconductors in the microwave regime have been the subject of a large number of intensive studies in recent years. Most of the attention is focused on studying one or more of the following issues: investigating the origins of nonlinear effects in superconductors [1], [2], introducing theoretical models that explain nonlinear behavior [3], [4], identifying the dominant factors that manifest these effects [5], [6], find ways to control and minimize nonlinear effects [7], [8] such as, harmonic generation and intermodulation distortions, which degrade the performance of promising superconducting microwave applications mainly in the telecommunication area [9].

Among the nonlinear effects reported in the literature associated with resonance curves, one can find the commonly known Duffing oscillator nonlinearity which is characterized by skewed resonance curves above certain power level, appearance of infinite slope in the resonance lineshape, pronounced shift of the resonance frequency and hysteretic behavior [10]–[12]. To account for this effect, associated with the rise of kinetic inductance of superconductors, both thermal [13], and weak link [10] explanations have been successfully applied. Other nonlinear effects were reported by Portis *et al.* [14], where they observed notches that develop on both sides of the frequency response of their high-temperature superconducting (HTS) microstrip patch antenna, accompanied with hysteresis and frequency shift, in the nonlinear regime. Similar results were reported also by Hedges *et al.* [15], in their YBCO stripline resonator, and in [16] in YBCO thin film dielectric cavity. All three studies [14]–[16] attributed the observed nonlinear behavior to abrupt changes in the resistive loss of weak links, thermal quenching, and weak link switching to normal state.

In this study, being interested in the behavior of nonlinear resonances, we have fabricated different NbN superconducting microwave resonators exhibiting some unusual nonlinear effects, which to the best of our knowledge, have not been reported before in the literature. We study the dependence of these resonators on input power, and examine the resonance curve behavior under different scan directions. To account for our results, we consider some possible physical mechanisms which may be responsible for the observed effects.

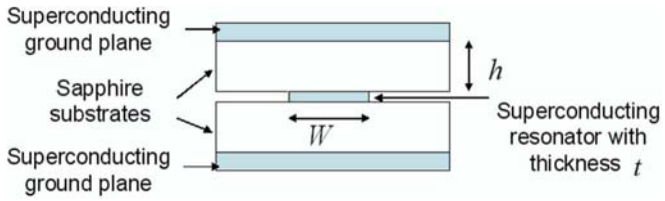

Fig. 1. Stripline geometry.

II. Resonators Design

The resonators were designed in the standard stripline geometry, which consists of five layers, as shown in the cross-section illustration, depicted in Fig. 1.

The superconducting resonator was dc-magnetron sputtered on one of the sapphire substrates, whereas the superconducting ground planes were sputtered on the inner covers of a gold plated Faraday package made of oxygen free high conductivity (OFHC) copper employed to house the resonators. The dimensions of the sapphire substrates were $34 \times 30 \times 1$ mm. The resonator geometries implemented, which we will refer to them, for simplicity, by the names B1, B2, and B3, are presented in the insets of Figs. 3–5 respectively. The width of the feedlines and the thin part of the resonators was set to 0.4 mm to obtain characteristic impedance of 50 Ω. The gap between the feedline and the resonators was set to 0.4 mm in B1, B3 cases, and to 0.5 mm in B2 case. The frequency modes of B1, B2, B3 resonators were theoretically calculated using a simple transmission line model, presented in Appendix A, and were also experimentally

Manuscript received January 9, 2005; revised June 28, 2005. This paper was recommended by Associate Editor J. Mazierska. This work was supported by the German Israel Foundation under Grant 1-2038.1114.07, by the Israel Science Foundation under Grant 1380021, and by the Deborah Foundation and Poznanski Foundation.

The authors are with the Department of Electrical Engineering and Microelectronics Research Center, Technion, Haifa 32000, Israel (e-mail: baleegh@tx.technion.ac.il).

Color versions of Figs. 1–5, Figs. 7–10 and Figs. 13–15 are available online at http://ieeexplore.ieee.org.

Digital Object Identifier 10.1109/TASC.2006.881823

TABLE I
SPUTTERING PARAMETERS

Process parameter	B1	B2	B3
Partial flow ratios (Ar,N2)	(87.5%,12.5%)	(75%,25%)	(70%,30%)
Base temperature	11 °C	11 °C	13 °C
Total pressure	$6.9 \cdot 10^{-3}$ torr	$8.1 \cdot 10^{-3}$ torr	$5.7 \cdot 10^{-3}$ torr
Discharge current	0.36A	0.55A	0.36A
Discharge voltage	351V	348V	348V
Discharge power	121W	185W	133W
Deposition rate	$6\frac{\text{Å}}{sec}$	$7.8\frac{\text{Å}}{sec}$	$3.8\frac{\text{Å}}{sec}$
Thickness (t)	2200 Å	3000 Å	2000 Å
Base pressure	$3.1 \cdot 10^{-8}$ torr	$7.3 \cdot 10^{-8}$ torr	$8 \cdot 10^{-8}$ torr
Target-substrate distance	80mm	90mm	90mm

measured using vector network analyzer (NA). The theoretical calculation was found generally to be in good agreement with the measurement results, as discussed in Appendix A.

III. FABRICATION PROCESS

The sputtering of the NbN films was done using a dc-magnetron sputtering system. All of the resonators reported here were deposited near room temperature [17]–[19], where no external heating was applied.

The system was usually pumped down prior to sputtering to $3\text{–}8 \cdot 10^{-8}$ torr base pressure (achieved overnight). The sputtering was done in Ar/N_2 atmosphere under current stabilization condition [20]. The relative flow ratio of the two gases into the chamber and the total pressure of the mixture were controlled by mass flow meters. The sputtering usually started with a -min presputtering in the selected ambient before removal of the shutter and deposition on the substrate. The sputtering parameters of the three resonators are summarized in Table I. Following the NbN deposition, the resonator features were patterned using standard photolithography process, whereas the NbN etching was done using Ar ion-milling.

To obtain resonators with reproducible physical properties we have used the sputtering method discussed in [20] and [21], where it was claimed that reproducible parameters of films are assured, by keeping the difference between the discharge voltage in a gas mixture and in pure argon, constant, for the same discharge current. In Fig. 2, we show one of the characterization measurements applied to our dc-magnetron sputtering system, exhibiting a knee-shape graph of discharge current as a function of discharge voltage. The knee-shape graph was obtained for different Ar/N_2 mixtures at room temperature. The discharge voltage difference measured in the presence of N_2 gas relative to the value measured in pure argon at the same discharge current, is also pointed out in the figure, corresponding to different currents and N_2 percentages.

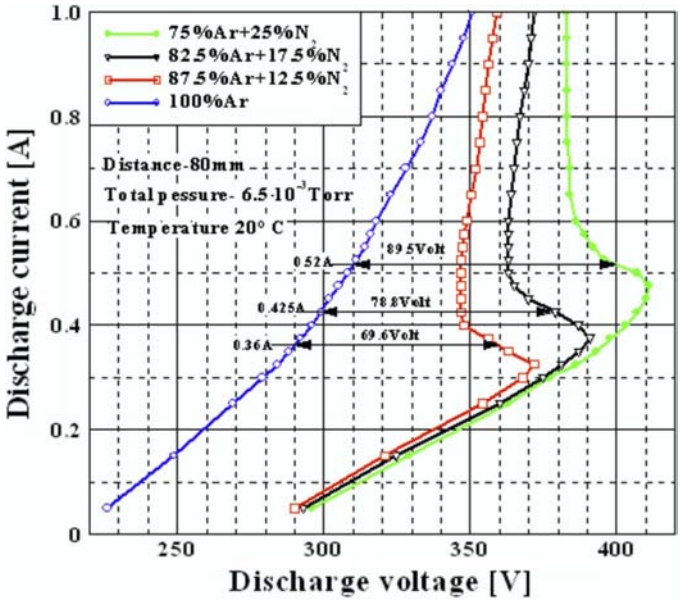

Fig. 2. Discharge current versus discharge voltage of the sputtering system displaying current-voltage knee for different percentages of Argon and Nitrogen, at ambient temperature of 20°C.

IV. PHYSICAL PROPERTIES

The fabricated resonators were characterized by relatively low T_c for NbN and relatively intermediate resistivity ρ. Resistance measurements were performed using standard four probe technique. T_c measured for B1, B2 and B3 was 10.7, 6.8, 8.9 [K] respectively, whereas ρ measured was 348 and 500 $[\mu\Omega]$ cm for B2 and B3, respectively. Critical temperature width ΔT_c measured for B3 resonator yielded 0.5 K (where ΔT_c is defined by the 5% and 95% points of the resistive transition), which may indicate that the intergrain Josephson coupling in this film is still dominant compared to granular behavior [22]. Residual resistance ratio (RRR) defined as $\rho(300)/\rho(15)$, where $\rho(300)$ refers to resistance value at room temperature and $\rho(15)$ refers to resistance before superconducting transition, was also measured for B3 resonator and yielded RRR of 0.5. This less than unity low RRR ratio, indicating a granular or columnar (island) structure [17] and nonmetallic conduction [18], [23], is in good correlation with the relatively low T_c (8.9 K) and high resistivity ρ (500 $\mu\Omega$ cm), measured for this film [18]. In addition, RRR ratios less than unity, implying a negative temperature coefficient of resistivity (TCR) [24] (the resistance increases with decreasing temperature), generally characterizes NbN films having a columnar (island) structure [24]. Moreover, these measured parameters $T_c, \Delta T_c, \rho$ and RRR ratio are in good agreement with the results of [22] and [18], where it was shown that increasing the partial pressure of N_2 in Ar/N_2 mixture at a given total pressure tends to decrease RRR ratio and T_c, and increase ρ and ΔT_c. The relatively low T_c measured, can be attributed also to bulk degradation and vacancies [22], or more likely to columnar grain boundaries [25]. Furthermore, from scanning electron microscopy micrographs taken to a NbN film sample sputtered with similar sputtering conditions as B2 resonator, and showing a clear columnar structure of the kind discussed in [24]–[26],

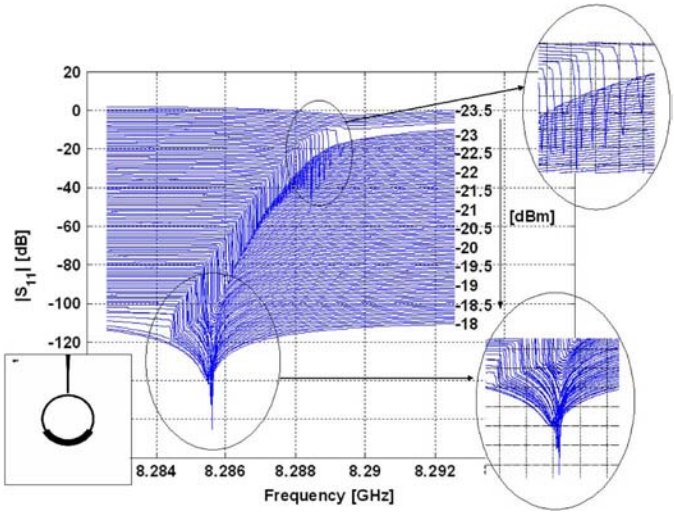

Fig. 3. S_{11} measurement of B1 resonance at ~ 8.288 GHz with 10-MHz span, exhibiting extraordinary nonlinear effects at low input powers. Resonance curves corresponding to different input powers were shifted by a constant offset for clarity.

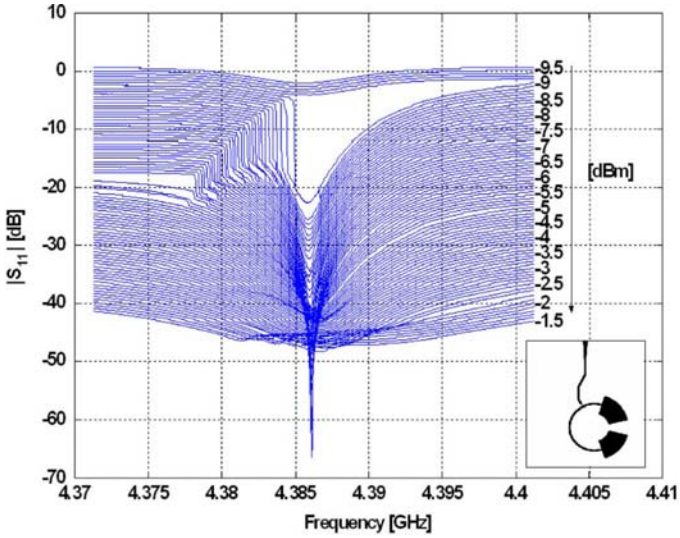

Fig. 4. S_{11} measurement of B2 resonance at ~ 4.385 GHz with 30-MHz span, exhibiting strong nonlinear effects at low input powers. Resonance curves corresponding to different input powers were shifted by a constant offset for clarity.

one can estimate the diameter of the columnar structure to be of the order of 20 nm.

V. Measurement Results

All measurements presented in this paper have been conducted at liquid helium temperature 4.2 K, and were verified using two cryogenic configurations. One was by immersing the resonator package in liquid helium, two by housing the resonator package in vacuum inside a temperature controlled cryostat. No significant differences were detected in the experimental data measured using these two cryogenic techniques.

A. S_{11} Measurements

The resonance response of the resonators was measured using the reflection parameter S_{11} of a NA. The resonance response obtained for the third mode of B1 resonator ~ 8.288 GHz at low input powers, between -23 dBm and -18 dBm in steps of 0.05 dBm, is shown in Fig. 3. A small vertical offset was applied for clarity between the sequential graphs corresponding to different input powers and to show the nonlinear evolution of the resonance response as the input power is increased. The interesting characteristics of this nonlinear evolution can be summarized as follows.

1) In the power range between -23.5 dBm and -23.25 dBm, the resonance is symmetrical and broad.
2) At input power level of -23.25 dBm, a sudden jump of about -15 dB occurs in the resonance curve at the minima where the slope of the resonance response is small.
3) As the input power is increased in steps of 0.05 dBm the resonance becomes asymmetrical, and the left jump shifts towards lower frequencies gradually.
4) As we continue to increase the input power, the jumps decrease their height but the resonance curve following the jumps becomes more symmetrical and deeper, and at a certain input power level we even witness a critical coupling phenomenon where $S_{11}(\omega)$ at resonance is almost zero, that is no power reflection is present.
5) The resonance becomes symmetrical again and broader and the jumps disappear.
6) All previously listed effects occur within a frequency span of 10 MHz, power range of about 5 dBm, and power step of 0.05 dBm.

Similar behavior to that exhibited by the nonlinear third mode of resonator B1 can be clearly seen in Figs. 4 and 5, which show the nonlinear dynamic evolution of the second mode of resonator B2 and the first mode of B3 respectively. The main differences between the figures are:

1) The power levels at which these nonlinear effects appear. Whereas in B1 case they happen between -23 dBm and -18 dBm, in B2 case they happen between -9.5 dBm and -1.5 dBm and in B3 case they happen around 1 dBm.
2) In Fig. 5 corresponding to B3 resonator we witness three apparent jumps within the resonance band as indicated by circles shown on the figure, a feature that we did not encounter in Figs. 3 and 4.

In order to evaluate approximately the peak RF magnetic field H_{RF} at the surface of the stripline, associated with the onset of nonlinearity of the resonances shown in Figs. 3 and 4, we apply the calculation method described in [27], [28] for a uniform resonator, with the necessary changes to account for the one port configuration and the nonuniform current density at the edges. The maximum RF current of the standing waves at resonance in a uniform resonator is given by $I_{\max} = \sqrt{(1-r_v^2)8QP_W/n\pi Z_0}$, where r_v is related to the return loss R measured in [dB] given by $R = -20\log_{10} r_v$, where Q is the unloaded quality factor of the stripline (to obtain an order of magnitude of H_{RF} we assume $Q_L \sim Q$), P_W is the incident power, n is the mode number of the resonance measured, and Z_0 is the characteristic impedance of the transmission line $\sim 50\ \Omega$. Thus, the peak of the RF magnetic field H_{RF} at the edges of the strip associated with $I_{\max}$, can be evaluated by accounting for the nonuniform current density along the cross section of the strip and by applying Ampere's

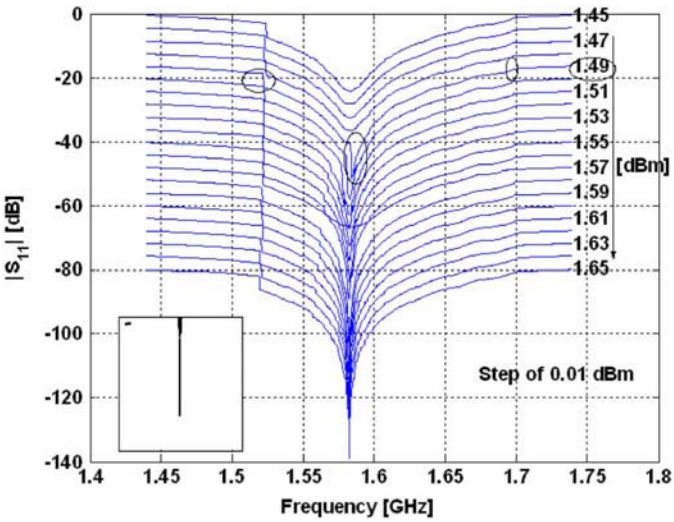

Fig. 5. Nonlinear response of B3 resonance at ~ 1.6 GHz, corresponding to input power levels increasing by a 0.01 dBm step. At input power of 1.49 dBm, we observe two obvious jumps in the resonance band, and another small one at the right side, marked with circles. The different resonance curves were shifted by a constant offset for clarity.

law at the edges. A relatively good approximation for the nonuniform current density of a thin isolated strip of width W and thickness t is given by [29]

$$J(x) = \begin{cases} \frac{J(0)}{\sqrt{1-\left(\frac{2x}{W}\right)^2}}, & |x| \le \frac{W}{2} - \frac{\lambda^2}{2t} \\ J\left(\frac{W}{2}\right)\exp\left\{-\frac{t}{\lambda^2}\left(\frac{W}{2}-x\right)\right\}, & \frac{W}{2} - \frac{\lambda^2}{2t} < |x| \le \frac{W}{2} \end{cases} \quad (1)$$

where $J(W/2) = \exp(1/2)\sqrt{Wt}J(0)/\sqrt{2}\lambda$, λ is the London penetration depth, $J(0)$ is the current density at the middle of the strip.

In the following calculations, λ is assumed to be comparable to the thickness of the strip $t(t \simeq \lambda)$ (since λ of NbN is typically in the range of 2000–4000 unit Å [30]), whereas W the width of the strip is assumed to be the width of the narrowest part of the film 0.4 mm. Substituting the following values for B1 resonator at the onset of nonlinearity shown in Fig. 3, $P_{\rm dBm} = -23$ dBm, $R = 30$ dB, $Q \sim 7000, n = 3$, yields the following approximate peak RF magnetic field at the narrowest part $H_{\rm RF}\sim 6$ Oe. Whereas for B2 second resonance shown in Fig. 4, one gets $H_{\rm RF}\sim 9$ Oe, which corresponds to the following parameters, $P_{\rm dBm} = -9$ dBm, $R = 20$ dB, $Q\sim 462, n = 2$.

Moreover, by comparing the onsets of nonlinearity corresponding to the different resonance frequencies one finds different values even for the same resonator. Whereas, in B1 resonator, the onset of nonlinearity for the third resonance (~ 8.288 GHz) is about $I_{\rm max}\sim 24$ mA (~ 6 Oe), the onset of nonlinearity for the first resonance (~ 2.59 GHz) is much lower, $I_{\rm max}\sim 9$ mA (~ 2 Oe). In B2 resonator, whereas the second resonance frequency (~ 4.385 GHz) exhibited strong nonlinear behavior at about $I_{\rm max}\sim 40$ mA (~ 9 Oe) of the kind shown in Fig. 4, the first resonance frequency (~ 2.52 GHz) exhibited similar but smaller jumps at about $I_{\rm max}\sim 104$ mA (~ 23 Oe). In B3 resonator, the onset of nonlinearity for the first resonance is about $I_{\rm max}\sim 61$ mA (~ 17 Oe) (not shown in Fig. 5), whereas other resonances of this resonator exhibited nonlinearities at much lower currents about $I_{\rm max}\sim 4$ mA (~ 1 Oe).

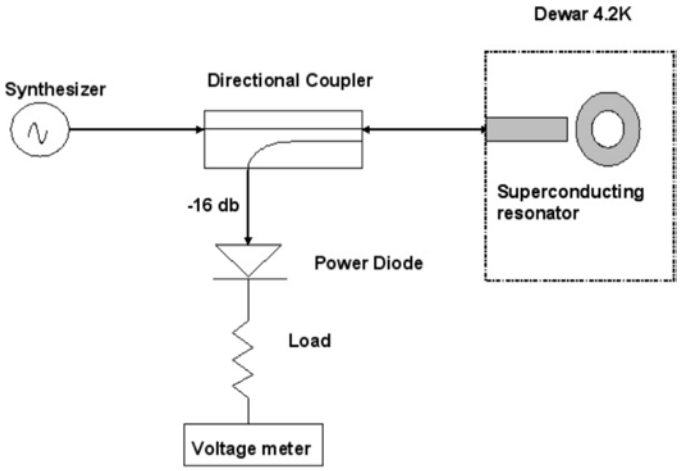

Fig. 6. Setup used to verify the occurrence of the bifuractions at the nonlinear resonance (B1 third mode) previously measured by NA.

These relatively low RF currents and magnetic fields, at which the nonlinear effects appear in the NbN films, are orders of magnitude lower than the magnetic fields generally reported in the literature, see for example [28], [31]–[33] , but they are, on the other hand, on the order of RF magnetic fields associated with Josephson vortices in YBCO grain boundaries reported for example in [34] and [35].

B. Verifications

In order to verify that the jump feature, previously measured using NA S_{11} parameter, is not a measurement artifact, we have applied a different measurement configuration, shown in Fig. 6, where we swept the frequency of a synthesizer and measured the reflected power from the resonator using a power diode and a voltage meter. The load that appears in Fig. 6 following the diode is used in order to extend the linear regime of the power diode. The results of this measurement configuration are shown in Fig. 7. The frequency scan around the resonance was done using 201 points in each direction (forward and backward). A small hysteresis loop is visible in the vicinity of the two jumps.

C. Abrupt Jumps

In attempt to find out whether the resonance curve of these nonlinear resonances changes its lineshape along two or more frequency points, further measurements where carried out using NA, where we scanned the frequency axis in the vicinity of the jump with high frequency resolution. The measurement results corresponding to frequency step of ~ 600 Hz and ~ 2.5 kHz are presented in Fig. 8(a) and (b), respectively, indicating abrupt transition between two bistable states.

D. Frequency Hysteresis

Bifurcations in the resonance response of the device usually occur when the resonance curve becomes multiple valued as a function of the drive frequency. Such multiple valued resonance

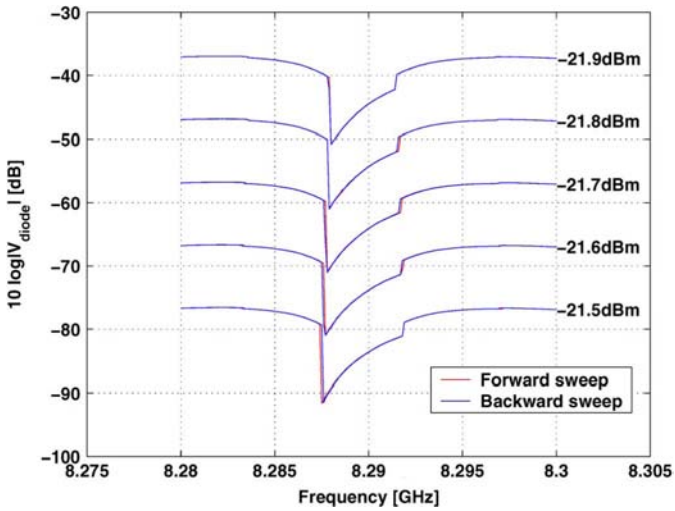

Fig. 7. Nonlinear response of B1 third mode measured using the configuration shown in Fig. 6. Red line represents a forward scan whereas the blue line represents a backward scan. Two abrupt jumps appear at both sides of the resonance curve and small hysteresis loops are present at the vicinity of the jumps. Resonance curves corresponding to different input powers were shifted by a constant offset for clarity.

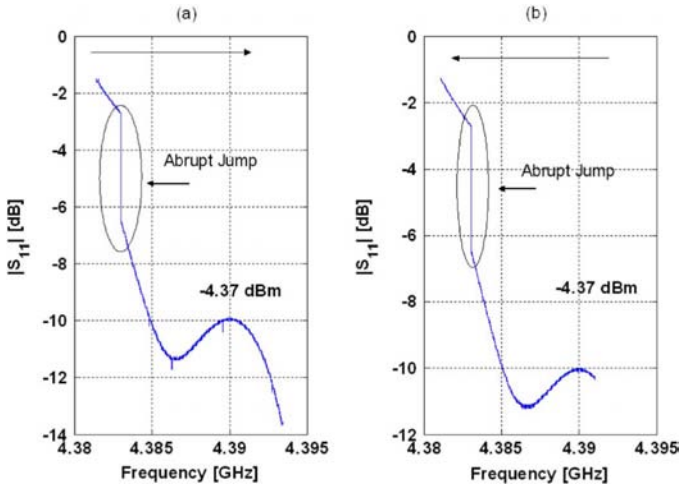

Fig. 8. (a) Forward continuous wave (CW) mode scan using NA, in a 12-MHz span around the left jump of the nonlinear resonance of B2. The scan includes 20 000 frequencies, which is equivalent to a frequency step of ~ 600 Hz between the data points. In spite of this small frequency step, the jump occurs between just two sequential frequencies. (b) A backward CW mode scan using NA, within a 10 MHz span around the left jump of the nonlinear resonance of B2. The scan includes 4000 frequencies, which is equivalent to a frequency step of ~ 2.5 kHz between the data points. Also for this case the jump occurs between just two sequential frequencies.

response generally lead to a hysteretic behavior at the vicinity of the bifurcations. In order to examine the resonance response dependence of these resonators on frequency, we have applied forward and backward frequency sweeps.

In Fig. 9, we show a representative frequency scan of B2 second mode, applied in both directions, featuring some interesting hysteretic behavior:

1) At low input powers -8.05 dBm and -8.04 dBm, the resonance is symmetrical and there is no hysteresis.

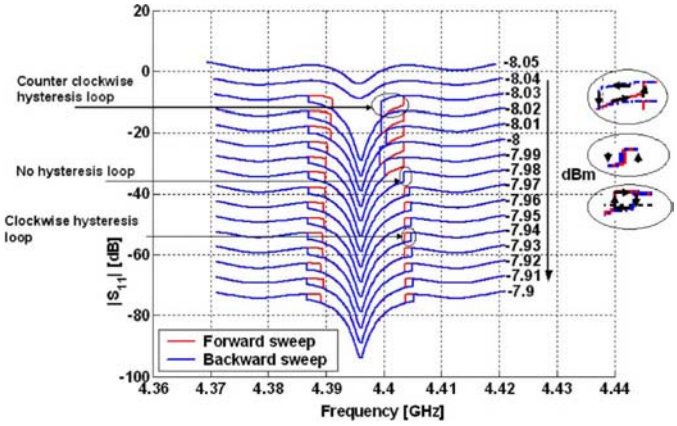

Fig. 9. Forward and backward scan measurement, performed using NA, measuring B2 second mode nonlinear resonance. Red line represents a forward scan whereas the blue line represents a backward scan. The graphs exhibit clear hysteresis loops forming at the vicinity of the jumps, and hysteresis loop changing direction as the input power is increased. Resonance curves corresponding to different input powers were shifted by a constant offset for clarity.

2) As the power is increased by 0.01 dBm to -8.03 dBm, two jumps occur at both sides of the resonance response and hysteresis loops form at the metastable regions.
3) As we continue to increase the input power gradually, the hysteresis loop associated with the right jump changes direction. At first it circulates counterclockwise between -8.03 dBm and -7.99 dBm, at -7.98 dBm the two opposed jumps at the right side meet and no hysteresis is detected. As we further increase the power, the right hysteresis loop appears again, circulating, this time, in the opposite direction, clockwise.

It is worth mentioning that the hysteresis loops changing direction are not unique to this resonator, or to the jump on the right side of the resonance. It appears also in the modes of B1, and it occurs at the left side jump of this resonance as well, though at different power level.

E. Multiple Jumps

Frequency sweep applied to B3 first resonance in both directions, exhibits yet another feature, in addition to the two jumps at the sides of the resonance curve, which we have seen earlier, there are another smaller jumps accompanied with hysteresis within the resonance lineshape, adding up to 3 jumps in each scan direction, and four hysteresis loops, as exhibited in Fig. 10.

F. Surface Impedance

Following surface impedance analysis carried in [2], [31], [34] which is generally used as an effective tool for investigating nonlinearity [10], [32], we try to quantify reactance and resistive changes, ΔX and ΔR, respectively, in the resonators, as a function of RF input power P_{RF}, using the following relations, $\Delta X(P_{\mathrm{RF}}) \propto 2\Delta f_0/f_0 = 2[f_0(P_{\min}) - f_0(P_{\mathrm{RF}})]/f_0(P_{\min})$ and $\Delta R(P_{\mathrm{RF}}) \propto \Delta(1/Q) = 1/Q(P_{\mathrm{RF}}) - 1/Q(P_{\min})$ [2], where f_0 is the resonance frequency determined from the minimum of the resonance curve, Q is the quality factor of the resonator, and $P_{\min}$ is the onset of nonlinearity input power. Whereas the first expression defines the relative frequency shift

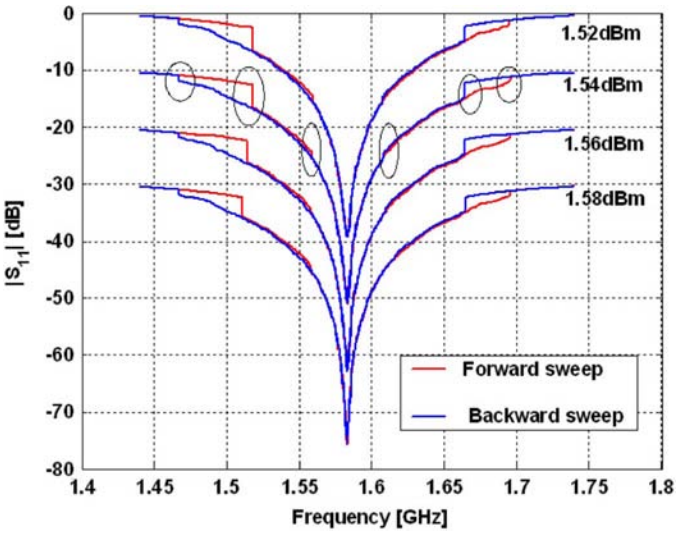

Fig. 10. S_{11} parameter measurement of the first resonance of B3 at input powers 1.52 dBm through 1.58 dBm in steps of 0.02 dBm using forward and backward CW mode scan of NA employing 2000 measurement points in each direction. Graph shows clearly three jumps within the band of the resonance in each direction. Resonance curves corresponding to different input powers were shifted by a constant offset for clarity.

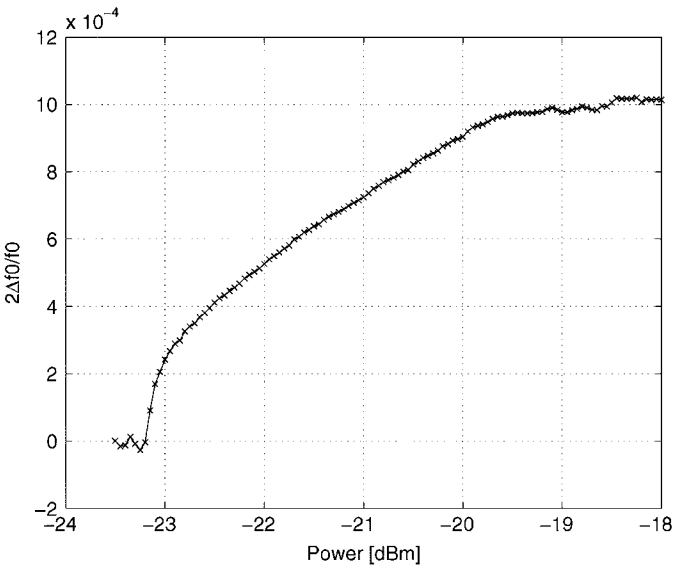

Fig. 11. Relative frequency shift $2\Delta f_0/f_0$ as a function of RF input power, corresponding to B1 third resonance frequency.

of the resonance, the second expression defines the difference in the microwave losses of the resonator. The quality factor Q of the resonators in the nonlinear regime was calculated using a Lorentzian fit applied to the $|S_{11}|^2$ data (the square amplitude of the reflection parameter) in the vicinity of the resonance [36]. Nevertheless, this approach does not enable us to calculate unambiguously the Q factor of the resonance curves which are extremely asymmetrical and do not resemble Lorentzians in the vicinity of the resonance [2], [28], such as those shown in Fig. 3. Therefore, the graph exhibiting $\Delta(1/Q)$ for B1 resonance is not plotted here. In Figs. 11 and 12(a), we show the

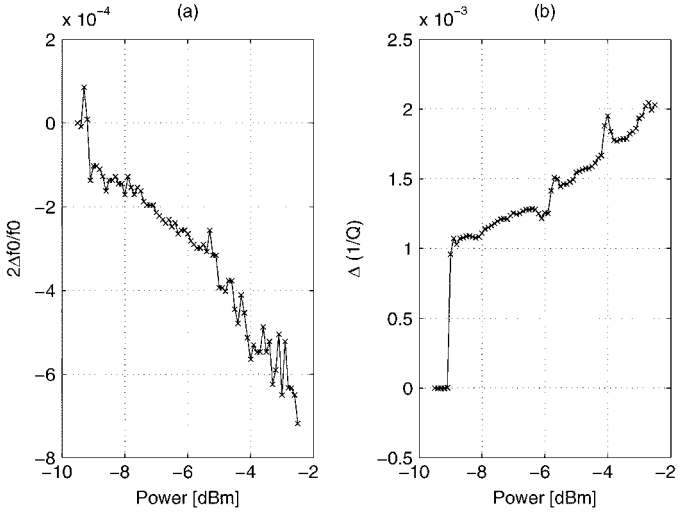

Fig. 12. (a) Relative frequency shift $2\Delta f_0/f_0$. (b) Relative microwave losses $\Delta(1/Q)$. Both graphs correspond to B2 second resonance frequency and are given as a function of RF input power.

$2\Delta f_0/f_0$ ratio calculated for B1 and B2 resonators respectively, whereas in Fig. 12(b), we show the difference ratio $\Delta(1/Q)$ for B2 resonator.

In Fig. 11, we observe a steep decrease in the resonance frequency at about -23 dBm, followed by a gradual shift of the resonance towards the lower frequencies up till -19.5 dBm, above which a plateau in the resonance frequency is observed. Whereas in Fig. 12(a) we measure a step in the resonance frequency at about -9 dBm, followed by a gradual increase untill -2 dBm. As to the relative losses $\Delta(1/Q)$, in Fig. 12(b), representing the second resonance of B2, the relative losses jumps at the onset of nonlinearity ~ -9 dBm and afterwords changes gradually as the input power increases.

Although Figs. 11 and 12 do not provide a clear coherent picture as to the physical origin of the observed nonlinearities, one can verify easily that these results differ from the resonance nonlinearities presented, for example, in [2], [10], [28], [31] exhibiting nonlinear effects which can be explained in terms of one dimensional Duffing oscillator equation [7], [37].

VI. Comparison with Duffing Oscillator Nonlinearity

In general hysteretic behavior in superconducting films is caused by one of the following physical nonlinear mechanisms: pair breaking, intrinsic nonlinearity [7], heating effects [13], vortex dynamics [34], and Josephson junctions [38]–[40]. *Oates et al.* in [37], showed that inductance change ΔL can lead to hysteretic behavior in the resonance response, whereas resistance change ΔR tends to suppress it (where ΔL and ΔR are given by the following relations $L = L_0 + \Delta L(I/I_c)^2, R = R_0 + \Delta R(I/I_c)^2$ [7], where I is the total current, $I_c$is the critical current, L_0, R_0 are the zero order inductance and resistance per unit length respectively). However, substituting L (inductance per unit length) and R (resistance per unit length) of the form $L = L_0 + \Delta L(I/I_c)^2, R = R_0 + \Delta R(I/I_c)^2$ into the transmission line equations given by $\partial I/\partial z = -C\partial V/\partial t, \partial V/\partial z =$

$-L\partial I/\partial t - RI$ [7], where V is the voltage along the transmission line and C is the capacitance per unit length, leads eventually to Duffing oscillator nonlinearity, which qualitatively differ from our results.

The main differences can be summarized as follows.

1) Whereas Duffing oscillator nonlinearity is gradual and builds up as the input power is increased, these presented effects are sudden and demonstrate high sensitivity to input power on the order of 0.01 dBm. (Figs. 3, 4, 9).
2) In Duffing oscillator nonlinearity, we observe (with Nb resonators) one jump and one or no hysteresis loop in the resonance lineshape, whereas in these resonators we observe two and sometimes more jumps and hysteresis loops. (Figs. 9 and 10).
3) In Duffing oscillator nonlinearity the hysteresis loop keeps its circulation direction, whereas in the presented results, the hysteresis loops may change direction. (Fig. 9).
4) These nonlinear effects may lead to critical coupling condition in some resonances. (Figs. 3 and 4).
5) Above some input power level the resonance becomes symmetrical again unlike Duffing oscillator nonlinearity. (Figs. 3 and 4).

VII. Nonlinear Mechanism Modeling

In attempt to account for some of the unusual nonlinear effects presented earlier, we consider herein a hypothesis according to which weak links (WL) forming at the boundaries of the granular NbN columnar structure [24]–[26] are the main source of the nonlinearities. WL, as it is well known, is a general term which represents a wide variety of "material defects," such as impurities, edge defects, built in Josephson junctions, insulating layers, grain boundaries, voids, and weak superconducting points [1]. Under certain conditions and circulating RF currents these WL can interrupt the shielding supercurrents and as a result affect the conductivity [41], the resonance mode and the losses inside the resonator. Thus, in this section we will consider a simple model where local heating mechanism acts on WL in the NbN films and switch them between normal and superconducting states [42]. This switching hypothesis is partly supported by Fig. 13, where the same experimental data of Fig. 9, have been redrawn while canceling the vertical offset between the different resonance curves. The resulting plot in Fig. 13, exhibits clearly abrupt transitions between two resonance curves.

For the purpose of modeling, consider a resonator driven by a weakly coupled feedline carrying an incident coherent tone $b^{\rm in}e^{-i\omega_p t}$, where $b^{\rm in}$ is a constant complex amplitude and ω_p is the drive angular frequency. The mode amplitude inside the resonator A can be written as $A = Be^{-i\omega_p t}$, where $B(t)$ is a complex amplitude, which is assumed to vary slowly on the time scale of $1/\omega_p$. In this approximation and while disregarding noise, the equation of motion of B reads [36]

$$\frac{dB}{dt} = \left[i(\omega_p - \omega_0) - \gamma\right] B - i\sqrt{2\gamma_1 1} b^{\rm in} \tag{2}$$

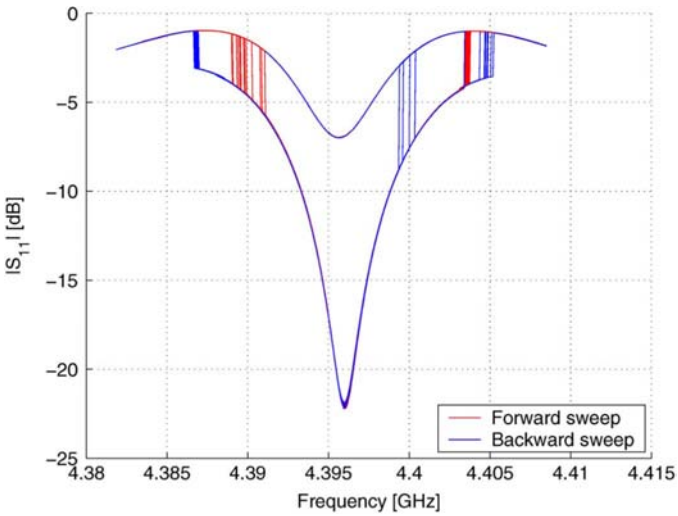

Fig. 13. Redrawing the experimental data of Fig. 9, while canceling the vertical offset between the graphs. The plot shows clear transitions between two resonance curves.

where ω_0 is the angular resonance frequency, $\gamma = \gamma_1 + \gamma_2$, where γ_1 is the coupling constant between the resonator and the feedline, and γ_2 is the damping rate of the mode.

In terms of the dimensionless time $\tau = \omega_0 t$, (2) reads

$$\frac{dB}{d\tau} = \frac{i(\omega_p - \omega_0) - \gamma}{\omega_0}(B - B_\infty) \tag{3}$$

where

$$B_\infty = \frac{i\sqrt{2\gamma_1} b^{\rm in}}{i(\omega_p - \omega_0) - \gamma}. \tag{4}$$

The output signal $a^{\rm out}$ reflected off the resonator can be written as $a^{\rm out} = b^{\rm out}e^{-i\omega_p t}$. The input–output relation relating the output signal to the input signal is given by [43]

$$\frac{b^{\rm out}}{\sqrt{\omega_0}} = \frac{b^{\rm in}}{\sqrt{\omega_0}} - i\sqrt{\frac{2\gamma_1}{\omega_0}} B. \tag{5}$$

Whereas the total power dissipated in the resonator Q_t can be expressed as [36]

$$Q_t = h\omega_0 2\gamma_2 E \tag{6}$$

where $E = |B|^2$.

Furthermore, consider the case where the nonlinearity is originated by a local hot spot in the stripline resonator. If the hot spot is assumed to be sufficiently small, its temperature T can be considered homogeneous. The temperature of other parts of the resonator is assumed be equal to that of the coolant T_0. The power Q heating up the hot spot is given by $Q = \alpha Q_t$ where $0 \leqslant \alpha \leqslant 1$.

The heat balance equation reads

$$C\frac{dT}{dt} = Q - W \tag{7}$$

where C is the thermal heat capacity, $W = H(T - T_0)$ is the power of heat transfer to the coolant, and H is the heat transfer coefficient. Defining the dimensionless temperature

$$\Theta = \frac{T - T_0}{T_c - T_0} \tag{8}$$

where T_c is the critical temperature, one has

$$\frac{d\Theta}{d\tau} = -g(\Theta - \Theta_\infty) \tag{9}$$

where

$$\Theta_\infty = \frac{2\alpha\gamma_2\rho E}{\omega_0 g} \tag{10}$$

$$\rho = h\omega_0 C(T_c - T_0) \tag{11}$$

$$g = \frac{H}{C\omega_0}. \tag{12}$$

The resonance frequency ω_0, the damping rates γ_1, γ_2, and α are assumed to have a step function dependence on the temperature

$$\omega_0 = \begin{cases} \omega_{0s}, & \Theta < 1 \\ \omega_{0n}, & \Theta > 1 \end{cases} \tag{13}$$

$$\gamma_1 = \begin{cases} \gamma_{1s}, & \Theta < 1 \\ \gamma_{1n}, & \Theta > 1 \end{cases} \tag{14}$$

$$\gamma_2 = \begin{cases} \gamma_{2s}, & \Theta < 1 \\ \gamma_{2n}, & \Theta > 1 \end{cases} \tag{15}$$

$$\alpha = \begin{cases} \alpha_s, & \Theta < 1 \\ \alpha_n, & \Theta > 1. \end{cases} \tag{16}$$

.

While disregarding noise, the coupled (3) and (9) may have, in general, up to two different steady state solutions. A superconducting steady state of the WL exists when $\Theta_\infty < 1$, or alternatively when $E < E_s$, where $E_s = gC(T_c - T_0)/2\alpha_s\gamma_{2s}h$. Similarly, a normal steady state of the WL exists when $\Theta_\infty < 1$, or alternatively when $E > E_n$, where $E_n = gC(T_c - T_0)/2\alpha_n\gamma_{2n}h$.

Moreover, the reflection coefficient S_{11} of the resonant in steady state is given by [36]

$$S_{11}(\omega) = \frac{b^{\text{out}}}{b^{\text{in}}} = \frac{\gamma_2 - \gamma_1 - i(\omega_p - \omega_0)}{\gamma_2 + \gamma_1 - i(\omega_p - \omega_0)}. \tag{17}$$

Thus, WL switching between the superconducting and the normal states cause simultaneous switching of $\omega_0, \gamma_1, \gamma_2, \alpha$ parameters which in turn change the resonance lineshape abruptly and result in hysteretic behavior in the bistable region.

In general, the heat capacity C can be expressed as $C = C_v t A_{\text{eff}}$, where C_v is the specific heat of NbN ($2.7\cdot10^{-3}$ J cm^{-3} K^{-1} [44]), t is the thickness of the film, and A_{eff} is the effective area of the hot spot. By further assuming that the generated heat is cooled mainly down the substrate rather than along the film [45], [46], the heat transfer coefficient H reads $H = \sigma A_{\text{eff}}$, where α is the thermal surface conductance between the superconducting film and the substrate. To obtain an estimate for A_{eff}, we evaluate the total dissipated power Q_t in the resonator [given by (6)] at the WL superconducting state threshold E_s : $Q_t = gC(T_c - T_0)\omega_0/\alpha_s$. Using (12) and $H = \sigma A_{\text{eff}}$ relation yield

$$A_{\text{eff}} \simeq \frac{Q_t}{\sigma(T_c - T_0)} \tag{18}$$

where α_s is assumed to be of order unity. To evaluate A_{eff} for the second mode of B2 at the onset power of nonlinearity $P_W \sim 1.6\cdot10^{-4}$ W (corresponding to ~ -8.03 dBm of Fig. 9), we relate Q_t to P_W at the jump frequency, using $Q_t = (1-r_v^2)P_W \simeq 8\cdot10^{-5}$ W. Substituting Q_t and the following resonator parameters: $T_c = 6.8$ K, $T_0 = 4.2$ K, $\sigma = 2$ W cm^{-2} K^{-1} at 4.2 K [46], [47], in (18) yield $A_{\text{eff}} \simeq 1.5\cdot 10^{-5}$ cm^2. Substituting this result in C and H expressions gives $C \simeq 1.2\cdot 10^{-12}$ J/K, $H \simeq 3\cdot10^{-5}$ W/K. Whereas direct substitution in (11) and (12) yield the dimensionless parameters $\rho \simeq 9\cdot10^{-13}, g \simeq 9\cdot10^{-4}$ respectively.

Next, we numerically simulate the unusual hysteretic behavior of B2 second mode ($\omega_{0n} = 2\cdot\pi\cdot 4.395$ GHz) shown in Fig. 9 using this model and the parameters derived above. In Fig. 14, we show one of the simulation results corresponding

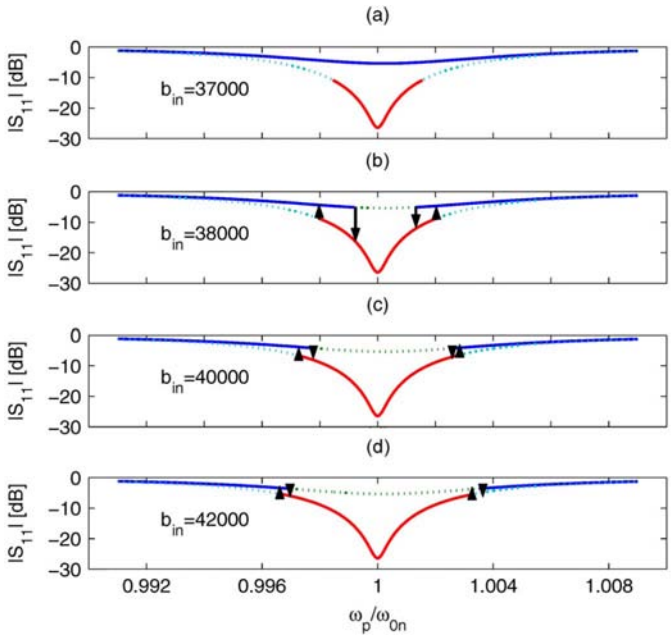

Fig. 14. Simulated resonance response. Plots (a)–(d) correspond to an increasing drive amplitude b^{in}. Solid lines represent valid steady state solutions whereas the dotted lines represent invalid solutions. Red/cyan lines represent the normal WL solutions, whereas the blue/green lines represent the superconducting WL solutions. Black arrows show the direction of the hysteresis loops in the different cases. Parameters that were used in the simulation are: $\omega_{0s}/\omega_{0n} = 1.00023, \gamma_{1n}/\omega_{0n} = 2.5\cdot10^{-3}, \gamma_{1s}/\omega_{0n} = 1.5\cdot10^{-3}, \gamma_{2n}/\omega_{0n} = 2.75\cdot10^{-3}, \gamma_{2s}/\omega_{0n} = 5\cdot10^{-3}, \alpha_n = 0.8, \alpha_s = 1, g = 9\cdot10^{-4}, \rho = 9\cdot10^{-13}$.

to increasing values of b^{in}, the drive amplitude. The simulation parameters used are listed in the figure caption. The blue solid line represents the valid superconducting WL steady state solution ($E < E_s$), while the green dotted line represents the invalid steady state solution ($E > E_s$). Similar lines are plotted for the normal WL steady state solution. The red solid line represents the valid solution ($E > E_n$), while the cyan dotted line represents the invalid one ($E < E_n$). For the simulation parameters chosen in plot (a), the superconducting WL steady state solution is valid at all frequencies (the blue line) and thus the system follows this resonance lineshape as the frequency is scanned back and forth. In plot (b) corresponding to a higher amplitude drive, the superconducting WL steady state solution is not valid at all frequencies, thus as the superconducting WL solution becomes invalid under forward frequency sweep, the system jumps to the valid normal WL steady state solution as indicated by the downward arrow at the left side of the resonance. As we continue to sweep the frequency forward, another jump occurs at the right side of the resonance back to the blue solid line (indicated by the upward arrow) as the normal WL steady state solution becomes invalid. Sweeping the frequency in the backward direction exhibits hysteresis in the response lineshape, since the opposed jumps differ, as can be clearly seen in plot (b). As we increase the amplitude drive b^{in} further [see plot (c)], we successfully obtain a case where the two opposed jumps at the right side of the resonance are in close proximity of each other. Whereas in plot (d) corresponding to a higher amplitude drive one gets a frequency region (see the right side of the resonance) where no steady state solution is valid. This result may potentially explain the third enlarged hysteresis loop which appears in Fig. 9, where the two opposed jumps occur earlier in each frequency sweep direction. That is if one assumes the existence of additional two valid solutions within the "invalid region" which the system jumps to, and which coincide with the existing valid solutions outside this region. Such additional solutions can possibly originate from another WL becoming active at these higher amplitude drives. Moreover the assumption of different WL becoming active may be needed also to account for the multiple jumps feature presented in Figs. 5 and 10.

VIII. Conclusion

In the course of this experimental work, we have fabricated several stripline NbN resonators dc-magnetron sputtered on sapphire substrates at room temperature implementing different geometries. The resonators have exhibited similar and unusual nonlinear effects in their resonance response curves. The onset of the nonlinear effects in these NbN resonators varied between the different resonators, but usually occurred at relatively low microwave powers, typically 2–3 orders of magnitude lower than Nb for example. Among the nonlinear effects observed: abrupt and multiple jumps in the resonance curve, power dependent resonance frequency shift, hysteresis loops in the vicinity of the jumps, hysteresis loops changing direction, and critical coupling phenomenon. Weak links forming in the NbN films are hypothesized as the source of the nonlinearities. Further study of these effects under other modes of operation and measurement conditions would be carried in the future, in order to substantiate our understanding of these extraordinary effects.

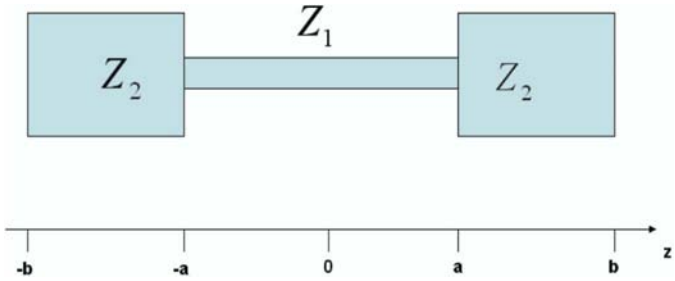

Fig. 15. Geometry model.

Appendix I
Resonance Frequency Calculation of B1, B2, B3 Resonators

The calculation process of the resonance frequencies of B1 and B2 makes use of opposite traveling voltage-current waves method [48], [49]. For this purpose, we model B1 and B2 resonators as a straight transmission line extending in the z-direction with two characteristic impedance regions Z_1 and Z_2 as shown in Fig. 15.

The equivalent voltage along the resonator transmission line would be given, in general, by a standing waves expression in the form

$$V(z) = \begin{cases} A_+ \cos\beta(z-a) + B_+ \sin\beta(z-a) & z\epsilon(a,b) \\ A\cos\beta z + B\sin\beta z & z\epsilon(-a,a) \\ A_- \cos\beta(z+a) + B_- \sin\beta(z+a) & z\epsilon(-b,-a) \end{cases} \tag{19}$$

where β ($= 2\pi f\sqrt{\varepsilon_r}/c$) is the propagation constant along the transmission line, and A_+, B_+, A, B, A_-, B_- are constants that can be determined using boundary conditions. However due to the symmetry of the problem $z \longleftrightarrow -z$, we expect the solutions to have defined parity, where $V(z) = V(-z)$ for symmetric solution and $V(z) = -V(-z)$ for antisymmetric solution. Thus by taking advantage of this property and demanding that $V(z)$ be continuous at $z = a$ and $z = -a$, one gets:

$$V_{\text{sym}}(z) = \begin{cases} \cos\beta a\cos\beta(z-a) & \\ +B_s\sin\beta(z-a), & z\epsilon(a,b) \\ \cos\beta z, & z\epsilon(-a,a) \\ \cos\beta a\cos\beta(z+a) & \\ -B_s\sin\beta(z+a), & z\epsilon(-b,-a) \end{cases}$$

$$V_{\text{anti}}(z) = \begin{cases} \sin\beta a\cos\beta(z-a) & \\ +B_a\sin\beta(z-a), & z\epsilon(a,b) \\ \sin\beta z, & z\epsilon(-a,a) \\ -\sin\beta a\cos\beta(z+a) & \\ +B_a\sin\beta(z+a), & z\epsilon(-b,-a) \end{cases}$$

where $V_{\text{sym}}(z)$ stands for the symmetric solution whereas $V_{\text{anti}}(z)$ for the antisymmetric solution. To calculate the value

of the new constants B_s, B_a, we require that the equivalent current $I(z)$ along the transmission line, which is given by $I(z) = (i/\beta Z_i)dV/dz$ where Z_i is the characteristic impedance of the line (in the $i = 1, 2$ region), be continuous at $z = a$ and $z = -a$. Following this requirement one gets $B_s = -\eta \sin(\beta a)$ and $B_a = \eta \cos(\beta a)$, where $\eta = Z_2/Z_1$.

A. B1 Resonator

Since the resonator ends are shorted we demand $V(b) = V(-b)$.

The symmetric case:

In this case, we either have maximum or minimum at $V(b)$ thus we get $I(b) = 0$, yielding the following condition on the resonance frequencies

$$\cos(\beta a)\sin(\beta(b-a)) + \eta \sin(\beta a)\cos(\beta(b-a)) = 0 \quad (20)$$

The antisymmetric case:

From the antisymmetric $V(-b) = -V(-b)$ and the continuity $V(b) = V(-b)$ conditions, we get $V(b) = V(-b) = 0$, which yields

$$\sin(\beta a)\cos(\beta(b-a)) + \eta \cos(\beta a)\sin(\beta(b-a)) = 0 \quad (21)$$

Substituting the following numerical values $\eta = Z_2/Z_1 = 0.5, l_1 = a = 13$ mm, $l_2 = b - a = 6.5$ mm into the above resonance frequency conditions and solving for frequencies below 10 GHz, yield the following solutions (2.5035 GHz, 5.697 GHz, 8.1647 GHz) for the symmetric case, and (2.9804 GHz, 5.1786 GHz, 8.1647 GHz) for the antisymmetric case, with doubly degenerate mode at 8.1647 GHz. By comparing these calculated resonances to the directly measured resonances of B1 resonator, obtained using a broadband S_{11} measurement (2.5812 GHz, 5.6304 GHz, 8.4188 GHz), we find that the excited resonances correspond to the symmetrical case only. The antisymmetric modes do not get excited because they have a voltage node at the feedline position.

B. B2 Resonator

Since the resonator ends are open-circuited, we demand $I(b) = I(-b) = 0$.

The symmetric case:

We require that the current associated with the symmetric voltage, vanishes:

$$\cos(\beta a)\sin[\beta(b-a)] + \eta \sin(\beta a)\cos[\beta(b-a)] = 0 \quad (22)$$

The antisymmetric case:

We require that the current associated with the antisymmetric voltage, vanishes:

$$-\sin(\beta a)\sin(\beta(b-a)) + \eta \cos(\beta a)\cos\beta(b-a) = 0 \quad (23)$$

Substituting the following numerical values $\eta = Z_2/Z_1 = 49.9/10.4 = 4.79, l_1 = a = 11.97$ mm, $l_2 = b - a = 6.43$ mm into the above resonance frequency conditions and solving for frequencies below 10 GHz, yield the following solutions (2.6486 GHz, 6.0288 GHz, 8.5588 GHz) for the symmetric case, and (1.1763 GHz, 4.3698 GHz, 7.4597 GHz, 9.7778 GHz for the antisymmetric case. By comparing these calculated resonances to the directly measured resonances of B2 resonator, obtained using a broadband S_{11} measurement (2.5152 GHz, 4.425 GHz, 6.3806 GHz, 8.176 GHz), we find a good agreement between the two results. The missing resonances do not get excited apparently because of the coupling location of the feedline relative to the resonator.

C. B3 Resonator

B3 resonator, in contrast, showed some larger discrepancy between the measured value for the first mode ~ 1.6 GHz (seen in Fig. 5) and the theoretical value $f_1 = 2.4462$ GHz calculated according to the approximated equation:

$$f_n = \frac{nc}{2l\sqrt{\varepsilon_r}} \quad (24)$$

where n is the mode number, c is the light velocity, l is the open-circuited line length ($\simeq$20 mm), and ε_r is the relative dielectric coefficient of the sapphire ($\simeq 9.4$).

ACKNOWLEDGMENT

E. Buks would like to thank M. L. Roukes for supporting the early stage of this research and for many helpful conversations and invaluable suggestions. Very helpful conversations with G. Eisenstein, O. Gottlieb, G. Koren, E. Polturak, and B. Yurke are also gratefully acknowledged.

REFERENCES

[1] J. Halbritter, "RF residual losses,surface impedance and granularity in superconducting cuprates," *J. Appl. Phys.*, vol. 68, p. 6315, Dec. 1990.

[2] M. A. Golosovsky, H. J. Snortland, and M. R. Beasley, "Nonlinear microwave properties of superconducting Nb microstrip resonators," *Phys. Rev. B.*, vol. 51, p. 6462, Mar. 1995.

[3] S. K. Yip and J. A. Sauls, "Nonlinear Meissner effect in CuO Superconductors," *Phys. Rev. Lett.*, vol. 69, p. 2264, Oct. 1992.

[4] J. Wosik, L.-M. Xie, J. Mazierska, and R. Grabovickic, "Influence of columnar defects on surface resistance of YBaCuO superconducting thin films; nonlinear effects," *Appl. Phys. Lett.*, vol. 75, p. 1781, Sept. 1999.

[5] D. E. Oates, M. A. Hein, P. J. Hirst, R. G. Humphreys, G. Koren, and E. Polturak, "Nonlinear microwave surface impedance of YBCO films: Latest results and present understanding," *Physica C*, vol. 372, pp. 462–468, 2002.

[6] S. M. Anlage, W. Hu, C. P. Vlahacos, D. Steinhauer, B. J. Feenstra, S. K. Dutta, A. Thanawalla, and F. C. Wellstood, "Microwave nonlinearities in high-T_c superconductors: The truth is out there," *J. Supercond.*, vol. 12, p. 353, 1999.

[7] T. Dahm and D. J. Scalapino, "Theory of intermodulation in a superconducting microstrip resonator," *J. Appl. Phys.*, vol. 81, p. 2002, Feb. 1997.

[8] D. E. Oates, S.-H. Park, M. A. Hein, P. J. Hirst, and R. G. Humphreys, "Intermodulation distortion and third-harmonic generation in YBCO films of varying oxygen content," *IEEE Trans. Appl. Supercond.*, vol. 13, no. 2, pp. 311–314, Jun. 2003.

[9] T. Dahm and D. J. Scalapino, "Analysis and Optimization of intermodulation in high T_c superconducting microwave filter design," *IEEE Trans. Appl. Supercond.*, vol. 8, no. 4, pp. 149–157, Dec. 1998.

[10] C. C. Chen, D. E. Oates, G. Dresselhaus, and M. S. Dresselhaus, "Nonlinear electrodynamics of superconducting NbN and Nb thin films at microwave frequencies," *Phys. Rev. B.*, vol. 45, p. 4788, Mar. 1992.

[11] J. Wosik, L.-M. Xie, J. H. Miller, Jr., S. A. Long, and K. Nesteruk, "Thermally-induced nonlinearities in the surface impedance of superconducting YBCO thin films," *IEEE Trans. Appl. Supercond.*, vol. 7, no. 2, pp. 1470–1473, Jun. 1997.

[12] B. A. Willemsen, J. S. Derov, J. H. Silva, and S. Sridhar, "Nonlinear response of suspended high temperature superconducting thin film microwave resonators," *IEEE Trans. Appl. Supercond.*, vol. 5, no. 2, pp. 1753–1755, Jun. 1995.

[13] L. F. Cohen, A. L. Cowie, A. Purnell, N. A. Lindop, S. Thiess, and J. C. Gallop, "Thermally induced nonlinear behavior of HTS films at high microwave power," *Supercond. Sci. Technol.*, vol. 15, p. 559, 2002.

[14] A. M. Portis, H. Chaloupka, M. Jeck, and A. Pischke, "Power-induced switching of an HTS microstrip patch antenna," *Superconduct. Sci. Technol.*, vol. 4, no. 9, p. 436, Sep. 1991.

[15] S. J. Hedges, M. J. Adams, and B. F. Nicholson, "Power dependent effects observed for a superconducting stripline resonator," *Elect. Lett.*, vol. 26, no. 14, Jul. 1990.

[16] J. Wosik, L.-M. Xie, R. Grabovickic, T. Hogan, and S. A. Long, "Microwave power handling capability of HTS superconducting thin films: Weak links and thermal effects induced limitation," *IEEE Trans Appl. Supercond.*, vol. 9, no. 2, pp. 2456–2459, Jun. 1999.

[17] Z. Wang, A. Kawakami, Y. Uzawa, and B. Komiyama, "Superconducting properties and crystal structures of single-crystal niobium nitride thin films deposited at ambient substrate temperature," *J. Appl. Phys.*, vol. 79, p. 7837, Feb. 1996.

[18] D. D. Bacon, A. T. English, S. Nakahara, F. G. Peters, H. Schreiber, W. R. Sinclair, and R. B. van Dover, "Properties of NbN thin films deposited on ambient temperature substrates," *J. Appl. Phys.*, vol. 54, p. 6509, Jul. 1983.

[19] S. Thakoor, J. L. Lamb, A. P. Thakoor, and S. K. Khanna, "High T_c superconducting NbN films deposited at room temperature," *J. Appl. Phys.*, vol. 58, p. 4643, Dec. 1985.

[20] P. Yagoubov, G. Gol'tsman, B. Voronov, L. Seidman, V. Siomash, S. Cherednichenko, and E. Gershenzon, "The bandwidth of HEB mixers employing ultrathin NbN films on sapphire substrate," in *7th Int. Symp. Space Terahertz Technol.*, Mar. 1996, p. 290.

[21] A. C. Anderson, D. J. Lichtenwalner, and W. T. Brogan, "Process control for the low temperature deposition of niobium-nitride thin films," *IEEE Trans. Mag.*, vol. 25, no. 2, pp. 2084–2088, Mar. 1989.

[22] Y. Pellan, G. Dousselin, J. Pinel, and Y. U. Sohn, "Temperature and magnetic field dependence of NbN film resistivity: 3D weak localization effects," *J. Low Temp. Phys.*, vol. 78, p. 60, Jun. 1990.

[23] H. C. Jones, "Some properties of granular thin films of high-field superconductors," *Appl. Phys. Lett.*, vol. 27, p. 471, Oct. 1975.

[24] Y. M. Shy, L. E. Toth, and R. Somasundaram, "Superconducting properties, electrical resistivities, and structure of NbN thin films," *J. Appl. Phys.*, vol. 44, p. 5539, Dec. 1973.

[25] H. L. Hoetal, R. T. Kampwirth, K. E. Gray, D. W. Capone II, L. S. Chumbley, and M. MeshII, "Electron microscopy study of sputtered NbN films," *Ultramicroscopy*, vol. 22, p. 297, Apr. 1987.

[26] S. Isagawa, "RF superconducting properties of reactively sputtered NbN," *J. Appl. Phys.*, vol. 52, p. 921, Oct. 1980.

[27] D. E. Oates, A. C. Anderson, and P. M. Mankiewich, "Measurement of the surface resistance of $YBa_2Cu_3O_{7-x}$ thin films using stripline resonators," *J. Supercond.*, vol. 3, p. 251, 1990.

[28] D. E. Oates, A. C. Anderson, D. M. Sheen, and S. M. Ali, "Stripline resonator measurements of Z_s versus H_{RF} in $YBa_2Cu_3O_{7-x}$ thin films," *IEEE Trans. Microw. Theory Tech.*, vol. 39, no. 2, pp. 1522–1529, Sep. 1991.

[29] E. H. Rhoderick and E. M. Wilson, "Current distribution in thin superconducting films," *Nature*, vol. 194, p. 1167, Jun. 1962.

[30] R. Hu, G. L. Kerber, J. Luine, E. Ladizinsky, and J. Bulman, "Sputter deposition conditions and penetration depth in NbN thin films," *IEEE Trans. Appl. Supercond.*, vol. 13, no. 2, pp. 3288–3291, Jun. 2003.

[31] A. Andreone, A. Cassinese, A. Di Chiara, M. Lavarone, F. Palomba, A. Ruosi, and R. Vaglio, "Nonlinear microwave properties of Nb_3Sn sputtered superconducting films," *J. Appl. Phys.*, vol. 82, p. 1736, Aug. 1997.

[32] P. P. Nguyen, D. E. Oates, G. Dresselhaus, and M. S. Dresselhaus, "Nonlinear surface impedance for $YBa_2Cu_3O_{7-x}$ thin films: Measurements and a coupled-grain model," *Phys. Rev. B*, vol. 48, p. 6400, Sep. 1993.

[33] P. P. Nguyen, D. E. Oates, G. Dresselhaus, M. S. Dresselhaus, and A. C. Anderson, "Microwave hysteretic losses in $YBa_2Cu_3O_{7-x}$ and NbN thin films," *Phys. Rev. B*, vol. 51, p. 6686, Mar. 1995.

[34] H. Xin, D. E. Oates, G. Dresselhaus, and M. S. Dresselhaus, "Microwave-frequency vortex dynamics in YBCO grain boundaries," *J. Supercond.*, vol. 14, p. 637, Oct. 2001.

[35] D. E. Oates, H. Xin, G. Dresselhaus, and M. S. Dresselhaus, "Intermodulation distortion and Josephson vortices in YBCO bicrystal grain boundaries," *IEEE Trans. Appl. Supercond.*, vol. 11, no. 1, pp. 2804–2807, Mar. 2001.

[36] B. Yurke and E. Buks, "Performance of capacity-parametric amplifiers, employing Kerr nonlinearities in the presence of two-photon loss," *J. Lightw. Technol.*, vol. 24, no. 12, Dec. 2006, to be published.

[37] J. H. Oates, R. T. Shin, D. E. Oates, M. J. Tsuk, and P. P. Nguyen, "A nonlinear transmission line model for superconducting stripline resonators," *IEEE Trans. Appl. Superconduct.*, vol. 3, no. 1, pp. 17–22, Mar. 1993.

[38] H. Prance, T. D. Clark, R. Whiteman, R. J. Prance, M. Everitt, P. Stiffel, and J. F. Ralph, "Pinch resonances in a radio-frequency-driven superconducting-quantum-interference-device ring-resonator system," *Phys. Rev. E*, vol. 64, p. 016208, Jun. 2001.

[39] R. Whiteman, J. Diggins, V. Schollmann, T. D. Clark, R. J. Prance, H. Prance, and J. F. Ralph, "Opposed (hammerhead) bifurcations in the resonant lineshape of a strongly driven SQUID ring-tank circuit system," *Phys. Lett. A*, vol. 234, p. 205, Sept. 1997.

[40] R. J. Prance, R. Whiteman, T. D. Clark, H. Prance, V. Schollmann, J. F. Ralph, S. Al-Khawaja, and M. Everitt, "Nonlinear multilevel dynamics of a coupled SQUID ring-resonator system in the hysteretic regime," *Phys. Rev. Lett.*, vol. 82, p. 5401, Jun. 1999.

[41] J. Halbritter, "Granular superconductors and their intrinsic and extrinsic surface impedance," *J. Supercond.*, vol. 8, p. 691, 1995.

[42] A. VI. Gurevich and R. G. Mints, "Self-heating in normal metals and superconductors," *Rev. Mod. Phys.*, vol. 59, p. 941, Oct. 1987.

[43] C. W. Gardinar and M. J. Collett, "Input and output in damped quantum systems: Quantum stochastic differential equations and the master equation," *Phys. Rev. A*, vol. 31, p. 3761, June 1985.

[44] K. Weiser, U. Strom, S. A. Wolf, and D. U. Gubserm, "Use of granular NbN as a superconducting bolometer," *J. Appl. Phys.*, vol. 52, p. 4888, Jul. 1981.

[45] A. M. Kadin and M. W. Johnson, "Nonequilibrium photon-induced hotspot: A new mechanism for photodetection in ultrathin metalic films," *Appl. Phys. Lett.*, vol. 69, p. 3938, Dec. 1996.

[46] W. J. Skocpol, M. R. Beasley, and M. Tinkham, "Self-heating hotspots in superconducting thin-film microbridges," *J. Appl. Phys.*, vol. 45, p. 4054, Sep. 1974.

[47] M. W. Johnson, A. M. Herr, and A. M. Kadin, "Bolometric and nonbolometric infrared photoresponses in ultrathin superconducting NbN films," *J. Appl. Phys.*, vol. 79, p. 7069, May 1996.

[48] P. Gardner, D. K. Paul, and K. P. Tan, "Planar microstrip ring resonator filters," in *Colloquium on Microwave Filters and Antennas for Personal Communication Systems Digest*, Feb. 1994, vol. 6, pp. 1–6.

[49] K. Chang, S. Martin, F. Wang, and J. L. Klein, "On the study of microstrip ring and varactor-tuned ring circuits," *IEEE Trans. Microw. Tech.*, vol. 35, no. 12, pp. 1288–1295, Dec. 1987.

Baleegh Abdo (S'02) was born in Haifa, Israel, in 1979. He received the B.Sc. degree in computer engineering and the M.Sc. degree in electrical engineering, in 2002 and 2004, respectively, from the Technion-Israel Institute of Technology, Haifa, Israel, where he is currently working toward the Ph.D. degree in electrical engineering. His graduate research interests are nonlinear effects in superconducting resonators in the microwave regime, resonator coupling, and quantum qubits.

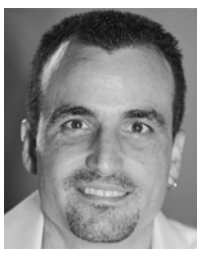

Eran Arbel-Segev was born in Haifa, Israel, in 1975. He received the B.Sc. degree in computer engineering and the M.Sc. degree in electrical engineering, in 2003 and 2006, respectively, from the Technion-Israel Institute of Technology, Haifa, Israel, where he is currently working toward the Ph.D. degree in electrical engineering. His research is focused on parametric gain in superconducting microwave resonators.

Oleg Shtempluck was born in Moldova, in 1949. He received the M.Sc. degree in electronic engineering from the Physical Department, Chernovtsy State University, Ukraine (former Soviet Union), in 1978. His research concerned semiconductors and dielectrics.

From 1983 to 1992, he was a team leader in the division of design engineering in Electronmash and from 1992 to 1999, he worked as stamp and mould design engineer at Ikar Company, both in Ukraine. Currently, he is working as a laboratory engineer in Microelectronics Research Center, Technion—Israel Institute of Technology, Haifa, Israel.

Eyal Buks received the B.Sc. degree in mathematics and physics from the Tel-Aviv University, Tel-Aviv, Israel, in 1991 and the M.Sc. and Ph.D. degrees in physics from the Weizmann Institute of Science, Israel, in 1994 and 1998, respectively. His graduate work concentrated on interference and dephasing in mesoscopic systems.

From 1998 to 2002, he worked at the California Institute of Technology (Caltech), Pasadena, as a Postdoctoral Scholar studying experimentally nanomachining devices. He is currently a Senior Lecturer at the Technion-Israel Institute of Technology, Haifa. His current research is focused on nanomachining and mesoscopic physics.

4.2 Nonlinear dynamics in the line shape of NbN superconducting resonators

Nonlinear dynamics in the resonance line shape of NbN superconducting resonators

B. Abdo,* E. Segev, O. Shtempluck, and E. Buks
Microelectronics Research Center, Department of Electrical Engineering, Technion, Haifa 32000, Israel
(Received 23 May 2005; revised manuscript received 5 December 2005; published 17 April 2006)

We report on unusual nonlinear dynamics observed in the resonance response of NbN superconducting microwave resonators. The nonlinear dynamics which occurs at relatively low input powers (2–4 orders of magnitude lower than Nb) includes among others, jumps in the resonance line shape, hysteresis loops changing direction, and resonance frequency shift. These effects are measured herein using varying input power, applied magnetic field, white noise, and rapid frequency sweeps. Based on these measurement results, we consider a hypothesis according to which local heating of weak links forming at the boundaries of the NbN grains is responsible for the observed behavior, and we show that most of the experimental results are qualitatively consistent with such a hypothesis.

DOI: 10.1103/PhysRevB.73.134513 PACS number(s): 74.50.+r, 85.25.−j, 47.20.Ky, 05.45.Xt

I. INTRODUCTION

Understanding the underlying mechanisms that cause and manifest nonlinear effects in superconductors has a significant implications for both basic science and technology. Nonlinear effects in superconductors may be exploited to demonstrate some important quantum phenomena in the microwave regime as was shown in Refs. 1 and 2 and as was suggested recently in Refs. 3 and 4, whereas, technologically, these effects, in general, can play a positive or negative role depending on the application. On the one hand, they are very useful in a wide range of nonlinear devices such as amplifiers,[5,6] mixers,[7] single-photon detectors,[8] and superconducting quantum interference devices (SQUID's).[9] On the other hand, in other applications mainly in the telecommunication area, such as bandpass filters and high-Q resonators, nonlinearities are highly undesirable.[10–13]

Various nonlinear effects in superconductors and in NbN in particular have been reported and analyzed in the past by several research groups. Duffing-like nonlinearity, for example, was observed in superconducting resonators employing different geometries and materials. It was observed in a high-T_c superconducting (HTS) parallel-plate resonator,[14] in a Nb microstrip resonator,[15] in Nb and NbN stripline resonators,[13] in a YBCO coplanar-waveguide resonator,[16] in a YBCO thin-film dielectric cavity,[17] and also in a suspended HTS thin-film resonator.[18] Other nonlinearities including notches, anomalies developing at the resonance line shape, and frequency hysteresis were reported in Refs. 19–21.

However, in spite of the intensive study of nonlinearities in superconductors in the past decades and the great progress achieved in this field, the determination of the underlying mechanisms responsible for the microwave nonlinear behavior of both low- and high-T_c superconductors is in many experiments still a subject of debate.[22] This is partly because of the variety of preparation and characterization techniques employed and the numerous fabrication parameters involved. In addition nonlinear mechanisms in superconductors, which are usually divided into intrinsic and extrinsic, are various and many times act concurrently. Thus identifying the dominant mechanism is in general difficult.[23]

Among the nonlinear mechanisms investigated in superconductors one can name the Meissner effect,[24] pair-breaking, global, and local heating effects,[14,17] rf and dc vortex penetration and motion,[25] defect points, damaged edges,[26] substrate material,[27] and weak links (WL's),[28] where WL is a collective term which represents various material defects such as weak superconducting points switching to normal state under low current density, Josephson junctions forming inside the superconductor structure, grain boundaries, voids, insulating oxides, and insulating planes. These defects and impurities generally affect the conduction properties of the superconductor and as a result cause extrinsic nonlinear effects.

In this paper we report the observation of unique nonlinear effects measured in the resonance line shape of NbN superconducting microwave resonators. Among the observed effects are asymmetric resonances, multiple jumps in the resonance curve, hysteretic behavior in the vicinity of the jumps, frequency hysteresis loops changing direction, jump frequency shift as the input power is increased, and nonlinear coupling. Some of these nonlinear effects were introduced by us in a previous publication.[29] Thus this paper will focus on presenting a more current set of measurements applied to these nonlinear resonators, which provides a better understanding of the underlying physical mechanism causing these effects. To this end, we have measured the nonlinear superconducting resonators using different operating conditions, such as bidirectional frequency sweeps, added white noise, fast frequency sweep using frequency modulation (FM), and dc magnetic fields. In each case we observe a unique nonlinear dynamics of the resonance line shape which is qualitatively different from the commonly reported Duffing oscillator nonlinearity. We attribute these nonlinear effects to WL's forming at the boundaries of the NbN columnar structure. A theoretical model explaining the dynamical behavior of the resonance line shape in terms of abrupt changes in the macroscopic parameters of the resonator, due to local heating, is formulated. Furthermore, simulations based on this model are shown to be in very good qualitative agreement with the experimental results.

The remainder of this paper is organized as follows: The fabrication process of the NbN superconducting resonators is described briefly in Sec. II. The nonlinear response of these resonators measured using various operating conditions are

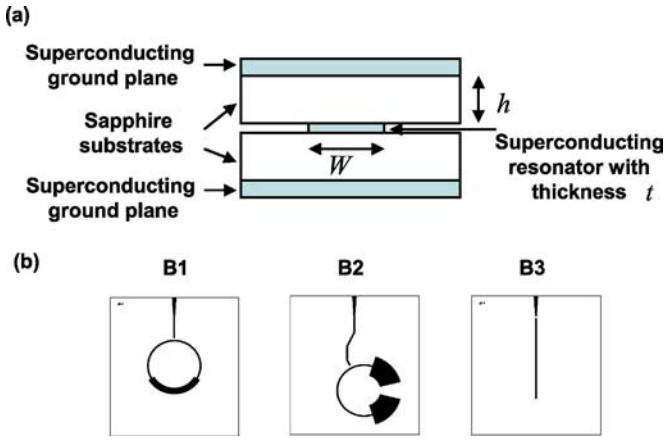

FIG. 1. (Color online). (a) Schematic cross section of the stripline geometry used, which consists of five layers: two superconducting ground planes, two sapphire substrates, and a NbN film in the middle deposited on one of the sapphires. (b) Top view of the three resonator layouts (B1, B2, B3) which were deposited as the center layer.

reviewed in Sec. III. A comparison with other nonlinearities reported in the literature is given in Sec. IV. The possible underlying physical mechanisms responsible for the observed effects are discussed in Sec. V, whereas in Sec. VI, a theoretical model based on local heating of weak links is suggested, followed by simulations which qualitatively reproduce most of the nonlinear features observed in the experiments. Finally, in Sec. VII, a short summary concludes this paper.

II. FABRICATION PROCESS

The measurement results presented in this paper belong to three nonlinear NbN superconducting microwave resonators. The resonators were fabricated using stripline geometry, which consists of two superconducting ground planes, two sapphire substrates, and a center strip deposited in the middle (the deposition was done on one of the sapphire substrates). Figure 1 shows a schematic diagram illustrating stripline geometry and a top view of the three resonator layouts. We will refer to the three resonators in the text by the names B1, B2 and B3 as defined in Fig. 1. The dimensions of the sapphire substrates used were 34 mm $\times$ 30 mm $\times$ 1 mm, whereas the coupling gap between the resonators and their feedline was set to 0.4 mm in the B1 and B3 and 0.5 mm in the B2 resonators. The resonators were dc magnetron sputtered in a mixed Ar/N_2 atmosphere, near room temperature. The patterning was done using the standard UV photolithography process, whereas the NbN etching was performed by Ar-ion milling. The sputtering parameters and design considerations as well as physical properties of the NbN films can be found elsewhere.[29] The critical temperature T_c of the B1, B2, and B3 resonators was relatively low and equal to 10.7 K, 6.8 K, and 8.9 K, respectively. The thickness of the NbN resonators was 2200 Å in the B1, 3000 Å in the B2, and 2000 Å in the B3 resonators.

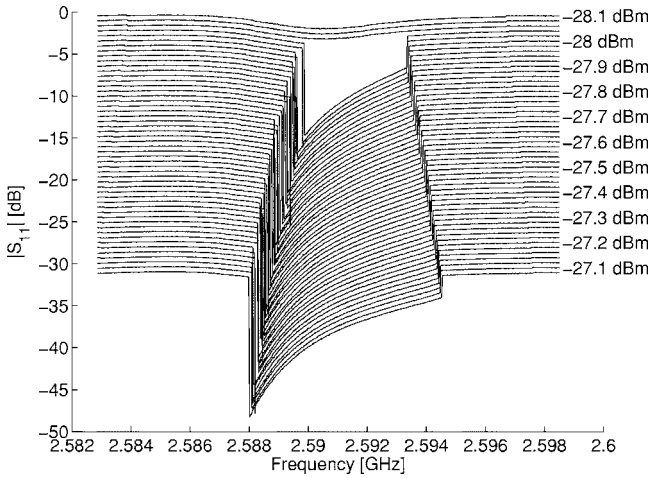

FIG. 2. S_{11} amplitude measurement of the B1 resonator at its first mode. The measured resonance line shapes are asymmetrical and contain two abrupt jumps at the sides of the resonance. Moreover, the jump frequencies shift outwards as the input power is increased. The measured resonance line shapes were shifted vertically by a constant offset for clarity.

III. NONLINEAR RESONANCE RESPONSE

In the following subsections, we present experimental results emphasizing the different aspects of the nonlinear response exhibited by the B1, B2, and B3 resonators. In Sec. III A, a resonance response measurement obtained while varying the input rf power is presented, showing an abrupt and low-power onset of nonlinearity. In Secs. III B–III D,, representative experimental results measured while scanning the resonance response in the forward and backward directions are shown, exhibiting, respectively, hysteresis loops changing direction, metastability, and multiple jumps, whereas in Sec. III E, the dependence of the resonance line shape on the applied dc magnetic field is examined, where the resonance line shape exhibits a change in the direction of the jump and vanishing jump features. All measurements presented were performed at liquid-helium temperature 4.2 K.

A. Abrupt onset of nonlinearity

In Fig. 2 we present a S_{11} parameter measurement of the B1 first mode using a vector network analyzer. At low input powers, the resonance response line shape is Lorentzian and symmetrical. As the input power is increased gradually in steps of 0.01 dBm, the resonance response changes dramatically and abruptly at about −28.04 dBm. It becomes extremely asymmetrical and includes two abrupt jumps at both sides of the resonance line shape. The magnitude of the jumps at some input powers can be as high as 16 dB. As the input power is increased the resonance frequency is redshifted and the jump frequencies shift outwards away from the center frequency. Moreover, at much higher powers not shown in the figure, the resonance curve becomes gradually shallower and broader in the frequency span. It is also worthwhile noting that the intensive evolution of the resonance

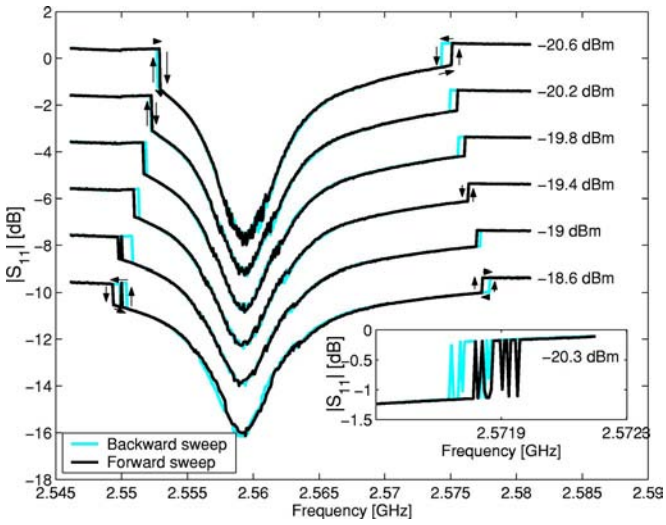

FIG. 3. (Color online). Frequency sweep measurement of the B1 resonator at its first mode performed in both frequency directions. The plots exhibit hysteresis loops forming at the vicinity of the jumps and hysteresis loops changing direction as the input power is increased. The black line represents a forward sweep, whereas the cyan (gray) line represents a backward sweep. The number of measurement points employed in each scan direction is 500 points. The resonance line shapes were shifted vertically by a constant offset for clarity. In the inset, a "zoom-in" measurement of the right hysteresis loop of the B1 first resonance is shown. The measurement, which was obtained using a spectrum analyzer, includes 100 data points and corresponds to −20.3 dBm input power.

line shape shown in Fig. 2 takes place within only a 1-dBm power range.

B. Hysteretic behavior

As the response function for nonlinear systems becomes multiple valued or lacks a steady-state solution in some parameter domain, nonlinear systems tend to demonstrate hysteretic behavior with respect to that parameter.

Frequency hysteresis in the resonance line shape of superconducting resonators exhibiting Duffing oscillator nonlinearity and other kinds of nonlinearities was observed by several groups.[19,30] Hysteretic behavior and losses in superconductors were discussed also in Refs. 25 and 31. Moreover, recent works, which examined the resonance response of a rf tank circuit coupled to a SQUID, have reported several interesting frequency hysteresis features.[32–34]

Likewise, measuring the resonance response of our nonlinear resonators yields a hysteretic behavior in the vicinity of the jumps. However, this hysteretic behavior is unique in many aspects. In Fig. 3 we show a S_{11} measurement of the B1 resonator at its first mode, measured while sweeping the frequency in both directions. The input power range shown in this measurement corresponds to a higher-power range than that of Fig. 2. The black line represents a forward frequency sweep, whereas the cyan (gray) line represents a backward frequency sweep.

At −20.6 dBm the resonance line shape contains two jumps in each scan direction and two hysteresis loops. The left hysteresis loop circulates clockwise whereas the right loop circulates counterclockwise. However, the common property characterizing them is that the jumps occur at higher frequencies in the forward scan compared to their counterparts in the backward scan. As the input power is increased to about −20.2 dBm the two opposed jumps at the left side meet and the left hysteresis loop vanishes. At about −19.4 dBm a similar effect happens to the right hysteresis loop, and it vanishes as well, whereas at higher input powers (i.e., −19 dBm, −18.6 dBm) the two jumps occur earlier at each frequency sweep direction, causing the hysteresis loops to appear circulating in the opposite direction compared to the −20.6-dBm resonance curve, for instance. As we show in the next subsection, this picture of well-defined hysteresis loops is strongly dependent on the applied frequency sweep rate and on the system noise. A possible explanation for this unique hysteretic behavior would be presented in Sec. VI.

C. Metastable states

Jumps in the resonance response of a nonlinear oscillator are usually described in terms of metastable and stable states and the dynamic transition between basins of attraction of the oscillator;[35] thus in order to examine the stability of these observed resonance jumps, we carried out several measurements.

In one measurement, we have "zoomed in" around the right jump of the resonance at −20.3 dBm and examined its frequency response in both directions. The measurement setup included a signal generator, the cooled resonator, and a spectrum analyzer. The reflected signal power off the resonator was redirected by a circulator and measured using a spectrum analyzer. The measurement result obtained using 100 sampling points in each direction is exhibited in the inset of Fig. 3, where the metastable nature of the jump region is clearly demonstrated.

In another measurement configuration we have investigated this metastability further by monitoring the effect of applied broadband noise on the resonance jumps. We applied a constant white-noise power to the resonator, several orders of magnitude lower than the main signal power. The applied white noise level was −58 dBm/Hz (measured separately using spectrum analyzer) and was generated by amplifying the thermal noise of a room-temperature 50-Ω load using an amplifying stage. The generated noise was added to the transmitted power of a network analyzer via a power combiner. The reflected power was redirected by a circulator and was measured at the second port of the network analyzer. The effect of the −58-dBm/Hz white-noise power on the B1 first-mode jumps is shown in Fig. 4(a), whereas in Fig. 4(b) we show for comparison the nearly noiseless case obtained after disconnecting the amplifier and combiner stage. The two measurements were carried out within the same input power range (from −23.9 dBm to −20 dBm).

By comparing the two measurement results, one can make the following observations. The twofold jumps in Fig. 4(b) form a hysteresis loop at both sides of the resonance curve. By contrast in Fig. 4(a), as a result of the added noise, the hysteresis loops at the right side vanish, while the jumps at

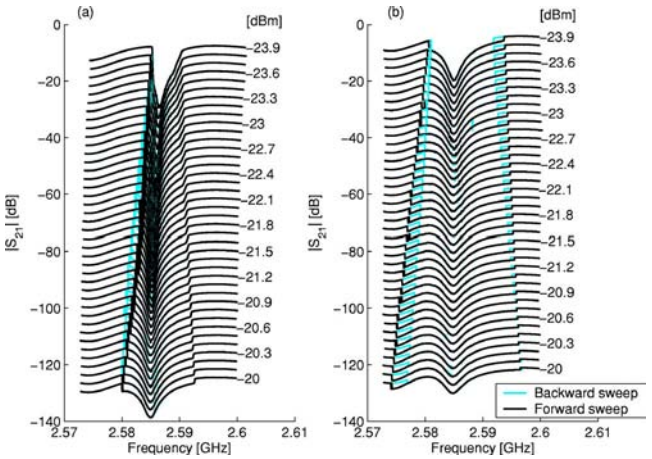

FIG. 4. (Color online). Frequency sweep measurement of the B1 resonator first mode performed in both directions while (a) applying white noise of −58 dBm/Hz (b) without applying external noise. The black line represents a forward sweep, whereas the cyan (gray) line represents a backward sweep. The measured resonance curves were shifted vertically by a constant offset for clarity.

the left side become frequent and bidirectional (indicated by the thick colored lines).

At a given input drive, the transition rate $\Gamma(f)$ between the oscillator basins of attraction can be generally estimated by the expression $\Gamma(f)=\Gamma_0\exp(-E_A(f)/k_BT_{eff})$,[35] where $E_A(f)$ is the quasiactivation energy of the oscillator, T_{eff} is proportional to the noise power, k_B is Boltzmann's constant, and f is the oscillator frequency, whereas Γ_0 is related to Kramers low-dissipation form[36] and it is given approximately by f_0/Q, where f_0 is the natural resonance frequency and Q is the quality factor of the oscillator. From our results we roughly estimate the order of magnitude of E_A to be 10^{14} K for the jump on the left.[35] Note, however, that this quantity varies for different transitions and strongly depends on the operating point.

D. Multiple jumps

Another nonlinear feature—namely, multiple jumps in the resonance line shape—is observed in the resonance response of B3, while sweeping the frequency in the forward and backward directions. In Fig. 5 we show a representative measurement of the first resonance of B3 corresponding to 1.49 dBm input power, exhibiting three jumps in each sweep direction and four hysteresis loops.

E. dc magnetic field dependence

Measuring the B2 resonator second mode under a dc magnetic field yielded additional nonlinear features in the resonance response line shape as shown in Figs. 6 and 7.

In Fig. 6 we show the resonance line shape of the B2 second mode measured while applying a perpendicular dc magnetic field of 90 mT. As the input rf power is increased gradually, the resonance line shape undergoes different phases. While at low and high powers the curves are Lorentzians and symmetrical, in the intermediate range, the resonance curves include a jump at the left side, which, as the input power increases, flips from the upward to the downward direction.

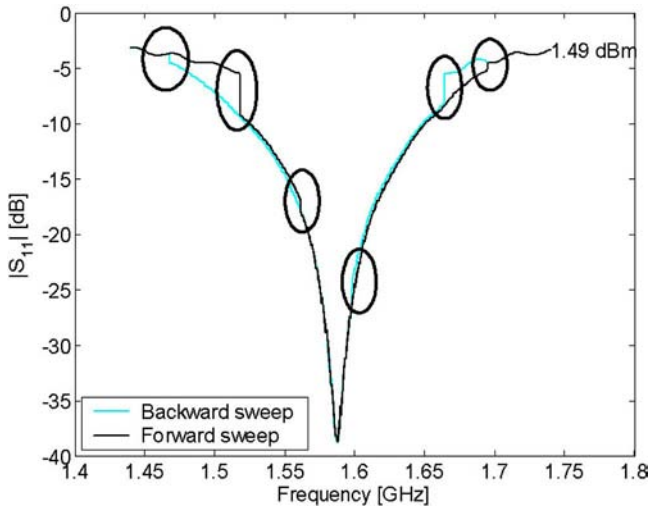

FIG. 5. (Color online). S_{11} amplitude measurement of the first resonance of the B3 resonator, measured at an input power of 1.49 dBm. The measurement was done using a network analyzer employing 4000 measurement points in each direction. The black line represents a forward frequency scan whereas the cyan (gray) line represents a backward frequency scan. The plot shows clearly three jumps within the resonance line shape in each direction, as indicated by small circles.

In Fig. 7, where we have set a constant input power of −5 dBm and increased the applied magnetic field by small steps, the left-side jump vanishes as the magnetic field exceeds some relatively low threshold of ~11.8 mT. These effects will be further discussed in Secs. V and VI.

IV. COMPARISON WITH OTHER NONLINEARITIES

The most commonly reported nonlinearity in superconductors is the Duffing oscillator nonlinearity. However, this

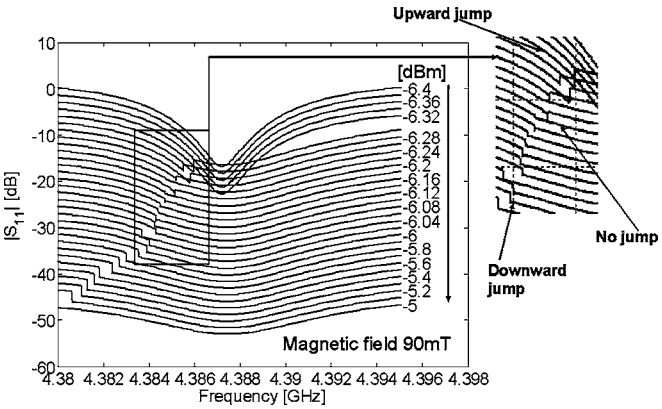

FIG. 6. B2 nonlinear resonance response measured under a constant magnetic field of 90 mT while increasing the input power. The resonance which starts as a Lorentzian at low powers, develops into a resonance curve having an upward jump, a curve with no jump, a curve having a downward jump, and finally a Lorentzian curve again as the power is increased. The measured curves were shifted vertically by a constant offset for clarity.

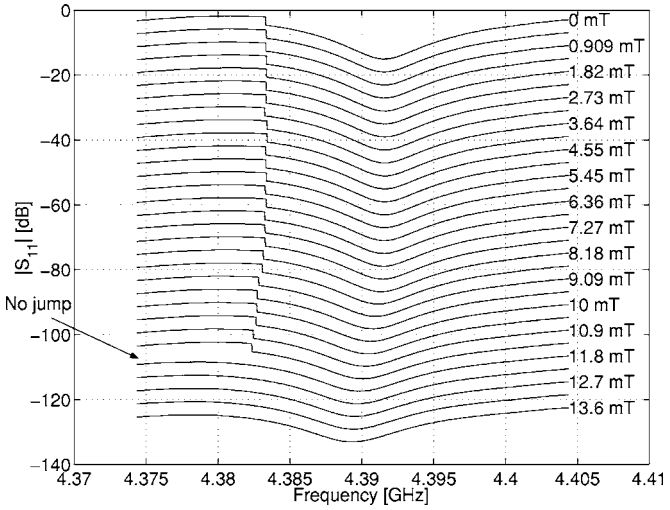

FIG. 7. Increasing the magnetic field gradually from zero while applying a constant input power level of −5 dBm causes the jump in the B2 resonance line shape to disappear at a relatively low value of 11.8 mT. This vanishing jump indicates that the jump mechanism is sensitive to the magnetic field. The measured curves were shifted vertically by a constant offset for clarity.

nonlinearity is qualitatively different from the nonlinearity we observe in our NbN samples and which is reported in this paper. In Fig. 8 we show, for the sake of visual comparison, a resonance response measured at 4.2 K, exhibiting Duffing oscillator nonlinearity of the kind generally reported in the literature.[13,14,16] This nonlinearity, which can be explained in terms of resistance change ΔR and kinetic inductance change ΔL_K,[10,30,37] was measured at the first resonance frequency of a 2200-Å-thick Nb resonator employing B2 layout geometry (T_c=8.9 K). The differences between the two nonlinear dynamics shown in Figs. 2 and 8 are obvious. In Fig. 8 the nonlinearity is gradual, while in Fig. 2 the power onset of nonlinearity is abrupt and sudden. In Fig. 8, the resonance response in the nonlinear regime contains an infinite slope at the left side, whereas in Fig. 2 the curves contain two jumps at both sides of the resonance response. In Fig. 8 changes in the resonance curve are measured on a power scale of 1 dBm, while changes in Fig. 2 are measured on a 0.01 dBm power scale. Whereas the onset of nonlinearity in Fig. 8 is on the order of 10 dBm, the onset of nonlinearity in Fig. 2 is about 4 orders of magnitude lower, ~−28 dBm. Furthermore, the presented nonlinearity differs from Duffing oscillator nonlinearity in its hysteretic behavior and its multiple-jump feature shown in Fig. 5.

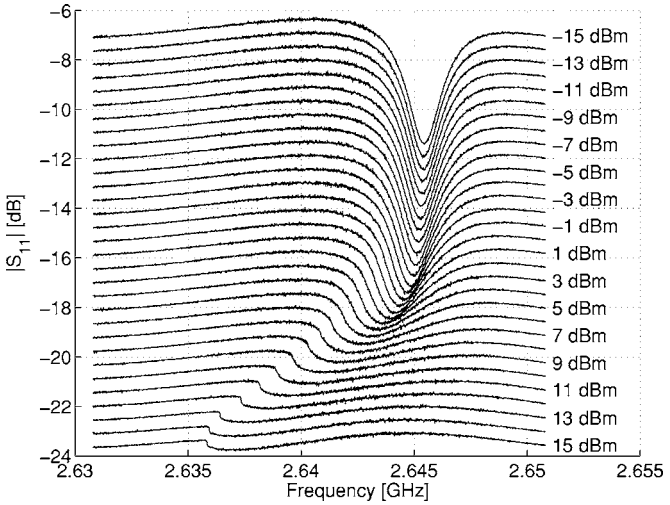

FIG. 8. Duffing oscillator nonlinearity exhibited by a Nb stripline resonator employing a B2 layout at its first mode. The different plots of the S_{11} amplitude correspond to different input powers, ranging from −15 dBm to 15 dBm in steps of 1 dBm. As the input power is increased the resonance becomes asymmetrical and an infinite slope builds up at the left side of the resonance curve. The plots were offset in the vertical direction for clarity.

Abrupt jumps in the resonance line shape, similar in some aspects to the jumps reported herein, were observed in two-port high-T_c YBCO resonators.[19–21] Portis *et al.*[19] have also reported some frequency hysteretic behavior in the vicinity of the jumps. However, one significant difference between the two nonlinearities is the onset power of nonlinearity reported in these references, which is on the order of 20 dBm[20,21]—that is, about 5 orders of magnitude higher than the onset power of nonlinearity of the B1 first mode (~−28 dBm). All three works[19–21] have attributed the nonlinear abrupt jumps to local heating of distributed WL's in the resonator film.

V. POSSIBLE NONLINEAR MECHANISMS

The relatively very low power onset of nonlinearity observed in these resonators as well as its strong sensitivity to rf power highly implies an extrinsic origin of these effects, and as such, hot spots in WL's are a leading candidate for explaining the nonlinearity.

Vortex penetration in the bulk or in WL's is less likely, mainly because heating the sample above T_c between sequential magnetic field measurements has yielded reproducible results with good accuracy in the magnetic field magnitude, the microwave input power, and the jump frequency (less than 200 kHz offset). Moreover, the low-magnetic-field threshold ~11.8 mT above which the B2 resonance jump vanished is about 3.5 times lower than the H_{c_1} (flux penetration) of NbN reported, for example, in Ref. 13.

In the following subsection, Sec. V A, we provide a direct evidence of WL, whereas in Sec. V B, we exclude the global heating mechanism as a possible source of the nonlinearities.

A. Columnar structure

It is well known from numerous research works done in the past[38,39] that NbN films can grow in a granular columnar structure under certain deposition conditions. Such columnar structure may even promote the growth of random WL's at the grain boundaries of the NbN films. To examine the NbN structure we have sputtered about a 2200-Å NbN film on a thin small rectangular sapphire substrate of 0.2 mm thickness. The sputtering conditions applied were similar to those used in the fabrication of the B2 resonator. Following the sputtering process, the thin sapphire was cleaved and a scan-

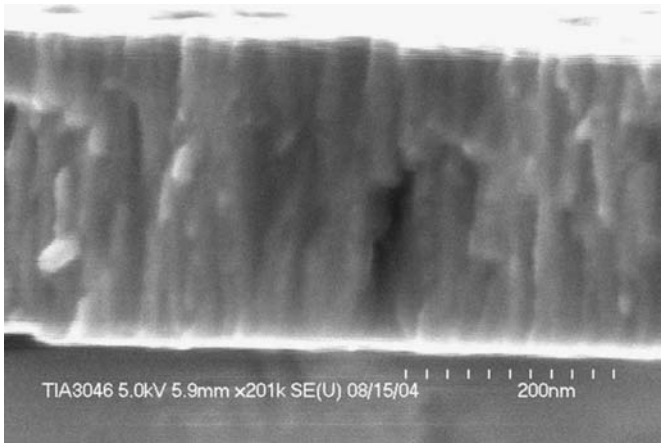

FIG. 9. A SEM micrograph showing a 2200-Å NbN film deposited on a thin sapphire substrate using similar sputtering conditions as the B2 resonator. The micrograph exhibits clearly the columnar structure of the NbN film and its grain boundaries.

ning electron microscope (SEM) micrograph was taken at the cleavage plane. The SEM micrograph appearing in Fig. 9, which shows clearly the columnar structure of the deposited NbN film and its grain boundaries, further supports the weak-link hypothesis. The typical diameter of each NbN column is about 20 nm.

B. Frequency sweep time analysis

Resistive losses and heating effects are typically characterized by relatively long time scales.[14] In an attempt to consider whether such effects are responsible for the observed nonlinearities in general and for the jumps in particular, we have run a frequency sweep time analysis using the experimental setup depicted in Fig. 10. We have controlled the frequency sweep cycle of a signal generator via FM modulation. The FM modulation was obtained by feeding the signal generator with a sawtooth wave form of $1/f$ sweep time cycle. The reflected power off the resonator was redirected

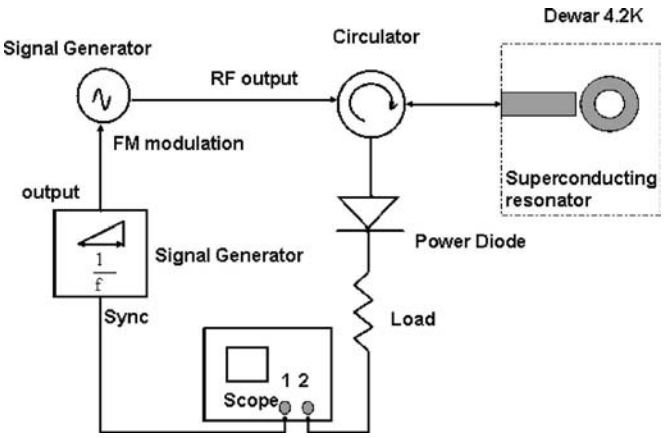

FIG. 10. Frequency sweep time analysis setup. The frequency sweep time of the microwave signal generator was FM modulated by a sawtooth wave form of frequency f. The reflected power off the resonator was measured by a power diode and an oscilloscope.

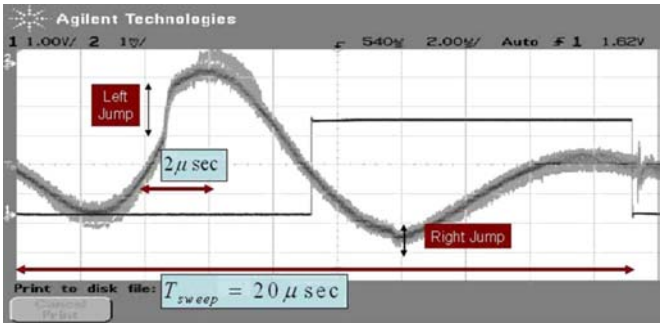

FIG. 11. (Color online). Frequency sweep time measurement. The figure displays the resonance measured by an oscilloscope while applying a sawtooth FM modulation of frequency 50 kHz ($T_{sweep}=20$ μs) to the signal generator. The left and right jumps of the resonance are still apparent in spite of the fast rate frequency sweep. Thus indicating that the jumps do not originate from any global heating mechanism.

using a circulator and measured by a power diode and an oscilloscope. The left- and right-hand jumps of B2 $\sim$4.39 GHz resonance were measured using this setup, while applying increasing FM modulation frequencies up to 200 kHz. In Fig. 11 we present a measurement result obtained at 50 kHz FM modulation or, alternatively, T_{sweep} of 20 μs. The FM modulation applied was $\pm$20 MHz around the center frequency 4.4022 GHz. The measured resonance response appears inverted in the figure due to the negative output polarity of the power diode. The fact that both jumps continue to occur within the resonance line shape (see Fig. 11), in spite of the short duty cycles that are of the order of $\sim\mu s$, indicates that heating processes which have typical time scales on the order of s to ms (Ref. 14) are unlikely to cause these effects.

However, the above measurement result does not exclude local heating of WL's.[40–42] Assuming that the substrate is isothermal and that the hot spot is dissipated mainly down into the substrate rather than along the film,[40] one can evaluate the characteristic relaxation time of the hot spot using the equation $\tau = Cd/\alpha$, where C is the heat capacity of the superconducting film (per unit volume), d is the film thickness, and α is the thermal surface conductance between the film and substrate.[41] Substituting for our B2 NbN resonator yields a characteristic relaxation time of $\tau \simeq 5.4\times10^{-8}$ s, where the parameters $C \simeq 2.7\times10^{-3}$ J cm^{-3} K^{-1} (NbN),[42] $d=3000$ Å (B2 thickness), and $\alpha \simeq 1.5$ W cm^{-2} K^{-1} at 4.2 K (sapphire substrate)[42] have been used. A similar calculation based on values given in Ref. 40 yields $\tau \simeq 2.1\times10^{-9}$ s. These time scales are of course 2–3 orders of magnitude lower than the time scales examined by the FM modulation setup, and thus local heating of WL's is not ruled out.

VI. LOCAL HEATING MODEL

In this section we consider a hypothesis according to which local heating of WL's is responsible for the observed effects. We show that this hypothesis can account for the main nonlinear features observed and that simulations based

on such a theoretical model exhibit a very good qualitative agreement with the experimental results.

A. Theoretical modeling

Consider a resonator driven by a weakly coupled feedline carrying an incident coherent tone $b^{in}e^{-i\omega_p t}$, where b^{in} is a constant complex amplitude and ω_p is the drive angular frequency. The mode amplitude inside the resonator A can be written as $A=Be^{-i\omega_p t}$, where $B(t)$ is a complex amplitude, which is assumed to vary slowly on the time scale of $1/\omega_p$. In this approximation, the equation of motion of B reads[3]

$$\frac{dB}{dt} = [i(\omega_p - \omega_0) - \gamma]B - i\sqrt{2\gamma_1}b^{in} + c^{in}, \tag{1}$$

where ω_0 is the angular resonance frequency, $\gamma=\gamma_1+\gamma_2$, γ_1 is the coupling constant between the resonator and feedline, and γ_2 is the damping rate of the mode. The term c^{in} represents input noise with vanishing average

$$\langle c^{in}\rangle = 0 \tag{2}$$

and correlation function given by

$$\langle c^{in}(t)c^{in*}(t')\rangle = G\omega_0\delta(t-t'). \tag{3}$$

In thermal equilibrium and for the case of high temperature $k_BT \gg \hbar\omega_0$, where k_B is Boltzmann's constant, one has

$$G = \frac{2\gamma}{\omega_0}\frac{k_BT}{\hbar\omega_0}. \tag{4}$$

In terms of the dimensionless time $\tau=\omega_0 t$, Eq. (1) reads

$$\frac{dB}{d\tau} = \frac{i(\omega_p-\omega_0)-\gamma}{\omega_0}(B-B_\infty) + \frac{c^{in}}{\omega_0}, \tag{5}$$

where

$$B_\infty = \frac{i\sqrt{2\gamma_1}b^{in}}{i(\omega_p-\omega_0)-\gamma}. \tag{6}$$

Small noise gives rise to fluctuations around the steady-state solution B_∞. A straightforward calculation yields

$$\langle |B-B_\infty|^2\rangle = \frac{G\omega_0}{2\gamma}. \tag{7}$$

The output signal a^{out} reflected off the resonator can be written as $a^{out}=b^{out}e^{-i\omega_p t}$. The input-output relation relating the output signal to the input signal is given by[43]

$$\frac{b^{out}}{\sqrt{\omega_0}} = \frac{b^{in}}{\sqrt{\omega_0}} - i\sqrt{\frac{2\gamma_1}{\omega_0}}B, \tag{8}$$

whereas the total power dissipated in the resonator Q_t can be expressed as[3]

$$Q_t = \hbar\omega_0 2\gamma_2 E, \tag{9}$$

where $E=|B|^2$.

Furthermore, consider the case where the nonlinearity is originated by a local hot spot in the stripline resonator. If the hot spot is assumed to be sufficiently small, its temperature T can be considered to be homogeneous. The temperature of the other parts of the resonator is assumed to be equal to that of the coolant, T_0. The power Q heating up the hot spot is given by $Q=\alpha Q_t$ where $0\leqslant\alpha\leqslant 1$.

The heat balance equation reads

$$C\frac{dT}{dt} = Q - W, \tag{10}$$

where C is the thermal heat capacity, $W=H(T-T_0)$ is the heat power transferred to the coolant, and H is the heat transfer coefficient. Defining the dimensionless temperature[44]

$$\Theta = \frac{T-T_0}{T_c-T_0}, \tag{11}$$

where T_c is the critical temperature, one has

$$\frac{d\Theta}{d\tau} = -g(\Theta-\Theta_\infty), \tag{12}$$

where

$$\Theta_\infty = \frac{2\alpha\gamma_2\rho E}{\omega_0 g}, \tag{13}$$

$$\rho = \frac{\hbar\omega_0}{C(T_c-T_0)}, \tag{14}$$

$$g = \frac{H}{C\omega_0}. \tag{15}$$

While in Duffing oscillator equation discussed in Ref. 3 the nonlinearity can be described in terms of a gradually varying resonance frequency which depends on the amplitude of the oscillations inside the cavity, in the current case, the resonance frequency ω_0, the damping rates γ_1 and γ_2, and the α factor are considered to have a step function dependence on T, the temperature of the WL's:

$$\omega_0 = \begin{cases} \omega_{0s} & \Theta < 1, \\ \omega_{0n} & \Theta > 1, \end{cases} \tag{16}$$

$$\gamma_1 = \begin{cases} \gamma_{1s} & \Theta < 1, \\ \gamma_{1n} & \Theta > 1, \end{cases} \tag{17}$$

$$\gamma_2 = \begin{cases} \gamma_{2s} & \Theta < 1, \\ \gamma_{2n} & \Theta > 1, \end{cases} \tag{18}$$

$$\alpha = \begin{cases} \alpha_s & \Theta < 1, \\ \alpha_n & \Theta > 1. \end{cases} \tag{19}$$

In general, while disregarding noise, the coupled differential equations (5) and (12) may have up to two different steady-state solutions. A superconducting steady state of the WL exists when $\Theta_\infty<1$ or, alternatively, when $E<E_s$, where $E_s=gC(T_c-T_0)/2\alpha_s\gamma_{2s}\hbar$. Similarly, a normal steady state of the WL's exists when $\Theta_\infty>1$ or, alternatively, when $E>E_n$, where $E_n=gC(T_c-T_0)/2\alpha_n\gamma_{2n}\hbar$.

In addition, the reflection coefficient S_{11} in steady state is in general given by[3]

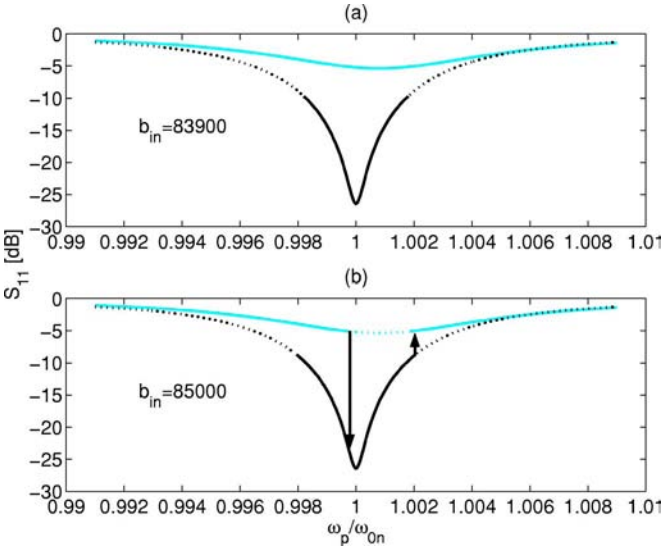

FIG. 12. (Color online). Simulated resonance response obtained by the hot-spot mechanism model. The different plots simulate the nonlinear behavior shown in Fig. 2. Panels (a) and (b) correspond to an increasing drive amplitude b^{in}. The solid lines represent valid steady-state solutions whereas the dotted lines represent invalid solutions. The black lines represent the normal WL solutions, whereas the cyan (gray) lines represent the superconducting WL solutions. The black arrows show the direction of the jumps in the different cases. The parameters that were used in the simulation are $\omega_{0s}/\omega_{0n}=1.0008$, $\gamma_{1n}/\omega_{0n}=2.5\times10^{-3}$, $\gamma_{1s}/\omega_{0n}=1.5\times10^{-3}$, $\gamma_{2n}/\omega_{0n}=2.75\times10^{-3}$, $\gamma_{2s}/\omega_{0n}=5\times10^{-3}$, $\alpha_n=0.8$, $\alpha_s=1$, $g=0.5$, and $\rho=10^{-10}$.

$$S_{11}=\frac{b^{out}}{b^{in}}=\frac{\gamma_2-\gamma_1-i(\omega_p-\omega_0)}{\gamma_2+\gamma_1-i(\omega_p-\omega_0)}. \tag{20}$$

B. Simulation results

Simulating the resonator system using this local heating WL model yields results which qualitatively agree with most of the nonlinear effects previously presented. In Sec. VI B 1 we simulate the main effects of Secs. III A–III D, whereas in Sec. VI B 2 we simulate and provide a possible explanation to the nonlinear features of Sec. III E.

1. Abrupt jumps and hysteretic behavior

In Fig. 12 we show a resonance response simulation result based on the hot-spot model, which simulates the abrupt jump exhibited in Fig. 2. The solid and dotted lines represent valid steady-state solutions of the system and invalid steady-state solutions, respectively, while the cyan (gray) and black colors represent superconducting WL solutions and normal WL solutions, respectively. In plot (a) the superconducting WL solution is valid in the normalized frequency span, and therefore the system follows this line shape without jumps. As we increase the amplitude drive b_{in} we obtain a result shown in plot (b). As the frequency is swept, jumps in the resonance response are expected to take place as the solution followed by the system (according to the initial conditions) becomes invalid. Thus in the forward sweep direction (as the frequency sweep of Fig. 2), we get two jumps indicated by black arrows on the figure. Similar to Fig. 2, the magnitudes of the jumps are unequal (the left jump is larger). This difference in the magnitude of the jumps is generally dependent on the relative position between the two resonance frequencies [Eq. (16)]. In the experiment, on the other hand, due to the metastability of the system in the hysteretic regime, it depends also on the frequency sweep rate. The simulation parameters used in the different phases are indicated in the figure captions.

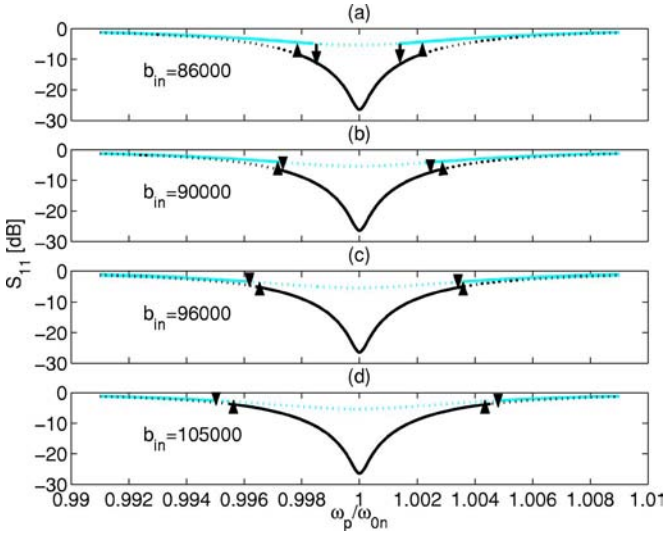

FIG. 13. (Color online). Simulated resonance response obtained by the hot spot mechanism model. Panels (a), (b), (c), and (d) correspond to an increasing drive amplitude b^{in}. The different plots simulate the nonlinear behavior shown in Fig. 3. The lines and symbols are the same as in Fig. 12. The parameters that were used in the simulation are $\omega_{0s}/\omega_{0n}=0.99989$, $\gamma_{1n}/\omega_{0n}=2.5\times10^{-3}$, $\gamma_{1s}/\omega_{0n}=1.5\times10^{-3}$, $\gamma_{2n}/\omega_{0n}=2.75\times10^{-3}$, $\gamma_{2s}/\omega_{0n}=5\times10^{-3}$, $\alpha_n=0.8$, $\alpha_s=1$, $g=0.5$, and $\rho=10^{-10}$.

The behavior of the frequency hysteresis loops exhibited in Fig. 3 is simulated in Fig. 13. The different plots exhibited in Fig. 13 correspond to the different phases shown in Fig. 3. In plot (a) the jumps in the forward direction (indicated by the arrows in that direction) occur at higher frequencies than the jumps in the backward direction, whereas in plot (b) corresponding to a higher drive amplitude b_{in} we show a case in which the left-side hysteresis loop vanishes as the two opposed jump frequencies coincide. If we increase b_{in} further, then at some drive amplitude as shown in plot (c), we get a similar case of vanishing hysteresis loop at the right side of the resonance response, whereas at the left side we get a frequency region where both the superconducting and normal WL solutions are invalid. In this instable region, transitions between the invalid solutions are expected, depending on the number of the sampling points, the sweep time, and the internal noise. However, due to this instability, the system is highly expected to jump "early" in each frequency direction, as it enters this region (at lower frequencies in the forward direction and at higher frequencies in the backward direction), thus leading to the observed change in the direction of the hysteresis loop. By increasing b_{in} further, one obtains a case in which both hysteresis loops are circulating

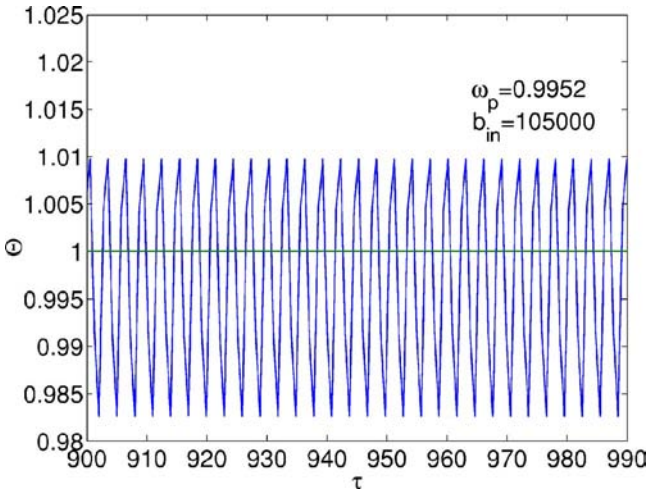

FIG. 14. (Color online). The dynamical solution of the coupled equations (5) and (12) at a normalized frequency of $\omega_p = 0.9952$. The simulation parameters used are the same as those of Fig. 13(d).

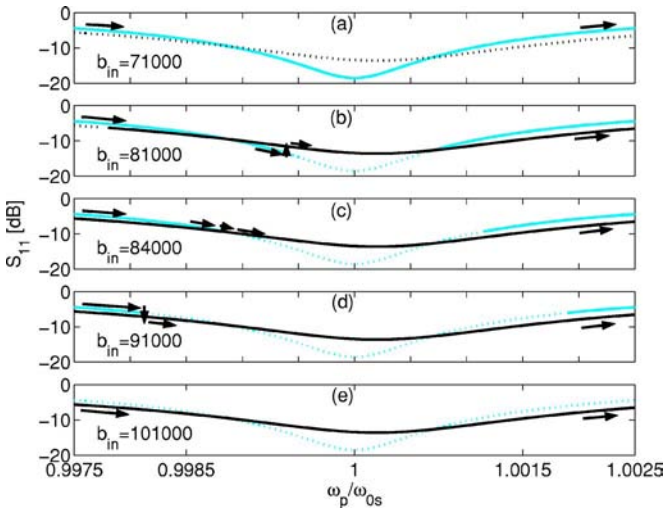

FIG. 15. (Color online). Simulated resonance response obtained by the hot-spot mechanism model. The different plots simulate the nonlinear behavior shown in Fig. 6. Panels (a), (b), (c), (d), and (e) correspond to an increasing drive amplitude b^{in}. The lines and symbols are the same as in Fig. 12. The simulation parameters used are $\omega_{0n}/\omega_{0s} = 1.0002$, $\gamma_{1n}/\omega_{0s} = 0.0029$, $\gamma_{1s}/\omega_{0s} = 0.0019$, $\gamma_{2n}/\omega_{0s} = 0.0019$, $\gamma_{2s}/\omega_{0s} = 0.0015$, $\alpha_n = 1$, $\alpha_s = 0.8$, $g = 0.5$, and $\rho = 10^{-10}$.

in the opposite direction compared to plot (a).

Furthermore, the intermediate jump indicating instability, which appears at the left jump region of the last resonance curve in Fig. 3 (corresponding to −18.6 dBm), can be explained by this model as well. By solving the coupled equations (5) and (12) in the time domain for a single normalized frequency $\omega_p = 0.9952$ (arbitrarily chosen in the left-side hysteresis region) and using the simulation parameters of Fig. 13(d), one obtains the oscillation pattern of the dimensionless temperature Θ as a function of the dimensionless time τ, which is shown in Fig. 14. The Θ oscillations indicating instability are between the superconducting and normal values, corresponding to $\Theta < 1$ and $\Theta > 1$, respectively.

As to the multiple-jump feature exhibited in Fig. 5, a straightforward generalization of the model may be needed in order to account for this effect. Such a generalization would include several WL's having a variation in their sizes and their critical current along the stripline, thus causing them to switch to the normal state at different drive currents (corresponding to different frequencies) and as a result induce more than two jumps in the resonance line shape.

2. Magnetic field dependence

In this subsection we show how the model of local heating of WL's can also account for the nonlinear dynamics of the resonance line shape observed under an applied magnetic field.

To this end, we show in Fig. 15 a simulation result based on the WL local heating model, which regenerates qualitatively the nonlinear behavior of the resonance line shape of B2 under a constant magnetic field (presented in Fig. 6). At low drive amplitude b_{in}, only the superconducting WL steady-state solution exists, and thus no jump occurs as one sweeps the frequency [plot (a)]. Increasing the drive amplitude b_{in} [plot (b)] causes the superconducting WL solution to become invalid in the center frequency region; thus, the resonance response jumps upward (as the system reaches the invalid region) and stabilizes on the normal WL steady-state solution, as indicated by arrows in the plot. By increasing the drive amplitude further [plot (c)] one gets an intersection point where a smooth transition (without a jump) is expected to occur between the valid superconducting WL solution and the valid normal one, whereas in plot (d), where we have increased b_{in} further, a downward jump in the resonance response occurs as the valid normal WL solution lies below the invalid superconducting WL solution. Finally in plot (e), corresponding to a much higher drive, only the normal WL steady-state solution exists (within the frequency span), and therefore there are no jumps in the resultant curve.

Another measurement which can be explained using the WL model is the measurement shown in Fig. 7, where the left-side jump vanishes as the magnetic field increases above some low-magnetic-field threshold. This result can be explained in the following manner. Increasing the applied dc magnetic field would increase the screening supercurrent flowing in the film and the local heating of the WL. As the local heating exceeds some threshold, the superconducting WL solution would become invalid (within the same frequency span), and consequently, the system would only follow the normal WL solution without apparent jumps.

VII. SUMMARY

In attempt to investigate and manifest nonlinear effects in superconducting microwave resonators, several superconducting NbN resonators employing different layouts, but similar sputtering conditions, have been designed and fabricated. The resonance line shapes of these NbN resonators having a very low onset of nonlinearity, several orders of magnitude lower than other reported nonlinearities,[13,45,46] exhibit some extraordinary nonlinear dynamics. Among the nonlinearities observed while applying different measure-

ment configurations are abrupt metastable jumps in the resonance line shape, hysteresis loops changing direction, multiple jumps, vanishing jumps, and jumps changing direction. These effects are hypothesized to originate from weak links located at the boundaries of the columnar structure of the NbN films. This hypothesis is fully consistent with SEM micrographs of these films and generally agrees with the extrinsiclike behavior of these resonators. To account for the various nonlinearities observed, a theoretical model assuming local heating of weak links is suggested. Furthermore, simulation results employing this model are shown to be in a very good qualitative agreement with measurements.

Such strong sensitive nonlinear effects reported herein may be utilized in the future in a variety of applications, ranging from qubit coupling in quantum computation to signal amplification[47] and to the demonstration of some important quantum effects in the microwave regime.[3,48]

ACKNOWLEDGMENTS

E.B. would especially like to thank Michael L. Roukes for supporting the early stage of this research and for many helpful conversations and invaluable suggestions. Very helpful conversations with Oded Gottlieb, Gad Koren, Emil Polturak, and Bernard Yurke are also gratefully acknowledged. This work was supported by the German Israel Foundation under Grant No. 1-2038.1114.07, the Israel Science Foundation under Grant No. 1380021, the Deborah Foundation, and the Poznanski Foundation.

*Electronic address: baleegh@tx.technion.ac.il

[1] R. Movshovich, B. Yurke, P. G. Kaminsky, A. D. Smith, A. H. Silver, R. W. Simon, and M. V. Schneider, Phys. Rev. Lett. **65**, 1419 (1990).

[2] B. Yurke, P. G. Kaminsky, R. E. Miller, E. A. Whittaker, A. D. Smith, A. H. Silver, and R. W. Simon, IEEE Trans. Magn. **25**, 1371 (1989).

[3] B. Yurke and E. Buks, quant-ph/0505018 (unpublished).

[4] E. Buks and B. Yurke, Phys. Rev. A **73**, 023815 (2006).

[5] I. Siddiqi, R. Vijay, F. Pierre, C. M. Wilson, M. Metcalfe, C. Rigetti, L. Frunzio, and M. H. Devoret, Phys. Rev. Lett. **93**, 207002 (2004).

[6] I. Siddiqi, R. Vijay, F. Pierre, C. M. Wilson, L. Frunzio, M. Metcalfe, C. Rigetti, R. J. Schoelkopf, M. H. Devoret, D. Vion, and D. Esteve, Phys. Rev. Lett. **94**, 027005 (2005).

[7] P. J. Burke, R. J. Schoelkopf, D. E. Prober, A. Skalare, B. S. Karasik, M. C. Gaidis, W. R. McGrath, B. Bumble, and H. G. LeDuc, Appl. Phys. Lett. **85**, 1644 (1999).

[8] R. Sobolewski, A. Verevkin, G. N. Gol'tsman, A. Lipatov, and K. Wilsher, IEEE Trans. Appl. Supercond. **13**, 1151 (2003).

[9] I. Chiorescu, Y. Nakamura, C. J. P. M. Harmans, and J. E. Mooij, Science **299**, 1869 (2003).

[10] T. Dahm and D. J. Scalapino, J. Appl. Phys. **81**, 2002 (1997).

[11] Z. Ma, E. de Obaldia, G. Hampel, P. Polakos, P. Mankiewich, B. Batlogg, W. Prusseit, H. Kinder, A. Anderson, D. E. Oates, R. Ono, and J. Beall, IEEE Trans. Appl. Supercond. **7**, 1911 (1997).

[12] R. B. Hammond, E. R. Soares, B. A. Willemsen, T. Dahm, D. J. Scalapino, and J. R. Schrieffer, J. Appl. Phys. **84**, 5662 (1998).

[13] C. C. Chin, D. E. Oates, G. Dresselhaus, and M. S. Dresselhaus, Phys. Rev. B **45**, 4788 (1992).

[14] L. F. Cohen, A. L. Cowie, A. Purnell, N. A. Lindop, S. Thiess, and J. C. Gallop, Supercond. Sci. Technol. **15**, 559 (2002).

[15] A. L. Karuzskii, A. E. Krapivka, A. N. Lykov, A. V. Perestoronin, and A. I. Golovashkin, Physica B **329-333**, 1514 (2003).

[16] Z. Ma, E. D. Obaldia, G. Hampel, P. Polakos, P. Mankiewich, B. Batlogg, W. Prusseit, H. Kinder, A. Anderson, D. E. Oates, R. Ono, and J. Beall, IEEE Trans. Appl. Supercond. **7**, 1911 (1997).

[17] J. Wosik, L.-M. Xie, J. H. Miller, Jr., S. A. Long, and K. Nesteruk, IEEE Trans. Appl. Supercond. **7**, 1470 (1997).

[18] B. A. Willemsen, J. S. Derov, J. H. Silva, and S. Sridhar, IEEE Trans. Appl. Supercond. **5**, 1753 (1995).

[19] A. M. Portis, H. Chaloupka, M. Jeck, and A. Pischke, Supercond. Sci. Technol. **4**, 436 (1991).

[20] S. J. Hedges, M. J. Adams, and B. F. Nicholson, Electron. Lett. **26**, 977 (1990).

[21] J. Wosik, L.-M. Xie, R. Grabovickic, T. Hogan, and S. A. Long, IEEE Trans. Appl. Supercond. **9**, 2456 (1999).

[22] D. E. Oates, M. A. Hein, P. J. Hirst, R. G. Humphreys, G. Koren, and E. Polturak, Physica C **372-376**, 462 (2002).

[23] M. A. Golosovsky, H. J. Snortland, and M. R. Beasley, Phys. Rev. B **51**, 6462 (1995).

[24] S. K. Yip and J. A. Sauls, Phys. Rev. Lett. **69**, 2264 (1992).

[25] D. E. Oates, H. Xin, G. Dresselhaus, and M. S. Dresselhaus, IEEE Trans. Appl. Supercond. **11**, 2804 (2001).

[26] B. B. Jin and R. X. Wu, J. Supercond. **11**, 291 (1998).

[27] A. V. Velichko, D. W. Huish, M. J. Lancaster, and A. Porch, IEEE Trans. Appl. Supercond. **13**, 3598 (2003).

[28] J. Halbritter, J. Appl. Phys. **68**, 6315 (1990).

[29] B. Abdo, E. Segev, Oleg Shtempluck, and E. Buks, IEEE Trans. Appl. Supercond. (to be published), cond-mat/0501114.

[30] J. H. Oates, R. T. Shin, D. E. Oates, M. J. Tsuk, and P. P. Nguyen, IEEE Trans. Appl. Supercond. **3**, 17 (1993).

[31] H. Xin, D. E. Oates, G. Dresselhaus, and M. S. Dresselhaus, J. Supercond. **14**, 637 (2001).

[32] R. Whiteman, J. Diggins, V. Schöllmann, T. D. Clark, R. J. Prance, H. Prance, and J. F. Ralph, Phys. Lett. A **234**, 205 (1997).

[33] H. Prance, T. D. Clark, R. Whiteman, R. J. Prance, M. Everitt, P. Stiffel, and J. F. Ralph, Phys. Rev. E **64**, 016208 (2001).

[34] R. J. Prance, R. Whiteman, T. D. Clark, H. Prance, V. Schöllmann, J. F. Ralph, S. Al-Khawaja, and M. Everitt, Phys. Rev. Lett. **82**, 5401 (1999).

[35] J. S. Aldridge and A. N. Cleland, Phys. Rev. Lett. **94**, 156403 (2005).

[36] H. A. Kramers, Physica (Amsterdam) **7**, 284 (1940).

[37] D. M. Sheen, S. M. Ali, D. E. Oates, R. S. Withers, and J. A. Kong, IEEE Trans. Appl. Supercond. **1**, 108 (1991).

[38] S. Isagawa, J. Appl. Phys. **52**, 921 (1980).

[39] Y. M. Shy, L. E. Toth, and R. Somasundaram, J. Appl. Phys. **44**, 5539 (1973).
[40] M. W. Johnson, A. M. Herr, and A. M. Kadin, J. Appl. Phys. **79**, 7069 (1996).
[41] A. M. Kadin and M. W. Johnson, Appl. Phys. Lett. **69**, 3938 (1996).
[42] K. Weiser, U. Strom, S. A. Wolf, and D. U. Gubser, J. Appl. Phys. **52**, 4888 (1981).
[43] C. W. Gardiner and M. J. Collett, Phys. Rev. A **31**, 3761 (1985).
[44] A. VI. Gurevich and R. G. Mints, Rev. Mod. Phys. **59**, 941 (1987).
[45] P. P. Nguyen, D. E. Oates, G. Dresselhaus, M. S. Dresselhaus, and A. C. Anderson, Phys. Rev. B **51**, 6686 (1995).
[46] A. Andreone, A. Cassinese, A. Di Chiara, M. Lavarone, F. Palomba, A. Ruosi, and R. Vaglio, J. Appl. Phys. **82**, 1736 (1997).
[47] B. Abdo, E. Segev, O. Shtempluck, and E. Buks, Appl. Phys. Lett. **88**, 022508 (2006).
[48] B. Abdo, E. Segev, O. Shtempluck, and E. Buks, cond-mat/0501236 (unpublished).

4.3 Intermodulation gain in nonlinear NbN superconducting microwave resonators

Intermodulation gain in nonlinear NbN superconducting microwave resonators

Baleegh Abdo,[a] Eran Segev, Oleg Shtempluck, and Eyal Buks
Microelectronics Research Center, Department of Electrical Engineering, Technion, Haifa 32000, Israel

(Received 3 August 2005; accepted 21 November 2005; published online 12 January 2006)

We report the measurement of intermodulation gain greater than unity in NbN superconducting stripline resonators. In the intermodulation measurements we inject two unequal tones into the oscillator—the pump and signal—both lying within the resonance band. At the onset of instability of the reflected pump we obtain a simultaneous gain of both the idler and the reflected signal. The measured gain in both cases can be as high as 15 dB. © *2006 American Institute of Physics*.
[DOI: 10.1063/1.2164925]

In previous publications,[1,2] we have presented and discussed extensively the unusual nonlinear effects observed in our nonlinear NbN superconducting resonators, which include, among others, abrupt jumps in the resonance line shape, hysteresis loops changing direction, magnetic field sensitivity, resonance frequency shift, and nonlinear coupling.[3] These nonlinear effects, as it was shown in Ref. 2, are likely to originate from weak links forming at the boundaries of the NbN columnar structure. In the present work, we examine these nonlinear resonators from another aspect by applying intermodulation measurements, which are considered one of the effective tools for detecting and studying nonlinearities in microwave superconducting devices.[4–12]

The results of the intermodulation measurements of these resonators not only provide an important insight as to the possible nonlinear mechanisms responsible for the observed dynamics,[5,11] they exhibit interesting unique features as well. We show that driving the nonlinear resonator to its onset of instability while injecting two closely spaced unequal tones lying within the resonance band into the resonator results in high amplification of both the low-amplitude injected signal and the idler (the tone generated via the nonlinear frequency mixing of the resonator). In Ref. 13, wherein the case of an intermodulation amplifier based on nonlinear Duffing oscillator has been analyzed, it was shown that intermodulation divergence is expected as the oscillator is driven near the critical slowing down point, where the slope of the device response with respect to frequency becomes infinite. The fact that our NbN resonators do not exhibit Duffing oscillator nonlinearity of the kind employed in the analysis of Ref. 13, but yet show high intermodulation gains in the vicinity of the bifurcation points, suggests strongly that the intermodulation gain effect predicted in Ref. 13 is not unique for the Duffing oscillator, and can be demonstrated using other kinds of nonlinear bifurcations. Moreover, in recent publications by Siddiqi *et al.*,[14,15] where dynamical bifurcations between two driven oscillation states of a Josephson junction have been directly observed, it has been suggested to employ this Josephson junction nonlinear mechanism for the purpose of amplification and quantum measurements.[15]

The intermodulation measurements presented in this letter were performed on a nonlinear NbN superconducting stripline microwave resonator. The layout of the resonator employed having $T_c = 10.7$ K is depicted in Fig. 1(a). The NbN resonator film was dc-magnetron sputtered on 34 mm × 30 mm × 1 mm sapphire substrate near room temperature. The thickness of the resonator is 2200 Å. The film was patterned using standard photolithography process and etched by Ar ion milling. The coupling gap between the resonator and its feedline was set to 0.4 mm. The fabrication process parameters as well as other design considerations can be found elsewhere.[1]

The basic intermodulation experimental setup that has been used, is schematically depicted in Fig. 2. The input field of the resonator is composed of two sinusoidal fields generated by external microwave synthesizers and combined using a power combiner. The isolators in the signal paths were added to minimize crosstalk noise between the signals and to suppress reflections. The signals used have unequal amplitudes: one, which we will refer to as the pump, is an intense sinusoidal field with frequency f_p, whereas the other, which we will refer to as the signal, is a small amplitude sinusoidal field with frequency $f_p + f$, where f represents the frequency offset between the two signals. Due to the nonlinearity of the resonator, frequency mixing between the pump and the signal yields an output idler field at frequency $f_p - f$. Thus, the output field from the resonator, which is redirected by a circulator and measured by a spectrum analyzer, consists mainly of three spectral components: the reflected pump, the reflected signal, and the generated idler. The intermodulation amplification in the signal and idler is obtained, as is shown in this letter, by driving the resonator to its onset of instability, via tuning the pump power.

In the intermodulation measurements, we limit the signal power to be several orders of magnitude smaller than the pump power, as was assumed in Ref. 13, and require that all of the tones (pump, signal, idler) lie within the resonance band of the resonator during the intermodulation operation.

In Fig. 1 we present an intermodulation measurement applied to the first resonance mode of the resonator (~2.58 GHz), at 4.2 K, where we measured the idler and the reflected tones (pump and signal) as a function of both the transmitted pump power and frequency. The experimental results presented here were obtained while decreasing the pump power gradually at each given frequency. The pump power range was set to include the onset of nonlinear bifurcations of the resonator first mode, which occurs at relatively

[a]Electronic mail: baleegh@tx.technion.ac.il

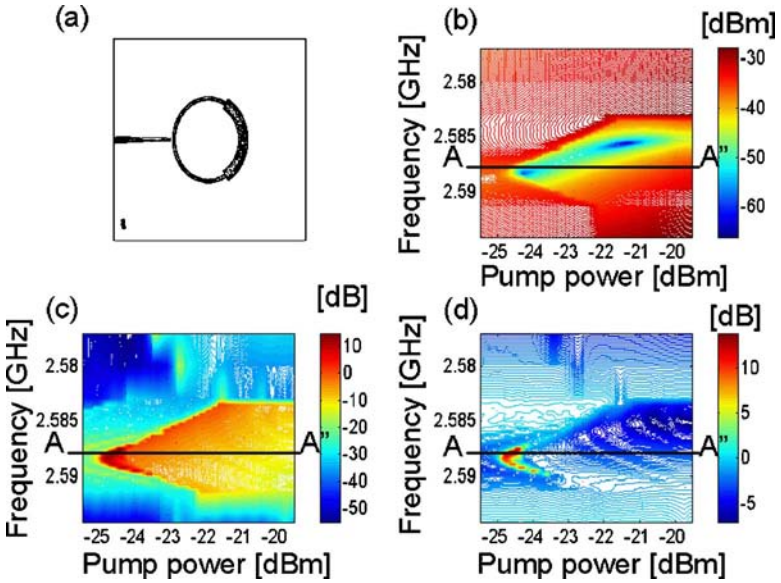

FIG. 1. (Color online) Intermodulation measurement results employing the first mode of the resonator. Plot (a) depicts the layout of the resonator. Plots (b), (c), and (d) exhibit contours of the reflected pump power, idler gain, and signal gain, respectively, as a function of transmitted pump power and pump frequency. The results were obtained while gradually decreasing the pump power. The frequency offset between the pump and signal was set to 2 kHz, whereas the signal power was set to −60 dBm. The cross sections A-A″ are shown in Fig. 3.

low input powers of the order of −25 dBm, whereas the signal was set to a constant power level of −60 dBm. The pump-signal frequency offset f was set to 2 kHz, very much narrower than the resonance band (thus ensuring that all three signals lie within the resonance line shape during the measurement process).

The reason for varying the pump power rather than its frequency to the onset of bifurcation is mostly because the bifurcations along the frequency axis are abrupt,[1] in contrast to the bifurcations along the power axis, which are more gradual. In Fig. 1, plots (b), (c), and (d) show contours of the reflected pump power, idler gain, and signal gain, respectively, as a function of pump power and pump frequency. Large amplifications of the idler and the signal are measured simultaneously as the reflected pump power bifurcates at a given pump frequency, as its power is decreased below some power threshold. These amplification peaks can be better seen in Fig. 3, where we show the idler gain and the signal gain at 2.5879 GHz (A-A″ cross section), plotted on the same axis with the reflected pump power for comparison.

The amplification gain [dB], which is defined as the difference between the idler or signal power at the resonator output [dBm] and the signal power [dBm] at the resonator input (losses in cables and passive devices are calibrated), reaches 14.99 dB at its peak in the case of the idler gain, and 13.91 dB in the case of the signal gain.

In Fig. 4 we show a power-frequency hysteresis of the reflected pump signal, which implies that the nonlinear resonance shape of the resonator, as a two-dimensional function of input power and frequency, is multivalued; therefore, care must be taken in choosing the path in reaching each point in the power-frequency plane. Furthermore, in the forward sweep of the pump, no positive gain has been detected in the idler or signal. This may be partly due to the less steep slopes associated with bifurcations in the forward direction, as seen in Fig. 4(b).

Based on these high gains demonstrated experimentally at $T=4.2$ K (and $f\sim 2.5$ GHz), it is interesting to consider the feasibility of demonstrating some important quantum phenomena using these nonlinear effects in the quantum regime where $\hbar\omega \gg k_B T$ ($T \ll 100$ mK). As in Ref. 13, we consider the mode of operation wherein a homodyne detection scheme with a local oscillator having the frequency of the pump is employed to measure the resonator output. The noise floor of the device is characterized by the power spectrum P of the homodyne detector output, where the only externally applied input is the pump. In the nonlinear regime of operation noise squeezing occurs; namely, P becomes dependent periodically on the phase of the local oscillator ϕ_{LO} relative to the phase of the pump. In particular, for an intermodulation amplifier having a gain larger than unity, as the one described in the present work, the maximum value of

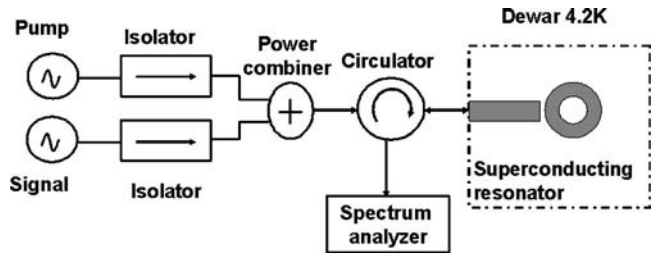

FIG. 2. A schematic drawing of the intermodulation setup used.

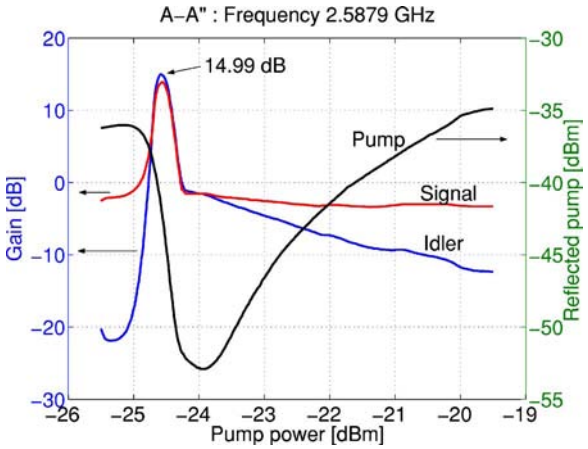

FIG. 3. (Color online) The idler and signal gains at the A-A″ cross section of Fig. 1 are shown as a function pump power. The reflected pump power at the same cross section A-A″ is also drawn on the same axis for comparison. A simultaneous amplification in the idler and signal is measured at the onset of instability of the reflected pump power.

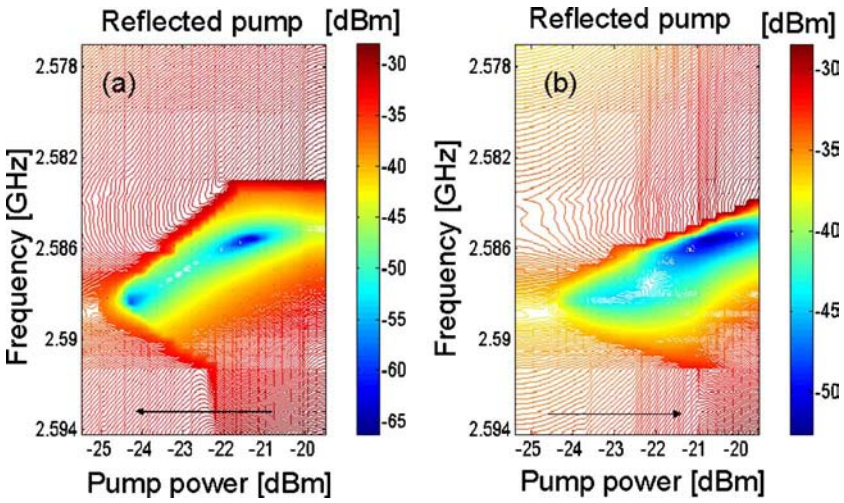

FIG. 4. (Color online) Reflected pump hysteresis during intermodulation operation. Left contour plot obtained while decreasing pump power, right contour plot while increasing pump power.

$P(\phi_{\mathrm{LO}})$ may become larger than the value corresponding to equilibrium noise. In the quantum limit, where $\hbar\omega \gg k_{\mathrm{B}}T$, this effect is somewhat similar to the well known dynamical Casimir effect,[16] where a parametric excitation is employed to amplify vacuum fluctuations and to generate photons.

In conclusion, we have measured intermodulation gain in several nonlinear NbN superconducting stripline resonators, at relatively low temperatures ~4.2 K. An intermodulation gain as high as ~15 dB was achieved. Moreover, we showed that the reflected pump power, as well as the signal gain and the idler gain, demonstrate strong hysteretic behavior in the frequency-pump power plane. The intermodulation gain results were found to be both reproducible and controllable, which is a preliminary condition for any practical application. Whereas the underlying physics remains an outstanding challenge for future research, these nonlinear resonators operated as intermodulation amplifiers may be potentially employed, in the future, in generating low-noise microwave signals, signal switching, and even in producing quantum squeezed states[13] and amplifying quantum zero-point fluctuations.

One of the authors (E.B.) would especially like to thank Michael L. Roukes for supporting the early stage of this research and for many helpful conversations and invaluable suggestions. Very helpful conversations with Bernard Yurke are also gratefully acknowledged. This work was supported by the German Israel Foundation under grant 1-2038.1114.07, the Israel Science Foundation under grant 1380021, the Deborah Foundation, and Poznanski Foundation.

[1] B. Abdo, E. Segev, Oleg Shtempluck, and E. Buks, cond-mat/0501114.
[2] B. Abdo, E. Segev, O. Shtempluck, and E. Buks, cond-mat/0504582.
[3] B. Abdo, E. Segev, O. Shtempluck, and E. Buks, cond-mat/0501236.
[4] C. C. Chen, D. E. Oates, G. Dresselhaus, and M. S. Dresselhaus, Phys. Rev. B **45**, 4788 (1992).
[5] T. Dahm and D. J. Scalapino, J. Appl. Phys. **81**, 2002 (1997).
[6] D. E. Oates, S.-H. Park, and G. Koren, Phys. Rev. Lett. **93**, 197001 (2004).
[7] B. A. Willemsen, K. E. Kihlstrom, and T. Dahm, Appl. Phys. Lett. **74**, 753 (1999).
[8] R. B. Hammond, E. R. Soares, B. A. Willemsen, T. Dahm, D. J. Scalapino, and J. R. Schrieffer, J. Appl. Phys. **84**, 5662 (1998).
[9] S. Cho and C. Lee, IEEE Trans. Appl. Supercond. **9**, 3998 (1999).
[10] H. Hoshizaki, N. Sakakibara, and Y. Ueno, J. Appl. Phys. **86**, 5788 (1999).
[11] D. E. Oates, S.-H. Park, M. A. Hein, P. J. Hirst, and R. G. Humphreys, IEEE Trans. Appl. Supercond. **13**, 311 (2003).
[12] R. Monaco, A. Andreone, and F. Palomba, J. Appl. Phys. **88**, 2898 (2000).
[13] B. Yurke and E. Buks, quant-ph/0505018.
[14] I. Siddiqi, R. Vijay, F. Pierre, C. M. Wilson, L. Frunzio, M. Metcalfe, C. Riggetti, R. J. Schoelkopf, M. H. Devoret, D. Vion, and D. Esteve, Phys. Rev. Lett. **94**, 027005 (2005).
[15] I. Siddiqi, R. Vijay, F. Pierre, C. M. Wilson, M. Metcalfe, C. Riggetti, L. Frunzio, and M. H. Devoret, Phys. Rev. Lett. **93**, 207002 (2004).
[16] V. V. Dodonov, Adv. Chem. Phys. **119**, 309 (2001).

4.4 Signal amplification in NbN superconducting resonators via stochastic resonance

Available online at www.sciencedirect.com
ScienceDirect
Physics Letters A 370 (2007) 449–453
PHYSICS LETTERS A
www.elsevier.com/locate/pla

Signal amplification in NbN superconducting resonators via stochastic resonance

Baleegh Abdo *, Eran Segev, Oleg Shtempluck, Eyal Buks

Microelectronics Research Center, Department of Electrical Engineering, Technion, Haifa 32000, Israel

Received 1 April 2007; received in revised form 27 May 2007; accepted 31 May 2007

Available online 6 June 2007

Communicated by A.R. Bishop

Abstract

We exploit nonlinearity in NbN superconducting stripline resonators, which originates from local thermal instability, for studying stochastic resonance. As the resonators are driven into instability, small amplitude modulation (AM) signals are amplified with the aid of injected white noise. Simulation results based on the equations of motion for the system yield a good agreement with the experimental data both in the frequency and time domains.

Keywords: Nonlinear resonators; Superconducting devices; Stochastic processes

The notion that certain amount of white noise can appreciably amplify small periodic modulating signals acting on bistable systems, generally known as *stochastic resonance* (SR), has been over the last two decades of a great interest [1–4]. It has been applied for instance to account for the periodicity of ice ages occurring on earth [5], as well as to explain some important neurophysiological processes [6]. Furthermore, it has been used to amplify small signals in various nonlinear systems, e.g. the intensity of one laser mode in a bistable ring laser [7], the magnetic flux in a superconducting quantum interference device [8], and even more recently, a small periodic drive of a nanomechanical oscillator [9,10]. The performance of an amplifier based on SR strongly depends in general on the underlying mechanism responsible for nonlinear instability. Here we employ a novel thermal instability mechanism, which has been recently discovered in superconducting NbN microwave resonators [11], to study SR. Contrary to other systems, which were employed before for studying SR, the dynamics in the present case is piecewise linear [12]. Moreover, the correlation time of the dynamical variable, which triggers transitions between metastable states, namely the temperature, is finite in our system [13]. These unique properties give rise to extreme nonlinearity, which occurs at a relatively low power level [14]. As we demonstrate in this Letter, both experimentally and theoretically, this mechanism is highly suitable for achieving high gain amplification at a relatively low power level.

In the experiment the resonators are driven into instability using a microwave pump having a frequency, which lies within the resonance band of the system. The amplified signal in this scheme is a small amplitude modulation (AM) drive modulating the pump signal with a relatively low frequency.

The superconducting resonator is fabricated in stripline geometry while using Sapphire as a dielectric material. The layout of the center conductor implemented is shown at the top-right corner of Fig. 2. Fabrication details as well as nonlinear characterization of such resonators can be found in Ref. [11].

In order to set a possible working point of the resonator at the metastable region, two preliminary hysteresis measurements were performed. In one measurement exhibited in Fig. 1(a), forward and backward frequency sweeps of the reflection parameter S_{11}, measured for the resonator fundamental mode at $f_0 \simeq 2.57\,\mathrm{GHz}$, reveal two hysteresis loops at both sides of the resonance line shape at which the resonator becomes bistable. In another measurement shown in Fig. 1(b) the frequency of the pump f_p was set to 2.565 GHz positioned at the left side of the

* Corresponding author.
E-mail address: baleegh@tx.technion.ac.il (B. Abdo).

0375-9601/$ – see front matter
doi:10.1016/j.physleta.2007.05.103

resonance, while the input power was swept in the forward and the backward directions. A hysteresis loop of the reflection parameter appears in this measurement as well, this time along the power axis. Thus, the working point was set to $f_p = 2.565\,\text{GHz}$, $P_0 = -21.5$ dBm, while the applied modulation drive is a sinusoidal AM signal with a modulation amplitude $A_{\text{mod}} = 0.27$.

A schematic diagram of the experimental setup employed in the measurement of SR is depicted in Fig. 2. A coherent signal $P_0 \cos(\omega_p t)$ with angular frequency $\omega_p = 2\pi f_p$ is AM modulated using a sinusoidal generator with an angular frequency Ω. The modulated signal is combined with a white noise and injected into the resonator. The white noise, which is generated using a noise source is amplified using an amplifying stage and tuned via an adjustable attenuator. Thus, the input signal power fed to the feedline of the resonator (after calibrating the path losses) reads

$$P_{\text{in}}(t) = P_0\big[1 + A_{\text{mod}} \sin(\Omega t + \varphi)\big]\cos(\omega_p t) + \xi(t), \tag{1}$$

where $\xi(t)$ denotes a zero-mean Gaussian white noise $\langle \xi(t) \rangle = 0$, with autocorrelation function $\langle \xi(t)\xi(t') \rangle = 2D\delta(t - t')$, where D is the noise intensity. Whereas, the reflected power off the resonator is mixed with a local oscillator with frequency f_p and measured simultaneously in the time and frequency domains using an oscilloscope and a spectrum analyzer respectively.

It is worthwhile to point out here that the SR phenomenon excited by means of AM modulation (Eq. (1)), can be considered as well as a high-frequency stochastic resonance of the kind defined by Dykman et al. [15] and demonstrated experimentally by Chan and Stambaugh [16] on nanomechanical oscillators, where the frequencies of the weak modulating drive $\omega_p \pm \Omega$ lie close to the frequency of the main periodic driving force ω_p.

Furthermore, for small amplitudes of the modulation signal $A_{\text{mod}} \ll 1$ and in steady state conditions, the spectral density of the reflected power at the output of the homodyne setup, can in general be written in the form [3,4]

$$S(\omega) = 2\pi P_0^r \delta(\omega) + \pi \sum_{n=1}^{\infty} A_n^r(D)\big[\delta(\omega - n\Omega) + \delta(\omega + n\Omega)\big] + S_N(\omega), \tag{2}$$

which is composed of a delta spike at dc ($\omega = 0$), delta spikes with amplitudes $A_n^r(D)$ centered at $\omega = \pm n\Omega$, $n = 1, 2, 3, \ldots$, and a background spectral density of the noise denoted by $S_N(\omega)$. Whereas P_0^r designates the dc component of the reflected power.

As it is known, one of the distinguished fingerprints of SR phenomenon is a peak observed in the signal to noise ratio (SNR) curve as a function of the input noise intensity D, corresponding to some nonzero intensity D_{SR}. This counterintuitive amplification in SNR curve is generally explained in terms of coherent interaction between the modulating signal and the stochastic noise entering the system.

In this framework the SNR for the nth harmonic can be defined as [1]

$$\text{SNR}_n \equiv 2\pi A_n^r(D)/S_N(n\Omega), \tag{3}$$

where SNR of the fundamental harmonic corresponds to $n = 1$.

In Fig. 3(a) and (b), two SNR data curves (blue) are drawn as a function of the noise intensity, corresponding to the odd harmonics $n = 3$ and $n = 5$ respectively. Both curves display a synchronized peak in the SNR around D_{SR} of 0.94 fW/Hz.

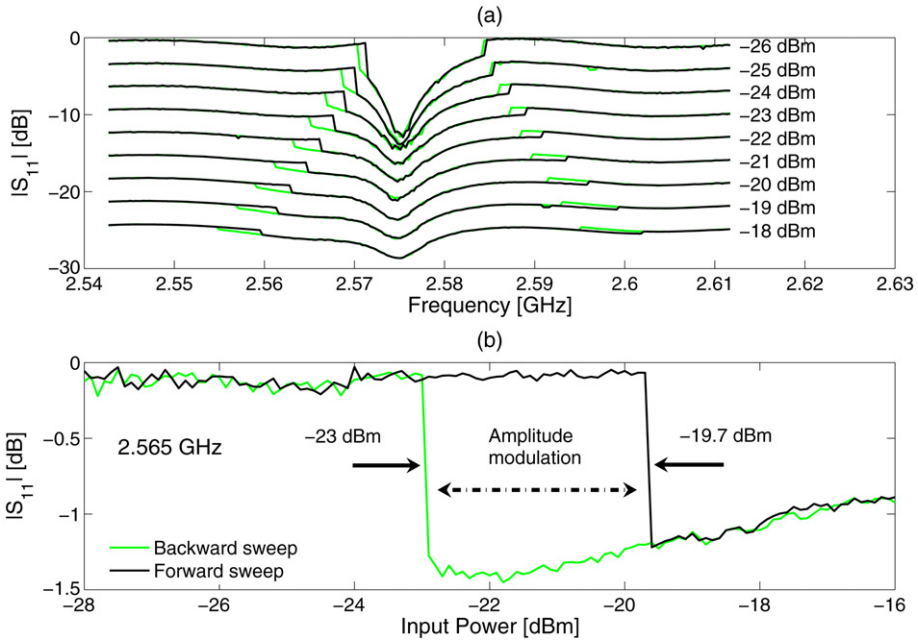

Fig. 1. (Color online.) (a) Forward and backward frequency sweeps applied to the first mode of the resonator at ∼2.57 GHz. The sweeps exhibit hysteresis loops at both sides of the resonance line shape. The plots which correspond to different input powers were shifted by a vertical offset for clarity. (b) Reflected power hysteresis measured at a constant angular frequency $\omega_p = 2\pi \times 2.565$ GHz which resides within the left-side metastable region of the resonance. For both plots the black (dark) line represents a forward sweep whereas the green (light) line represents a backward sweep.

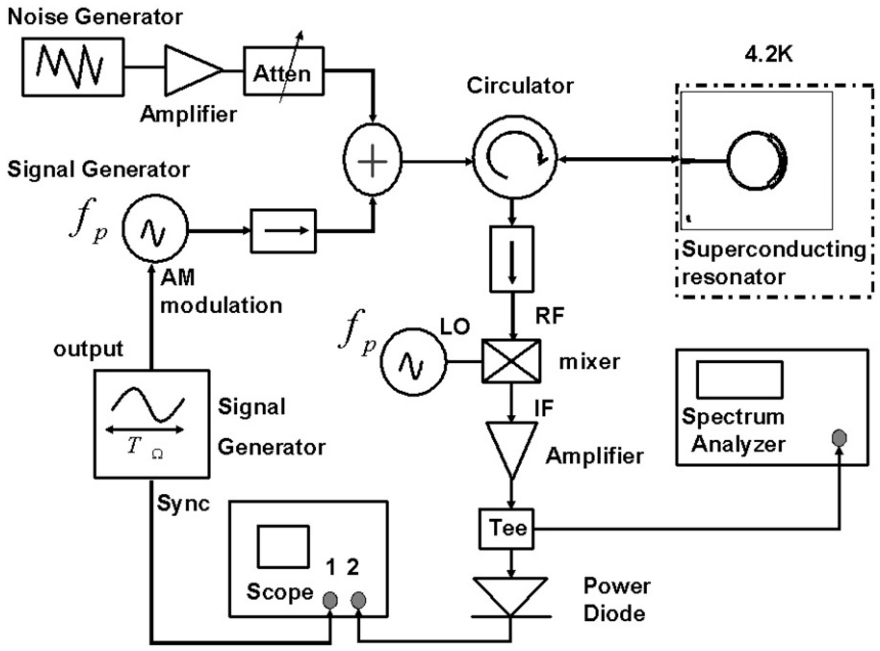

Fig. 2. Schematic drawing of the experimental setup used to measure SR. The microwave signal generator and the local oscillator at frequency f_p were phase-locked. The layout of the resonator is shown at the top-right corner.

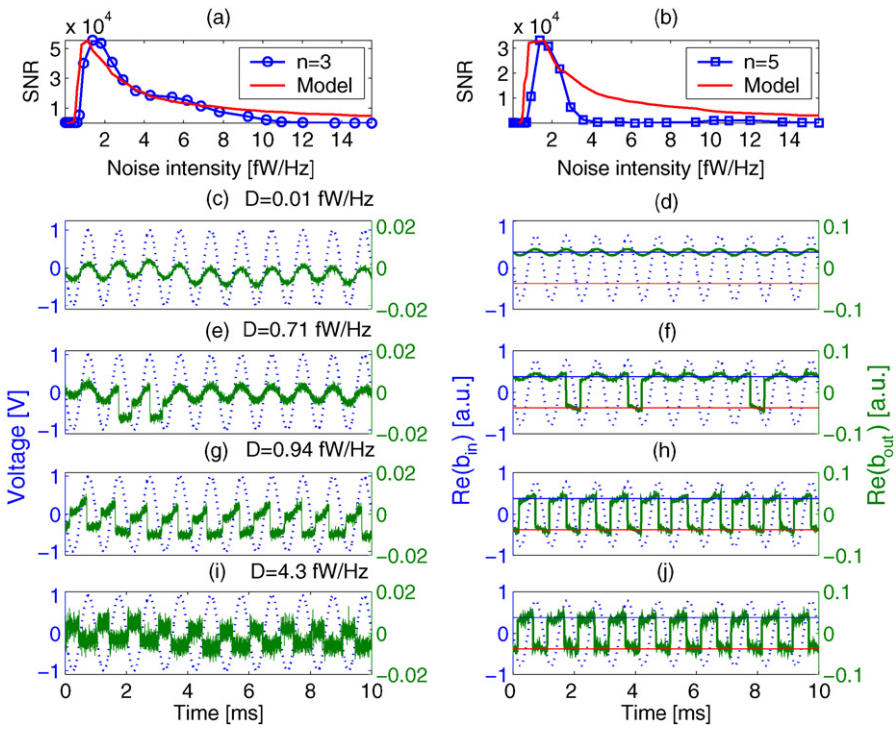

Fig. 3. (Color online.) Panels (a) and (b) show measured (blue) and simulated (red) SNR curves of the output harmonics $n = 3$ and $n = 5$ as a function of the input noise intensity. Panels (c), (e), (g) and (i) at the left exhibit typical snapshots of the reflected signal measured in the time domain as the input noise intensity D is increased. While panels (d), (f), (h) and (j) show the corresponding simulation results. Panels (c)–(d) and (e)–(f) correspond to noise intensities below D_{SR}. Panels (g)–(h) correspond to a noise intensity of $D_{\mathrm{SR}} = 0.94$ fW/Hz. Panels (i)–(j) correspond to noise intensities higher than D_{SR}. The dotted sinusoidal blue line represents the modulation signal. While the upper (blue) and lower (red) constant lines plotted in the simulation results represent the steady state solution of the resonator in the (S) and (N) phases of the hot spot. The simulation parameters used are: $\omega_{0n} = 2\pi \times 2.57$ GHz, $\omega_{0s}/\omega_{0n} = 1.002$, $\gamma_{1s}/\omega_{0n} = 1.1 \times 10^{-3}$, $\gamma_{2s}/\omega_{0n} = 2.7 \times 10^{-3}$, $\gamma_{1n}/\omega_{0n} = 10^{-3}$, $\gamma_{2n}/\omega_{0n} = 2 \times 10^{-3}$, $\omega_p/\omega_{0n} = 0.9991$, $(b^{\mathrm{in}})^2/\omega_{0n} = 9 \times 10^9$, $\Omega/2\pi = 1$ kHz, $T_0 = 4.2$ K, $T_c = 10.7$ K, $C = 1.2 \times 10^{-12}$ J/K, $H = 3 \times 10^{-5}$ W/K.

The data of the first harmonic (not shown here) exhibit an SNR peak of 2×10^5 at D_{SR}.

Typical results of SR measured in the time domain are shown in the left panels of Fig. 3. Panels (c) and (e) correspond to

low noise levels below D_{SR}. Panel (c) shows the reflected sinusoidal at $\Omega/2\pi = 1$ kHz without jumps. Panel (e) shows the reflected sinusoidal containing a few arbitrary jumps. Whereas, panel (g) which corresponds to the resonance noise D_{SR} exhibits one jump in the reflected signal at every half cycle. Thus, satisfying generally the *time-scale matching condition* for SR given by $\tau(D_{SR}) = T_\Omega/2$, where $T_\Omega = 2\pi/\Omega$ and $\tau(D)$ is the metastable state lifetime corresponding to the noise intensity D [1]. In panel (i) on the other hand, the case of a noise level higher than D_{SR} is shown at which the coherence between the modulating drive and the noise is lost and the noise fluctuations almost completely screen the signal.

In order to retrieve the experimental results observed in the time and frequency domains shown in Fig. 3, we employ the theoretical model elaborated in [13], according to which, the nonlinear dynamics exhibited by the system can be described to a large extent using two coupled equations of motion, one for the slowly varying amplitude of the resonator mode B given by

$$\frac{dB}{dt} = \left[i(\omega_p - \omega_0) - \gamma\right]B - i\sqrt{2\gamma_1}b^{in} + c^{in}, \tag{4}$$

and the other for the hot spot temperature T (the model assumes one dominant hot spot) which reads

$$C\frac{dT}{dt} = Q - W, \tag{5}$$

where ω_0 is the angular resonance frequency, b^{in} is the amplitude of the coherent tone injected to the resonator feedline $b^{in}e^{-i\omega_p t}$, $\gamma = \gamma_1 + \gamma_2$, where γ_1 is the coupling factor between the resonator and the feedline, γ_2 is the damping rate of the mode, C is the thermal heat capacity, $Q = \hbar\omega_0 2\gamma_2|B|^2$ is the power heating up the hot spot, $W = H(T - T_0)$ is the power of the heat transfer to the coolant which is assumed to be at temperature T_0, while H is the heat transfer coefficient. The term c^{in} represents an input noise with a random phase $\langle c^{in}\rangle = 0$ and an autocorrelation function $\langle c^{in}(t)c^{in*}(t')\rangle = G\omega_0\delta(t - t')$, where $G = \gamma D/\hbar\omega_0^2$. Whereas in order to obtain the reflected signal $b^{out}e^{-i\omega_p t}$ the following input–output relation is used [13]

$$b^{out} = b^{in} - i\sqrt{2\gamma_1}B. \tag{6}$$

Furthermore, this model assumes a step function dependence of the resonator parameters $\omega_0, \gamma_1, \gamma_2$ on the hot spot temperature T. As T exceeds the critical temperature T_c (the hot spot in the normal (N) phase) the resonator is characterized by ω_{0n}, γ_{1n}, γ_{2n}, while in the complementary case where $T \leqslant T_c$ (the hot spot in the superconducting (S) phase), these parameters equal ω_{0s}, γ_{1s}, γ_{2s}.

Due to the dependence of the stored energy inside the resonator on the resonance frequencies and the damping rates of the resonator, and the dependence of these parameters on the temperature of the hot spot, the system may have, in general, up to two locally-stable steady states, corresponding to the S and N phases of the hot spot. The stability of each of these phases depends on both the power and frequency parameters of the injected pump tone. In general there exist four different stability zones [17] (see Fig. 4). Two are monostable zones, where either the S phase or the N phase is locally stable. Another is a bistable zone, where both phases are locally stable. The third is an astable zone, where none of the phases are locally stable. Consequently, by setting the average value of $(b^{in})^2$ (which is proportional to the pump power) such that the system is located within the bistable region (see Fig. 4), and further determining an appropriate small amplitude ac component (which represents the signal with frequency Ω), one gets the theoretical fit lines (red) plotted in Fig. 3(a) and (b). Thus, apart from the y-axis scaling factor applied to coincide the SNR peaks with those of the data, the model, despite its simplicity, yields a relatively good agreement with the experimental data. Likewise, a good agreement is obtained also in the time domain, where the time simulations (d), (f), (h), (j) are drawn at the right of the corresponding measurement results. The constant upper (blue) and lower (red) lines shown in these panels correspond to the steady state of the resonator (hot spot) in the S and N phases respectively. It is worthwhile mentioning that some of the model parameters applied in the simulation (listed in the caption of Fig. 3) were measured directly (ω_{0n}, ω_{0s}, T_0, T_c, $\Omega/2\pi$, ω_p), whereas others were set to typical values characterizing superconducting nonlinear resonators made of NbN (γ_1, γ_2, C, H) [11].

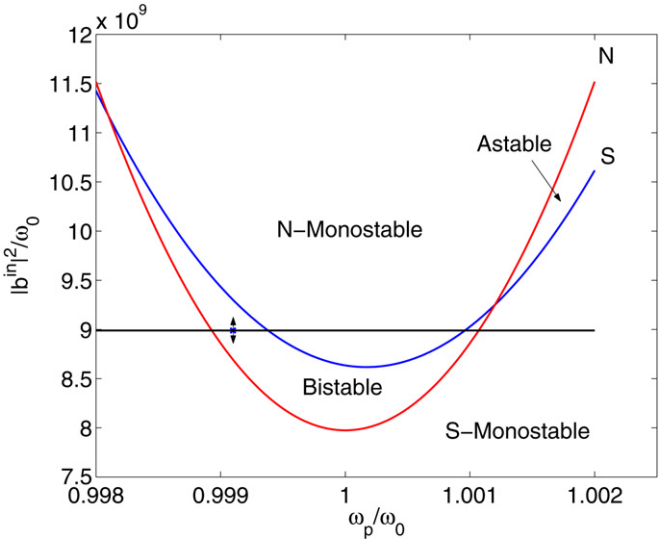

Fig. 4. (Color online.) Stability diagram showing the stability zones of the simulated nonlinear system as a function of the injected pump power and frequency. The red and blue lines in the figure denoted by N and S represent respectively the threshold of the N and S states, which consequently divides the pump power-frequency plane into four stability zones. Two are monostable zones, where either the S phase or the N phase is locally stable. Another is a bistable zone, where both phases are locally stable. The third is an astable zone, where none of the phases are locally stable. The working point employed in the simulation is indicated by a small cross drawn within the bistable region, while the vertical double arrow passing through this point illustrates the operation of an AM modulation. The various model parameters employed in the simulation are listed in the caption of Fig. 3.

Moreover, by inspecting the time response of the measurement results mainly panels (g) and (i), we find that the reflected modulated signals exhibit a rather rectangular shape. Such distortion of the sinusoidal shape at the output is very likely to originate from the dispersive character of the system response

as was suggested in Refs. [4,18]. Furthermore, by comparing these experimental data to the simulation plots exhibited in panels (h) and (j), one can verify that the suggested theoretical model manages to reproduce this feature as well.

In conclusion, nonlinear NbN superconducting resonators have been shown to exhibit SR when driven into the bistable region. Simulations based on the thermal instability model of the system succeeds to reproduce most of the measured SR features. Moreover, amplification of a slowly varying AM signal carried by a microwave pump is shown to be feasible by establishing a resonant cooperation between the modulating signal and the injected stochastic noise. Hence, such amplification scheme may be applicable in communication area. Namely, amplifying weak AM signals modulating a high frequency carrier [19] (located within the resonator metastable region), by means of tuning the input noise. Though to some extent, the range of possible application in this area might be limited by the nonlinearity of this amplification mechanism.

Acknowledgements

This work was supported by the German Israel Foundation under grant 1-2038.1114.07, the Israel Science Foundation under grant 1380021, the Deborah Foundation, the Poznanski Foundation, the Russel Berrie nanotechnology institute, and MAFAT.

References

[1] L. Gammaitoni, P. Hänggi, P. Jung, F. Marchesoni, Rev. Mod. Phys. 70 (1998) 223;
L. Gammaitoni, F. Marchesoni, S. Santucci, Phys. Rev. Lett. 74 (1995) 1052.
[2] A.R. Bulsara, L. Gammaitoni, Phys. Today (March 1996) 39.
[3] P. Jung, P. Hänggi, Phys. Rev. A 44 (1991) 8032.
[4] M. Morillo, J. Gómez-Ordóñez, Phys. Rev. E 51 (1995) 999.
[5] R. Benzi, A. Satera, G. Parisi, A. Vulpiani, J. Phys. A 14 (1981) L453;
R. Benzi, et al., SIAM J. Appl. Math. 43 (1983) 565.
[6] A. Longtin, A. Bulsara, F. Moss, Phys. Rev. Lett. 67 (1991) 656;
J.E. Levin, J.P. Miller, Nature 380 (1996) 165.
[7] B. McNamara, K. Wiesenfeld, R. Roy, Phys. Rev. Lett. 60 (1988) 2626;
R. Rouse, S. Han, J.E. Lukens, Appl. Phys. Lett. 66 (1995) 108.
[8] A.D. Hibbs, A.L. Singsaas, E.W. Jacobs, A.R. Bulsara, J.J. Pekkedahl, F. Moss, J. Appl. Phys. 77 (1995) 2582.
[9] R.L. Badzey, P. Mohanty, Nature 437 (2005) 995.
[10] R. Almog, S. Zaitsev, O. Shtempluck, E. Buks, Appl. Phys. Lett. 90 (2007) 013508.
[11] B. Abdo, E. Segev, O. Shtempluck, E. Buks, IEEE Trans. Appl. Supercond. 16 (2006) 1976;
B. Abdo, et al., Phys. Rev. B 73 (2006) 134513.
[12] M. Bier, R.D. Astumian, Phys. Rev. Lett. 71 (1993) 1649;
M. Bier, R.D. Astumian, Phys. Lett. A 247 (1998) 385.
[13] B. Abdo, E. Segev, O. Shtempluck, E. Buks, J. Appl. Phys. 101 (2007) 083909.
[14] E. Segev, B. Abdo, O. Shtempluck, E. Buks, Phys. Lett. A 366 (2007) 160.
[15] M.I. Dykman, D.G. Luchinsky, R. Mannella, P.V.E. McClintock, N.D. Stein, N.G. Stocks, Phys. Rev. E 49 (1994) 1198;
M.I. Dykman, D.G. Luchinsky, P.V.E. McClintock, N.D. Stein, N.G. Stocks, JETP Lett. 58 (1993) 145.
[16] H.B. Chan, C. Stambaugh, Phys. Rev. B 73 (2006) 224301;
H.B. Chan, C. Stambaugh, Phys. Rev. B 73 (2006) 172302.
[17] E. Segev, B. Abdo, O. Shtempluck, E. Buks, J. Phys.: Condens. Matter 19 (2007) 096206.
[18] M.I. Dykman, D.G. Luchinsky, R. Mannella, P.V.E. McClintock, N.D. Stein, N.G. Stocks, J. Stat. Phys. 70 (1993) 463.
[19] M. Golio (Ed.), The RF and Microwave Handbook, CRC Press, 2001.

4.5 Escape rate of metastable states in a driven NbN superconducting microwave resonator

Escape rate of metastable states in a driven NbN superconducting microwave resonator

Baleegh Abdo,[a] Eran Segev, Oleg Shtempluck, and Eyal Buks
Department of Electrical Engineering, Technion, Haifa 32000, Israel

(Received 8 November 2006; accepted 28 February 2007; published online 30 April 2007)

We study thermal instability and formation of local hot spots in a driven nonlinear NbN superconducting microwave resonator. White noise injected into the resonator results in transitions between the metastable states via a process consisting of two stages. In the first stage, the input noise entering the system induces fluctuations in the resonator mode. While in the second one, these mode fluctuations result in phase transitions of the hot spot due to induced temperature fluctuations. The associated noise-activated escape rate is calculated theoretically and measured also experimentally by means of driving the system into stochastic resonance. A comparison between theory and experiment yields a partial agreement. © *2007 American Institute of Physics*.
[DOI: 10.1063/1.2722241]

I. INTRODUCTION

The simple model of noise activated escape of a Brownian particle over a potential barrier succeeds to explain the basic behavior of a large number of metastable systems in nature.[1] Examples of such systems can be found in almost all major fields of science: physics, chemistry, biology, and even engineering.[2] For instance, it explains biochemical reactions in alternating current-driven protein,[3] the lifetime of zero-voltage state in Josephson junctions,[4,5] the magnetization reversal in nanomagnets,[6–8] noise-activated switching in micro-[9] and nanomechanical[10,11] oscillators, and photon-assisted tunneling in semiconductor hetrostructures.[12]

A well-known pioneering work on the subject is Krammer's in 1940. In his seminal paper,[13] he derived relatively simple expressions for the thermally induced escape rate in a one-dimensional asymmetric double-well potential. In general, these escape rate expressions take the form of $\Gamma = \Gamma_0 \exp(-U_b/k_B T)$, where U_b is the potential barrier height, k_B is the Boltzmann's constant, T is the temperature (where the limit $k_B T \ll U_b$ is assumed), and Γ_0 is a rate prefactor. Important extensions and refinements to this formula aimed either to include a wider range of damping regimes[14–16] or accommodate the solutions to other cases such as nonequilibrium systems, have been contributed by many authors over the years.[17–19] Examples of such nonequilibrium systems are metastable potentials modulated by deterministic forces,[20] e.g., the case of stochastic resonance,[21,22] or metastable systems subjected to nonwhite noise.[23,24] Moreover, efforts have been invested also in extending Krammer's rate theory to describe metastable systems in the quantum limit,[1,25,26] where escape is dominated by tunneling.

In the present article we study the escape rate of metastable states of thermally instable superconducting stripline resonators both theoretically and experimentally. In recent studies[27,28] we have experimentally demonstrated such instability in NbN superconducting resonators. The measured response of the system to a monochromatic excitation was accounted for by a theoretical model, which attributed the instability to a local hot spot in the resonator, switching between the superconducting and the normal phases. Nonlinearity, according to this model, results due to coupling between the equations of motion for both, the mode amplitude in the resonator and the temperature of the hot spot. The coupling mechanism is based on the dependence of both, the resonance frequency and the damping rate of the resonator on the stripline impedance, which in turn depends on the temperature of the hot spot. Moreover, we have employed this instability to demonstrate experimentally intermodulation gain,[29] stochastic resonance,[30] self-sustained modulation of a monochromatic drive,[31,32] period doubling bifurcation, and noise squeezing.[33]

In the case of thermally instable superconducting stripline resonators, the escape mechanism governing the lifetime of the metastable states differs in general from many of the examples mentioned earlier. In this case, the input noise induces escape in a two-stage process. The direct coupling between the input noise and the driven mode leads to fluctuations in the mode amplitude, which in turn, induce fluctuations in the heating power applied to the hot spot. Consequently, the fluctuating heating power, which is characterized by a finite correlation time, leads to temperature fluctuations. Escape occurs when the temperature approaches the critical value and a phase transition takes place in the hot spot.

The remainder of this article is organized as follows. In Sec. II the steady state solutions of the equation of motion for the resonator-mode are derived for the case of local heating instability. In Sec. III a perturbative approach is applied in order to include the effect of thermal fluctuations. In Sec. IV an escape rate expression characterizing the metastable states of the resonator is obtained. In Sec. V a brief explanation regarding stochastic resonance measurement is given. While in Secs. V A and V B, stochastic resonance measurement results are employed in order to extract some of the transition rate parameters characterizing the system. Finally, a brief summary concludes this article in Sec. VI.

[a]Electronic mail: baleegh@tx.technion.ac.il

II. STEADY STATE SOLUTIONS

Consider the case of a superconducting stripline microwave resonator weakly coupled to a feedline. Driving the resonator by a coherent tone $a_1^{\text{in}}=b^{\text{in}}e^{-i\omega_p t}$ injected into the feedline, excites a mode in the resonator with an amplitude $A=Be^{-i\omega_p t}$, where ω_p is the drive angular frequency, b^{in} is a constant complex amplitude proportional to the drive strength, and $B(t)$ is a complex mode amplitude which is assumed to vary slowly on the time scale of $1/\omega_p$.

A. Mode amplitude

In this approximation, the equation of motion for B reads[34]

$$\frac{dB}{dt}=[i(\omega_p-\omega_0)-\gamma]B-i\sqrt{2\gamma_1}b^{\text{in}}+c^{\text{in}}, \tag{1}$$

where ω_0 is the angular resonance frequency, $\gamma=\gamma_1+\gamma_2$, where γ_1 is the coupling factor between the resonator and the feedline and γ_2 is the damping rate of the mode. The term c^{in} represents an input noise with a random phase

$$\langle c^{\text{in}}\rangle=0, \tag{2}$$

and autocorrelation functions given by

$$\langle c^{\text{in}}(t)c^{\text{in}}(t')\rangle=\langle c^{\text{in}^*}(t)c^{\text{in}^*}(t')\rangle=0, \tag{3}$$

$$\langle c^{\text{in}}(t)c^{\text{in}^*}(t')\rangle=G\omega_0\delta(t-t'). \tag{4}$$

By further assuming a thermal equilibrium condition at temperature T_{eff} and a relatively high temperature case $k_BT_{\text{eff}}\gg\hbar\omega_0$, one has

$$G=\frac{\gamma}{\omega_0}\frac{k_BT_{\text{eff}}}{\hbar\omega_0}. \tag{5}$$

Rewriting Eq. (1) in terms of the dimensionless time $\tau=\omega_0 t$ and using the steady state solution

$$B_\infty=\frac{i\sqrt{2\gamma_1}b^{\text{in}}}{i(\omega_p-\omega_0)-\gamma}, \tag{6}$$

yields the following compact form:

$$\frac{db}{d\tau}+\lambda b=\frac{c^{\text{in}}}{\omega_0}, \tag{7}$$

where $b=B-B_\infty$ represents the difference between the mode amplitude variable and the steady state solution, while λ reads

$$\lambda=\frac{\gamma-i(\omega_p-\omega_0)}{\omega_0}. \tag{8}$$

By applying the methods of Gardiner and Collett introduced in Ref. 35, one can obtain the following input-output relation:

$$b^{\text{out}}=b^{\text{in}}-i\sqrt{2\gamma_1}B, \tag{9}$$

which relates the output signal $a_1^{\text{out}}=b^{\text{out}}e^{-i\omega_p t}$ reflected off the resonator to the input signal $a_1^{\text{in}}=b^{\text{in}}e^{-i\omega_p t}$ entering the system.

Thus, the reflection parameter r in steady state is in general given by

$$r=\frac{b^{\text{out}}}{b^{\text{in}}}=\frac{\gamma_2-\gamma_1-i(\omega_p-\omega_0)}{\gamma_2+\gamma_1-i(\omega_p-\omega_0)}, \tag{10}$$

which is obtained by substituting B_∞ of Eq. (6) in the input-output relation given by Eq. (9) and dividing by the input drive amplitude b^{in}.

B. Heat balance of local heating

Assuming that the resonator nonlinearity is dominated by a local hot spot in the stripline resonator, and that the hot spot area is sufficiently small in order to consider its temperature T to be homogeneous, the heat balance equation reads[36]

$$C\frac{\mathrm{dT}}{\mathrm{dt}}=Q-W, \tag{11}$$

where C is the thermal heat capacity of the hot spot, Q is the power heating up the hot spot given by $Q=\alpha Q_t$, where Q_t is the total power dissipated in the resonator given by $Q_t=\hbar\omega_0 2\gamma_2|B|^2$ and α is a positive coefficient $0\leq\alpha\leq1$, while $W=H(T-T_0)$ is the power of the heat transfer to the coolant, which is assumed to be at a constant temperature T_0, where H is the heat transfer coefficient to the substrate.

In terms of the dimensionless time τ and the dimensionless temperature given by

$$\Theta=\frac{T-T_0}{T_c-T_0}, \tag{12}$$

Equation (11) reads

$$\frac{d\Theta}{d\tau}+g(\Theta-\Theta_\infty)=0, \tag{13}$$

where the following quantities have been defined:

$$g=\frac{H}{C\omega_0}, \tag{14}$$

and

$$\Theta_\infty=\frac{2\hbar\alpha\gamma_2|B|^2}{gC(T_c-T_0)}. \tag{15}$$

Hence, the steady state solution of Eq. (13), reads

$$\Theta_{\infty 0}=\frac{2\hbar\alpha\gamma_2|B_\infty|^2}{gC(T_c-T_0)}. \tag{16}$$

Moreover, if one further assumes that the fluctuation of B around B_∞ is relatively small, one can rewrite Eq. (13) in the following form:

$$\frac{d\theta}{d\tau}+g\theta=f, \tag{17}$$

where

$$\theta=\Theta-\Theta_{\infty 0}, \tag{18}$$

and f reads

$$f = g\Theta_{\infty 0}\left[\frac{b}{B_\infty} + \left(\frac{b}{B_\infty}\right)^*\right], \tag{19}$$

where second order in b was neglected.

In general, when a hot spot is generated or alternatively diminished in the stripline, it affects the resonator parameters ω_0, γ_1, γ_2, and α and may induce as a result jumps in the resonance response curve. Moreover, as we have already shown in previous publications,[27,28] most of the nonlinear experimental results exhibited by our superconducting NbN resonators can be modeled to a very good extent by assuming a step function dependence of the resonator parameters ω_0, γ_1, γ_2, and α on the hot spot dimensionless temperature Θ,

$$\omega_0 = \begin{cases} \omega_{0s} & \Theta < 1 \\ \omega_{0n} & \Theta > 1 \end{cases}, \quad \gamma_1 = \begin{cases} \gamma_{1s} & \Theta < 1 \\ \gamma_{1n} & \Theta > 1 \end{cases}, \tag{20}$$

$$\gamma_2 = \begin{cases} \gamma_{2s} & \Theta < 1 \\ \gamma_{2n} & \Theta > 1 \end{cases}, \quad \alpha = \begin{cases} \alpha_s & \Theta < 1 \\ \alpha_n & \Theta > 1 \end{cases}. \tag{21}$$

In addition, we have shown that, in general, while disregarding noise, the coupled Eqs. (7) and (13) may have up to two different steady state solutions. A superconducting steady state (S) of the hot spot exists when $\Theta_{\infty 0} < 1$, or alternatively when $E = |B|^2 < E_s$, where $E_s = gC(T_c - T_0)/2\alpha_s\gamma_{2s}\hbar$. Similarly, a normal steady state (N) of the hot spot exists when $\Theta_{\infty 0} > 1$, or alternatively when $E > E_n$, where $E_n = gC(T_c - T_0)/2\alpha_n\gamma_{2n}\hbar$.

III. FLUCTUATIONS

In this section we assume a nonzero noise term $c^{\text{in}}(t)$ entering the resonator, thus giving rise to fluctuations around the steady state solution of the system.

A. Mode fluctuations

In this case the solution of Eq. (7) reads

$$b(\tau) = b(0)e^{-\lambda\tau} + \frac{1}{\omega_0}\int_0^\tau c^{\text{in}}(\tau')e^{\lambda(\tau'-\tau)}d\tau'. \tag{22}$$

For relatively long times $\gamma\tau/\omega_0 \gg 1$ one gets by using Eq. (2) a zero mean value of the mode fluctuation b,

$$\langle b(\tau)\rangle = 0, \tag{23}$$

whereas by using Eqs. (3) and (4), respectively, one obtains the following autocorrelation functions:

$$\langle b(\tau_1)b(\tau_2)\rangle = \langle b^*(\tau_1)b^*(\tau_2)\rangle = 0, \tag{24}$$

and

$$\langle b(\tau_1)b^*(\tau_2)\rangle = \frac{G\omega_0}{2\gamma}e^{-\lambda^*|\tau_2-\tau_1|}, \tag{25}$$

which implies that fluctuations in the heating power of the hot spot are characterized by a finite correlation time which is set by the resonator parameter λ.

B. Local heating fluctuations

Similarly, the solution of the heat balance Eq. (17) can be written as

$$\theta(\tau) = \langle\theta(\tau)\rangle + \Delta_\theta(\tau), \tag{26}$$

where

$$\langle\theta(\tau)\rangle = \theta(0)e^{-g\tau}, \tag{27}$$

is the mean value of θ variable and

$$\Delta_\theta(\tau) = \int_0^\tau f(\tau')e^{g(\tau'-\tau)}d\tau', \tag{28}$$

is the deviation from the mean value.

The variance of θ, which is denoted as $\langle\Delta_\theta^2(\tau)\rangle$, can be derived with the use of Eqs. (28), (19), and (25). In the case of small τ, namely the case when $g\tau \ll 1$ and $|\lambda|\tau \ll 1$, one has to lowest order in τ,

$$\langle\Delta_\theta^2(\tau)\rangle = \frac{g^2\Theta_{\infty 0}^2}{|B_\infty|^2}\frac{2G\omega_0\tau^2}{\gamma}. \tag{29}$$

On the other hand, for relatively long times $g\tau \gg 1$ one finds

$$\langle\Delta_\theta^2\rangle = \frac{G\Theta_{\infty 0}^2}{|B_\infty|^2}\frac{g\omega_0^2}{\gamma}\frac{\gamma + g\omega_0}{(\gamma + g\omega_0)^2 + (\omega_p - \omega_0)^2}. \tag{30}$$

As transitions between S and N states depend also on the rate at which the temperature of the hot spot changes, one needs to calculate the fluctuations in this quantity as well. Thus, by taking the square of Eq. (17) one obtains

$$\zeta^2 + g\frac{d(\theta^2)}{d\tau} + g^2\theta^2 = f^2, \tag{31}$$

where the variable ζ represents the temperature change rate

$$\zeta(\tau) \equiv \frac{d\theta}{d\tau}. \tag{32}$$

Expressing $\zeta(\tau)$ as a sum of a mean value and a deviation terms in a similar manner to Eq. (26) yields

$$\zeta(\tau) = \langle\zeta(\tau)\rangle + \Delta_\zeta(\tau). \tag{33}$$

To evaluate the variance of $\zeta(\tau)$, which is denoted as $\langle\Delta_\zeta^2(\tau)\rangle$, in the limit of relatively long times we employ Eqs. (31), (30), and (19) and the autocorrelation functions given in Eqs. (24) and (25) to get

$$\langle\Delta_\zeta^2\rangle = \frac{g^2G\Theta_{\infty 0}^2}{|B_\infty|^2}\frac{\omega_0}{\gamma}\frac{(\omega_p - \omega_0)^2 + \gamma(\gamma + g\omega_0)}{(\gamma + g\omega_0)^2 + (\omega_p - \omega_0)^2}. \tag{34}$$

IV. ESCAPE RATE

Escape from S to N states originates from a flux at point $\Theta = 1$ (or $\theta = 1 - \Theta_{\infty 0}$) flowing from $\Theta < 1$ to $\Theta > 1$, or vise versa for the case of escape from N to S states. Thus, the escape rate is given by

$$\Gamma = \omega_0 \int_0^\infty \zeta f(1 - \Theta_{\infty 0}, \zeta) d\zeta, \tag{35}$$

where $f(\theta, \zeta)$ is the joint probability distribution function of the random variables θ and ζ. As was shown earlier, in the limit of relatively long times where $g\tau \gg 1$, the expectation values $\langle\theta\rangle$ and $\langle\zeta\rangle$ vanish. In general, $f(\theta, \zeta)$ is expected to represent a joint normal distribution. Moreover, θ and ζ variables become statistically independent as the expectation value $\langle\theta^2\rangle$ becomes time independent (which applies in the above limit $g\tau \gg 1$). This can be readily inferred from the following relation:

$$\langle \Delta_\theta \Delta_\zeta \rangle = \frac{1}{2} \frac{d\langle\theta^2\rangle}{d\tau} - \langle\theta\rangle\langle\zeta\rangle, \tag{36}$$

which can be obtained by a direct substitution of Δ_θ and Δ_ζ definitions given by Eqs. (26) and (33).

Thus, by applying the previous approximations one finds

$$\Gamma = \frac{\omega_0 \exp\left[-\frac{(1-\Theta_{\infty 0})^2}{2\langle\Delta_\theta^2\rangle}\right]}{2\pi\sqrt{\langle\Delta_\theta^2\rangle\langle\Delta_\zeta^2\rangle}} \int_0^\infty \zeta \exp\left(-\frac{\zeta^2}{2\langle\Delta_\zeta^2\rangle}\right) d\zeta. \tag{37}$$

Furthermore, by evaluating the above integral, substituting instead of G and $\Theta_{\infty 0}$ [given by Eqs. (5) and (16) respectively], and using the simplifying notations

$$C\prime = \frac{1}{2} \frac{(\gamma + g\omega_0)^2 + (\omega_p - \omega_0)^2}{g\omega_0(\gamma + g\omega_0)}, \tag{38}$$

$$\Gamma_0 = \frac{\omega_0}{2\pi} \sqrt{\frac{g[(\omega_p - \omega_0)^2 + \gamma(\gamma + g\omega_0)]}{\omega_0(\gamma + g\omega_0)}}, \tag{39}$$

one gets

$$\Gamma = \Gamma_0 \exp\left[-\frac{C\prime(U_c - U_\infty)^2}{U_\infty k_B T_{\text{eff}}}\right], \tag{40}$$

where

$$U_\infty = \hbar\omega_0 |B_\infty|^2, \tag{41}$$

is the energy stored in the resonator corresponding to the steady state amplitude B_∞, and

$$U_c = \hbar\omega_0 |B_c|^2, \tag{42}$$

is the mode energy corresponding to the critical amplitude B_c at which $\Theta_{\infty 0} = 1$, namely

$$1 = \Theta_{\infty 0} = \frac{2\hbar\alpha\gamma_2 |B_c|^2}{gC(T_c - T_0)}. \tag{43}$$

Note that typically in our NbN devices[28] $\gamma/g\omega_0 \simeq 10^{-2}$. Thus, by assuming the limit $\gamma/g\omega_0 \ll 1$, and the resonance case $\omega_p = \omega_0$, the above rate expression appearing in Eq. (40) reduces into

$$\Gamma = \frac{\sqrt{g\omega_0\gamma}}{2\pi} \exp\left[-\frac{1}{2}\frac{(U_c - U_\infty)^2}{U_\infty k_B T_{\text{eff}}}\right]. \tag{44}$$

V. STOCHASTIC RESONANCE

In order to examine experimentally the escape rate expression derived in Eq. (40), we employed stochastic resonance technique. Basically, stochastic resonance phenomenon demonstrates how a weak periodic signal, applied to a nonlinear metastable system, can be amplified at the system output with the aid of certain amount of zero-mean Gaussian white noise. The amplification of the signal occurs when a resonant cooperation is established between the small periodic signal and the white noise entering the system. In general, such a coherent interaction between the signal and the noise occurs when the angular frequency Ω of the signal, which periodically modulates the double-well potential of the system, becomes comparable to the escape rate of the metastable states in the presence of the white noise.

One advantage of applying this measurement technique is that once the system is tuned at the stochastic resonance condition statistical data belonging to both metastable transitions can be gathered simultaneously.

In the experiment we employed a superconducting resonator which is made of NbN and implements a stripline geometry. The center conductor film of the resonator of thickness 2200 Å was direct current-magnetron sputtered on a 34 mm × 30 mm × 1 mm sapphire substrate in an ambient gas mixture of Ar/N_2 at room temperature. The resonator patterning was done using standard ultraviolet lithography and ion milling. Additional fabrication process parameters are listed in Ref. 27. Whereas further modeling and characterization of these nonlinear devices are discussed in Ref. 28.

One direct manifestation of the metastability states of the resonator, is the occurrence of jumps in the resonance line shape as can be seen for example in Fig. 2(a), where a reflection parameter measurement of the first resonance mode of the resonator at $f_0 = \omega_0/2\pi \simeq 2.575$ GHz is shown. The different plots corresponding to an increasing input power were shifted downward by a constant offset for clarity. Moreover, as the pump frequency is swept in the forward and backward directions two frequency hysteresis loops emerge at both sides of the resonant curve. Thus revealing the frequency range at which the system is metastable.

On the other hand, in Fig. 2(b) we show a reflected power hysteretic behavior measured at a constant frequency $f_p = \omega_p/2\pi = 2.565$ GHz as the input power is swept up and down. This frequency was chosen as it falls within the instable region of the fundamental mode for a certain input power range as can be inferred from the measurements appearing in panel (a). Thus, in order to drive our resonators into metastability, we have applied based on the earlier observations a coherent microwave signal at frequency f_p and input power of $P_0 = -21.5$ dBm. Moreover, in order to tune the resonator into stochastic resonance condition, we have applied a small sinusoidal forcing to the system in the form of amplitude modulation (AM) and injected a thermal white noise with an adjustable intensity to the resonator port. The applied noise intensity was measured and calibrated separately using a spectrum analyzer.

A schematic illustration of the stochastic resonance measurement setup used is depicted in Fig. 1. A continuous mi-

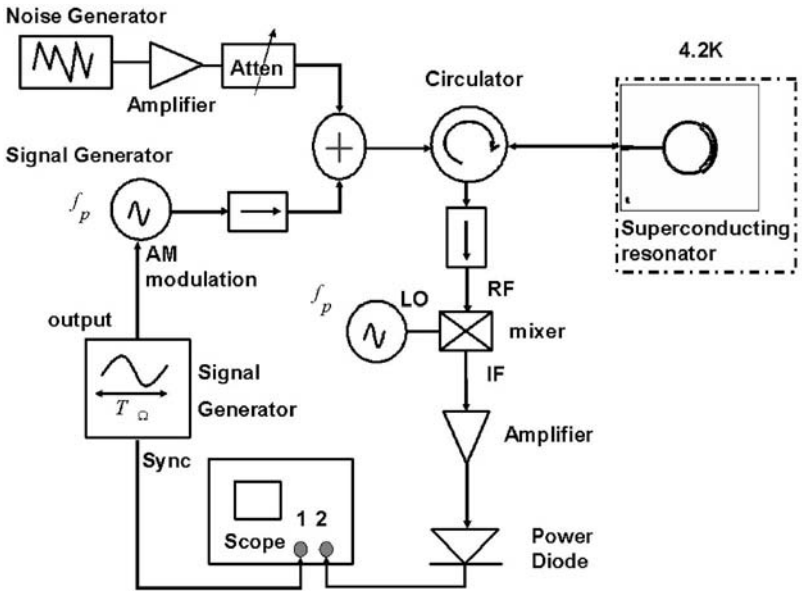

FIG. 1. Schematic block diagram of the experimental setup used. The microwave signal generator and the local oscillator at frequency f_p were phase locked. The layout of the resonator is shown at the top-right corner.

crowave signal at frequency f_p is amplitude modulated at frequency $f_\Omega = \Omega/2\pi = 1$ kHz. The modulated signal which effectively modulates the height of the potential barrier is combined with a white noise generated by a noise source and fed to the superconducting resonator. While the reflected signal off the resonator is mixed with a local oscillator phase-locked at frequency f_p and measured in the time domain using an oscilloscope. Additional information regarding stochastic resonance phenomenon measured in these nonlinear superconducting resonators is summarized in Ref. 30.

A. Escape rate measurement

At stochastic resonance condition, the lifetime of the metastable states becomes approximately equal to half the modulation period. Thus, assuming that the system has two metastable states designated by S_u and S_d (corresponding eventually to S and N states), it is expected to have one metastable state escape event each half time cycle. Such behavior is indeed seen in Fig. 3, which shows a typical result taken in the time domain at stochastic resonance condition, where the jumps appearing in the output signal correspond to alternating $S_d \rightarrow S_u$ and $S_u \rightarrow S_d$ transitions.

The blue dotted line in the figure represents the amplitude modulation signal, which modulates the escape rates Γ_1 and Γ_2 of the corresponding transitions $S_d \rightarrow S_u$ and $S_u \rightarrow S_d$, while the green solid line represents the modulated signal. In the vicinity of the minimum (maximum) points of the amplitude modulation signal (the blue dotted line), the escape rate $\Gamma_1(\Gamma_2)$ obtains its largest value, which is denoted as $\Gamma_{m1}(\Gamma_{m2})$. Hence, by letting $\tau_1(\tau_2)$ be the time difference between the time of the transition event $S_d \rightarrow S_u(S_u \rightarrow S_d)$ and the time at which the corresponding escape rate assumes its largest value, [namely the time at which Γ_1 equals Γ_{m1} (Γ_2 equals Γ_{m2})], the probability density characterizing this random variable $\tau_1(\tau_2)$ which will be denoted by $f_1(\tau_1)[f_2(\tau_2)]$, could be determined experimentally by building a normalized histogram of the measured times $\tau_1(\tau_2)$.

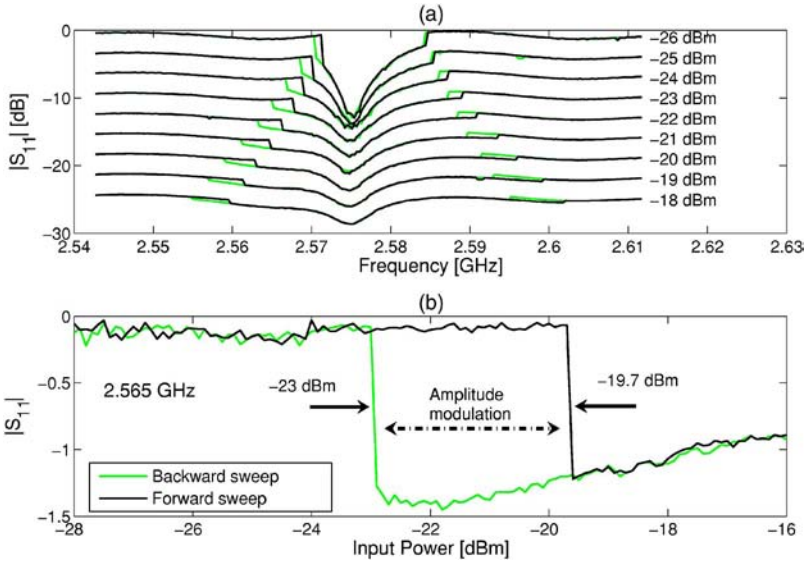

FIG. 2. (Color online). (a) Forward and backward frequency sweeps applied to the first mode of the resonator at ~2.575 GHz. The sweeps exhibit hysteresis loops at both sides of the resonance line shape. The plots corresponding to different input powers were shifted by a vertical offset for clarity. (b) Reflected power hysteresis measured at a constant angular frequency of $\omega_p = 2\pi 2.565$ GHz which resides within the left-side metastable region of the resonance. For both plots the black (dark) line represents a forward sweep whereas the green (light) line represents a backward sweep.

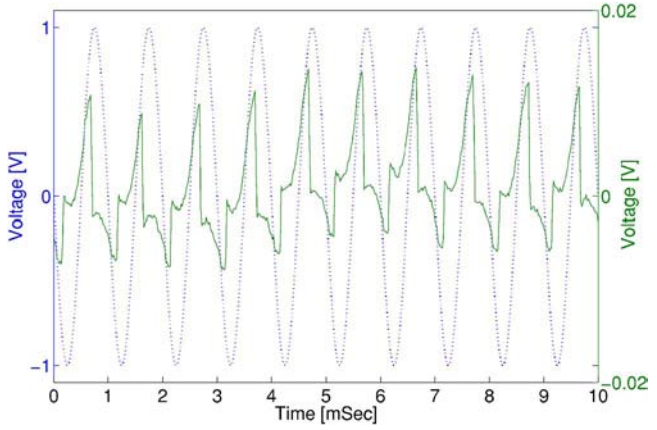

FIG. 3. (Color online). A typical snapshot of the time domain as the resonator is tuned into stochastic resonance condition. The solid (green) line represents the reflected modulated signal, corresponding to ten modulation cycles out of 5000 employed in the analysis. The dotted (blue) sinusoidal line represents the modulation signal applied to the microwave signal generator.

As can be seen from Eq. (A12) in the Appendix, the prefactors Γ_{m1} and Γ_{m2} can be estimated from the expectation value and the variance of the corresponding random variables τ_1 and τ_2. However, a more accurate value of the prefactor Γ_m can be obtained by invoking Eq. (A3) and employing a probability density function $f(\tau)$ fitted to the data.

In Figs. 4(a) and 4(b) we show the measured probability densities $f_1(\tau_1)$ and $f_2(\tau_2)$ extracted from 5000 modulation cycles sampled in the time domain. The solid line in both panels correspond to a Gaussian function fitted to the probability density measured in each case. The transition rate $\Gamma_1(\Gamma_2)$ as a function of the random variable $\tau_1(\tau_2)$, which is calculated using Eq. (A3) and the Gaussian fit applied to the data, is shown in the inset of Fig. 4(a) [Fig. 4(b)]. From these plots one can estimate the following rate values $\Gamma_{m1} \simeq 4.6 \times 10^5$ Hz and $\Gamma_{m2} \simeq 2.7 \times 10^5$ Hz which, as stated before, correspond to the transitions $S_d \rightarrow S_u$ and $S_u \rightarrow S_d$, respectively.

TABLE I. Calculated and measured model parameters.

	$S_d \rightarrow S_u$	$S_u \rightarrow S_d$
$g(10^{-3})$	1.56	1.56
γ(MHz)	37.6	18.6
P_c (dBm)	−23	−19.6
$\Delta P_{\text{in}}(10^{-6}$ W)	0.12	1.2
$\lvert r\rvert^2$	0.55	0.8
$k_B T_{\text{eff}}$(fW/Hz)	1.4	1.4
Γ_0(Hz)	8×10^6	8.3×10^6
Γ_m(Hz) (calc.)	7.8×10^6	1.9×10^6
Γ_m(Hz) (meas.)	4.6×10^5	2.7×10^5

B. Discussion

In order to obtain an estimate for the escape rates Γ_{m1} and Γ_{m2} corresponding to the $S_d \rightarrow S_u$ and $S_u \rightarrow S_d$ transitions, respectively, based on the theoretical model, we rewrite Eq. (40) in terms of the feedline input power P_{in} at the extremum of the AM, and the power difference $\Delta P_{\text{in}} \equiv P_c - P_{\text{in}}$, where P_c is the critical input power being proportional to the critical energy U_c,

$$\Gamma_m = \Gamma_0 \exp\left[-C\prime \left(\frac{\Delta P_{\text{in}}}{P_{\text{in}}} \right)^2 \frac{U_\infty}{k_B T_{\text{eff}}} \right]. \tag{45}$$

Furthermore, instead of the stored energy U_∞ appearing in the earlier expression, one can substitute the following equation:

$$U_\infty = \frac{P_{\text{in}}(1 - |r|^2)}{2\gamma}, \tag{46}$$

which basically relates the transmitted input power to the resonator $P_t = P_{\text{in}}(1 - |r|^2)$ in steady state, to the dissipated power at resonance which according to Eq. (1) is given by $2\gamma U_\infty$.

Estimates for the model parameters corresponding to both $S_d \rightarrow S_u$ and $S_u \rightarrow S_d$ transitions are summarized in Table I. Estimates for the coupling parameter γ corresponding to

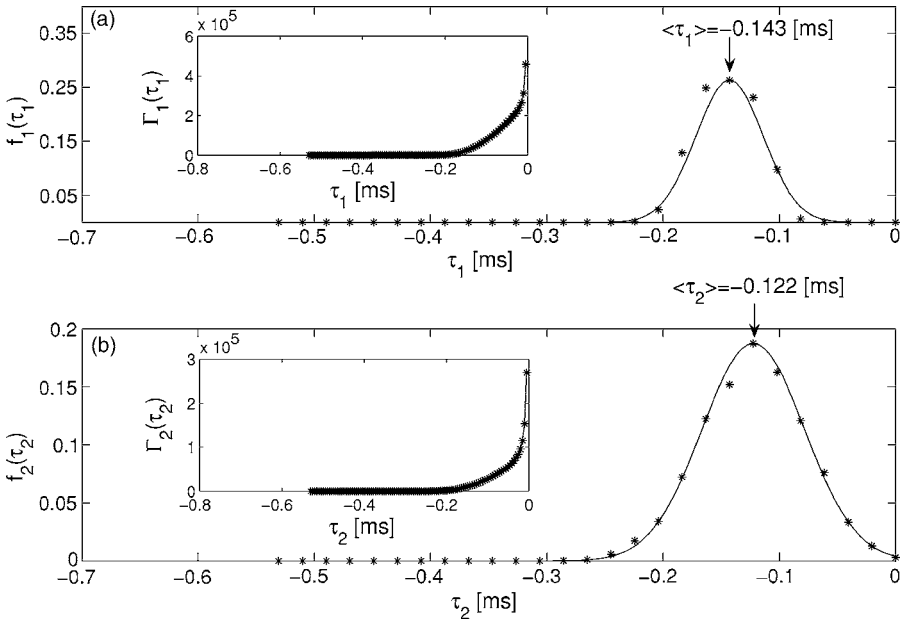

FIG. 4. Gaussian probability density functions $f_1(\tau_1)$ and $f_2(\tau_2)$ fitted to the experimental data which correspond to the $S_d \rightarrow S_u$ transition in panel (a) and to the $S_u \rightarrow S_d$ transition in panel (b). The escape rates Γ_1 and Γ_2 associated with both transitions are plotted in the insets of panels (a) and (b), respectively as a function of the random time variables τ_1 and τ_2 according to Eq. (A3).

the S_u and the S_d states have been extracted indirectly by fitting Eq. (10) to the measured reflection parameter curves versus the pump frequency ω_p in the vicinity of the resonance.[37] Whereas, the cooling parameter g, which is defined in Eq. (14), has been estimated using experimentally measured material properties of NbN,[38–40] yielding the value $g \simeq 1.56 \times 10^{-3}$ (see Refs. 28 and 32). Employing these estimates together with the experimental values of P_c, ΔP_{in}, and r and substituting in Eq. (45) yield a rough estimate for the escape rates $\Gamma_{m1} \simeq 7.8 \times 10^6$ Hz and $\Gamma_{m2} \simeq 1.9 \times 10^6$ Hz belonging to the $S_d \rightarrow S_u$ and the $S_u \rightarrow S_d$ transitions, respectively.

This discrepancy, found between the values of the escape rates obtained using the theoretical model as opposed to those extracted from the experimental data by about one order of magnitude, can be attributed to a large extent to the accumulated errors in the estimated values of the model parameters, some of which have been evaluated indirectly, as well as to many simplifying assumptions which the theoretical model employs in order to derive an analytical expression for the escape rate. As examples for model parameters which were determined indirectly and yet have a large effect on the escape rate value, one can name the g parameter which depends among others on the geometry of the hot spot and the thermal properties of the deposited NbN film, which are not known precisely, and also the coupling factor γ which is extracted using an approximate fitting procedure.[37]

VI. SUMMARY

In conclusion, a noise-activated escape rate expression was derived for the case of a nonlinear superconducting microwave resonator having a local-thermal instability. In order to determine the escape rate experimentally, stochastic resonance measurements were applied. A partial agreement is found between the theoretical and the experimental results up to one order of magnitude. Such discrepancy as has been argued, can be easily accounted for, by some of the shortcomings of the model and by possible uncertainties in the value of a few model parameters.

ACKNOWLEDGMENTS

This work was supported by the German Israel Foundation under Grant No. 1–2038.1114.07, the Israel Science Foundation under Grant No. 1380021, the Deborah Foundation, the Poznanski Foundation, and MAFAT.

APPENDIX: TRANSITION LIFETIME

Consider a system which has in general two metastable states designated by S_a and S_b and assume that at time $t = -t_0$ the system is in state S_b, where $t_0 > 0$. The transition rate Γ of the process $S_b \rightarrow S_a$ depends on an externally applied time varying parameter $p(t)$. Further assume that for p close to some fixed value p_m the transition rate is given approximately by

$$\Gamma(p) = \Gamma_m \exp\left(-\kappa^2 \frac{p - p_m}{p_m}\right), \tag{A1}$$

where both Γ_m and κ are positive constants.

The probability distribution function $F(\tau)$ for a transition of the kind $S_b \rightarrow S_a$ to take place within the time interval $(-t_0, \tau)$ is given by

$$F(\tau) = \int_{-t_0}^{\tau} f(t)dt, \tag{A2}$$

where $f(\tau)$ is the corresponding probability density. By definition, the following holds:

$$\frac{f(\tau)}{1 - F(\tau)} = \Gamma[p(\tau)]. \tag{A3}$$

The initial condition $F(-t_0) = 0$ and Eq. (A3) yield

$$f(\tau) = \Gamma[p(\tau)] \exp\{-\int_{-t_0}^{\tau} \Gamma[p(t)]dt\}. \tag{A4}$$

Further assume the case where at time $t = 0$ the function $p(t)$ obtains a local minimum $p(0) = p_m$. Near $t = 0$ one has

$$p(t) = p_m(1 + \Omega^2 t^2) + O(t^3). \tag{A5}$$

Thus, in the vicinity of $t = 0$ Eq. (A1) becomes

$$\Gamma(t) = \Gamma_m \exp(-\kappa^2 \Omega^2 t^2), \tag{A6}$$

and the following holds:

$$f(\tau) = \Gamma_m \exp\left[-\kappa^2 \Omega^2 \tau^2 - \sqrt{\pi} \frac{\Gamma_m}{\kappa \Omega} \frac{\text{erf}(\kappa \Omega \tau) + \text{erf}(\kappa \Omega t_0)}{2}\right]. \tag{A7}$$

Keeping terms up to second order in $\kappa \Omega \tau$ and assuming the case where

$$\left(-\kappa \Omega t_0 + \frac{\Gamma_m}{2\kappa \Omega}\right)^2 \gg 1, \tag{A8}$$

allow approximating the probability density $f(\tau)$ by

$$f(\tau) = \frac{\Omega \kappa}{\sqrt{\pi}} \exp\left[-\kappa^2 \Omega^2 \left(\tau + \frac{\Gamma_m}{2\kappa^2 \Omega^2}\right)^2\right]. \tag{A9}$$

In this approximation the random variable τ has a normal distribution function with a mean value

$$\mu_\tau = -\frac{\Gamma_m}{2\kappa^2 \Omega^2}, \tag{A10}$$

and a variance

$$\sigma_\tau^2 = \frac{1}{2\kappa^2 \Omega^2}, \tag{A11}$$

whereas, the parameters Γ_m and κ are given by

$$\Gamma_m = -\frac{\mu_\tau}{\sigma_\tau^2} \tag{A12}$$

and

$$\kappa^2 = \frac{1}{2\sigma_\tau^2 \Omega^2}. \tag{A13}$$

[1] P. Hänggi, P. Talkner, and M. Borkovec, Rev. Mod. Phys. **62**, 251 (1990).
[2] *Activated Barrier Crossing; Applications in Physics, Chemistry, and Biology*, edited by G. R. Fleming and P. Hänggi (World Scientific, Singapore, 1993).
[3] E. H. Serpersu and T. Y. Tsong, J. Membr. Biol. **74**, 191 (1983).
[4] T. A. Fulton and L. N. Dunkleberger, Phys. Rev. B **9**, 4760 (1974).
[5] M. Büttiker, E. P. Harris, and R. Landauer, Phys. Rev. B **28**, 1268 (1983).
[6] W. Wernsdorfer, E. B. Orozco, K. Hasselbach, A. Benoit, B. Barbara, N. Demoncy, and A. Loiseau, Phys. Rev. Lett. **78**, 1791 (1997).
[7] R. H. Koch, G. Grinstein, G. A. Keefe, Y. Lu, P. L. Trouilloud, W. J. Gallagher, and S. S. P. Parkin, Phys. Rev. Lett. **84**, 5419 (2000).
[8] E. B. Myers, F. J. Albert, J. C. Sankey, E. Bonet, R. A. Buhrman, and D. C. Ralph, Phys. Rev. Lett. **89**, 196801 (2002).
[9] C. Stambaugh and H. B. Chan, Phys. Rev. B **73**, 172302 (2006).
[10] J. S. Aldridge and A. N. Cleland, Phys. Rev. Lett. **94**, 156403 (2005).
[11] R. L. Badzey, G. Zolfagharkhani, A. Gaidarzhy, and P. Mohanty, Appl. Phys. Lett. **86**, 023106 (2005).
[12] B. J. Keay, S. J. Allen, Jr., J. Galán, J. P. Kaminski, K. L. Campman, A. C. Gossard, U. Bhattacharya, and M. J. W. Rodwell, Phys. Rev. Lett. **75**, 4098 (1995).
[13] H. A. Kramers, Physica (Amsterdam) **7**, 284 (1940).
[14] M. I. Dykman and M. A. Krivoglaz, Physica A **104**, 408 (1980).
[15] V. I. Mel'nikov and S. V. Meshkov, J. Chem. Phys. **85**, 1018 (1986).
[16] M. I. Dykman, I. B. Schwartz, and M. Shapiro, Phys. Rev. E **72**, 021102 (2005).
[17] R. Graham and T. Tél, Phys. Rev. A **31**, 1109 (1985).
[18] R. S. Maier and D. L. Stein, SIAM J. Appl. Math. **57**, 752 (1997).
[19] D. Ryvkine, M. I. Dykman, and B. Golding, Phys. Rev. E **69**, 061102 (2004).
[20] J. Lehmann, P. Reimann, and P. Hänggi, Phys. Rev. E **62**, 6282 (2000).
[21] M. I. Dykman, D. G. Luchinsky, R. Mannella, P. V. E. McClintock, N. D. Stein, and N. G. Stocks, Phys. Rev. E **49**, 1198 (1994).
[22] L. Gammaitoni, P. Hänggi, P. Jung, and F. Marchesoni, Rev. Mod. Phys. **70**, 223 (1998).
[23] H. S. Wio, P. Colet, M. S. Miguel, L. Pesquera, and M. A. Rodriguez, Phys. Rev. A **40**, 7312 (1989).
[24] S. J. B. Einchcomb and A. J. McKane, Phys. Rev. E **51**, 2974 (1995).
[25] P. Hänggi, J. Stat. Phys. **42**, 105 (1986).
[26] O. A. Tretiakov, T. Gramespacher, and K. A. Matveev, Phys. Rev. B **67**, 073303 (2003); O. A. Tretiakov and K. A. Matveev, Phys. Rev. B **71**, 165326 (2005).
[27] B. Abdo, E. Segev, O. Shtempluck, and E. Buks, IEEE Trans. Appl. Supercond. **16**, 1976 (2006).
[28] B. Abdo, E. Segev, O. Shtempluck, and E. Buks, Phys. Rev. B **73**, 134513 (2006).
[29] B. Abdo, E. Segev, O. Shtempluck, and E. Buks, Appl. Phys. Lett. **88**, 022508 (2006).
[30] B. Abdo, E. Segev, O. Shtempluck, and E. Buks, cond-mat/0606555.
[31] E. Segev, B. Abdo, O. Shtempluck, and E. Buks, cond-mat/0607259.
[32] E. Segev, B. Abdo, O. Shtempluck, and E. Buks, J. Phys.: Condens. Matter **19**, 096206 (2007).
[33] E. Segev, B. Abdo, O. Shtempluck, and E. Buks, Phys. Lett. A (to be published).
[34] B. Yurke and E. Buks, J. Lightwave Technol. **24**, 5054 (2006).
[35] C. W. Gardiner and M. J. Collett, Phys. Rev. A **31**, 3761 (1985).
[36] A. V. I. Gurevich and R. G. Mints, Rev. Mod. Phys. **59**, 941 (1987).
[37] B. Abdo, E. Segev, O. Shtempluck, and E. Buks, IEEE Trans. Appl. Supercond. (in press); cond-mat/0501236.
[38] M. W. Johnson, A. M. Herr, and A. M. Kadin, J. Appl. Phys. **79**, 7069 (1996).
[39] A. M. Kadin and M. W. Johnson, Appl. Phys. Lett. **69**, 3938 (1996).
[40] K. Weiser, U. Strom, S. A. Wolf, and D. U. Gubser, J. Appl. Phys. **52**, 4888 (1981).

4.6 Intermodulation and parametric amplification in a superconducting stripline resonator integrated with a dc-SQUID

A Letters Journal Exploring the Frontiers of Physics

March 2009

EPL, **85** (2009) 68001
doi: 10.1209/0295-5075/85/68001

www.epljournal.org

Intermodulation and parametric amplification in a superconducting stripline resonator integrated with a dc-SQUID

B. Abdo[1(a)], O. Suchoi[1], E. Segev[1], O. Shtempluck[1], M. Blencowe[2] and E. Buks[1]

[1] *Department of Electrical Engineering, Technion - Haifa 32000, Israel*
[2] *Department of Physics and Astronomy, Dartmouth College - Hanover, NH 03755, USA*

received 17 November 2008; accepted in final form 23 February 2009
published online 31 March 2009

PACS 85.25.Dq – Superconducting quantum interference devices (SQUIDs)
PACS 84.40.Dc – Microwave circuits
PACS 05.45.-a – Nonlinear dynamics and chaos

Abstract – We utilize a superconducting stripline resonator containing a dc-SQUID as a strong intermodulation amplifier exhibiting a signal gain of 24 dB and a phase modulation of 30 dB. Studying the system response in the time domain near the intermodulation amplification threshold reveals a unique noise-induced spikes behavior. We account for this response qualitatively via solving numerically the equations of motion for the integrated system. Furthermore, employing this device as a parametric amplifier yields an abrupt rise of 38 dB in the generated side-band signal.

The field of solid-state qubits and quantum information processing has received considerable attention during the past decade [1–4] and has successfully demonstrated several milestone results to date [5–11]. However, one of the fundamental challenges hindering this emerging field is noise interference, which either screens the output signal or leads to quantum state decoherence [5,6,12–15]. Hence, this may explain to some extent the renewed interest exhibited recently by the quantum measurement community in the field of parametric amplifiers [16–21]. This interest is driven essentially by two important properties of these amplifiers: 1) their capability to amplify very weak coherent signals; 2) their ability to squeeze noise below the equilibrium level by means of employing a homodyne setup and phase control. These properties are expected to be highly beneficial to the area of quantum communication [22,23] and to the generation of quantum squeezed states [16,17,24,25]. Additional interest in these high-gain parametric amplifiers arises from the large body of theoretical work predicting photon-generation from vacuum via the dynamical Casimir effect [26,27], which can be achieved by employing an appropriate parametric excitation mechanism [28,29].

In this present work we study a superconducting stripline microwave resonator integrated with a dc-SQUID [30–32]. The paper is mainly devoted to a novel amplification mechanism in which the relatively large nonlinear inductance of the dc-SQUID is exploited to achieve large gain in an intermodulation (IM) configuration. We provide theoretical evidence to support our hypothesis that the underlying mechanism responsible for the large observed gain is the metastability of the dc-SQUID. In addition, at the end of the paper we demonstrate another amplification mechanism, in which the dependence of the dc-SQUID inductance on the external magnetic field is exploited to achieve parametric amplification [20].

The device (see fig. 1(a)) is implemented on a high-resistivity 34 mm × 30 mm × 0.5 mm silicon wafer coated with a 100 nm thick layer of SiN. As a preliminary step, thick gold pads (300 nm) are evaporated at the periphery of the wafer. Following a stage of e-beam lithography, a two-angle shadow evaporation of aluminium [33] —with an intermediate stage of oxidation— realizes both the resonator and the two $Al/AlO_x/Al$ Josephson junctions comprising the dc-SQUID. The total thickness of the aluminium evaporated is 80 nm (40 nm at each angle).

In general, IM generation is often associated with the occurrence of nonlinear effects in the resonance curves of a superconducting resonator [34–38]. In fig. 2 we show a transmission measurement of the resonator response, obtained using a vector network analyzer at the resonance while sweeping the frequency upwards. The measured resonance resides at $f_0 = 8.219$ GHz which corresponds to

(a) E-mail: baleegh@tx.technion.ac.il

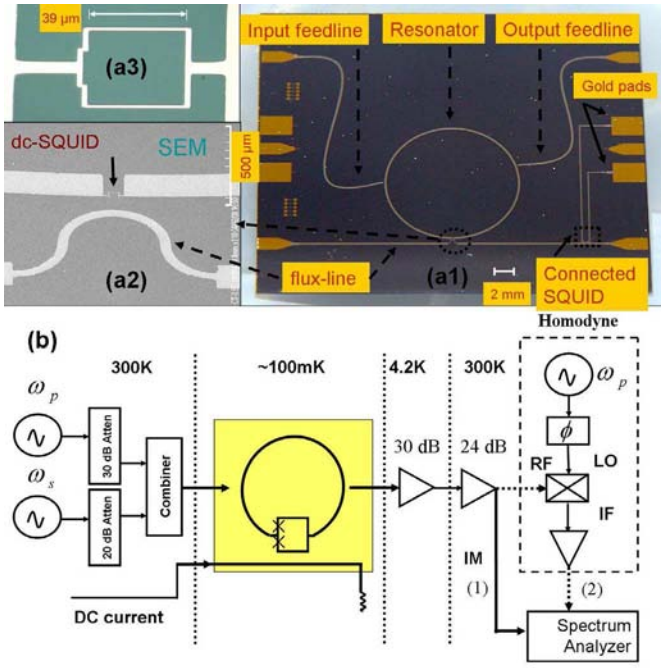

Fig. 1: (Color online) The device and IM setup. (a1) A photograph of the device consisting of a circular resonator with a circumference of 36.4 mm and a linewidth of 150 μm, a dc-SQUID integrated into the resonator and a flux line employed for driving rf-power and flux-biasing the dc-SQUID. The connected SQUID at the periphery of the wafer is employed for device characterization and dc measurements. (a2) An electron micrograph displaying the dc-SQUID incorporated in the resonator and the adjacent flux line. The area of the dc-SQUID fabricated is 39 μm $\times$39 μm, while the area of each junction is about 0.25 μm^2. The self-inductance of the dc-SQUID loop is $L_s = 1.3 \cdot 10^{-10}$ H and its total critical Josephson current is about $2I_c = 28\,\mu$A. (a3) A zoom-in optical-microscope image of the SQUID. (b) A basic IM setup. The pump and the signal designated by their angular frequency ω_p and ω_s, respectively, are combined by a power combiner and fed to the resonator. The field at the output is amplified using two amplification stages and measured using a spectrum analyzer (path 1). A dc current was applied to the flux line in order to flux-bias the dc-SQUID. Path (2) at the output corresponds to a homodyne setup employed in measuring IM.

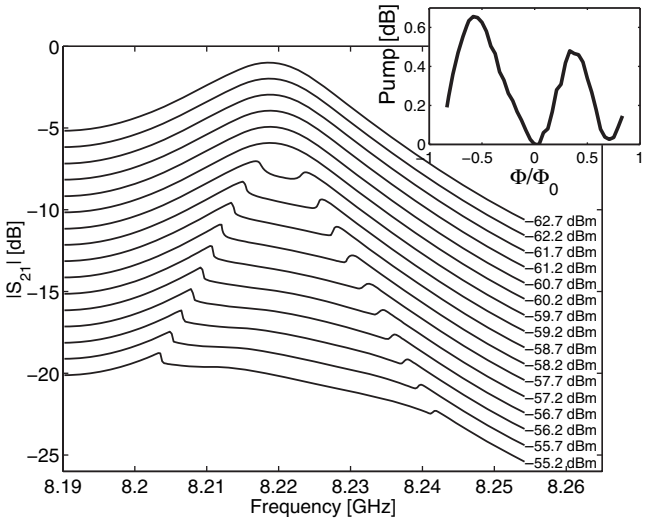

Fig. 2: Transmission response curves of the resonator at its third resonance (8.219 GHz) as a function of input power and frequency (the frequency was swept upwards). The resonance curves exhibit nonlinear effects at $P_p \geqslant P_c$. The loaded quality factor for this resonance in the linear regime is 350. The resonance curves corresponding to different input powers were offset by a 1 dB for clarity. The inset exhibits the relative change in the transmitted pump signal *vs.* the applied magnetic flux threading the dc-SQUID loop during an IM measurement. The measurement was taken at a fixed input pump power at the vicinity of P_c. The flux modulation is relative to zero-flux bias and was measured while sweeping the flux upwards.

the third resonance mode of the resonator having an anti-node of the rf-current waveform at the dc-SQUID position. Similar nonlinear effects in the transmission response have been measured at the first mode ($\simeq 2.766$ GHz) as well.

As can be seen in the figure, at excitation powers P_p below $P_c = -60.3$ dBm (at which nonlinear effects emerge) the resonance curve is linear and Lorentzian. As the input power is increased, abrupt jumps appear at both sides of the resonance. In addition, as one continues to increase the input power the resonance curves become shallower, broader and less symmetrical. Such power dependency can be attributed to the nonlinearity of the dc-SQUID inside the resonator which increases considerably as the amplitude of the driving current becomes comparable to the critical current.

The basic IM scheme used is schematically depicted in fig. 1(b). The input field of the resonator is composed of two sinusoidal fields generated by external microwave synthesizers and superimposed using a power combiner. The applied signals have unequal amplitudes. One, referred to as the pump, is an intense sinusoidal field with frequency f_p, whereas the other, referred to as the signal, is a small amplitude sinusoidal field with frequency $f_p + \delta$, where δ represents the frequency offset between the two signals. Due to the presence of a nonlinear element such as the dc-SQUID integrated into the resonator, frequency mixing between the pump and the signal yields an output idler field at frequency $f_p - \delta$. Thus the output field of the resonator, measured by a spectrum analyzer, consists mainly of three spectral components, the transmitted pump, the transmitted signal and the generated idler. The IM amplification in the signal, idler and the noise is obtained, as shown herein, by driving the dc-SQUID to its onset of instability via tuning the pump power. In the inset of fig. 2 we show how the device response changes during IM with respect to the flux degree of freedom at a constant pump power. Maximum IM amplification is attained near half-flux-quantum points.

In fig. 3 we show a typical IM measurement result. In this measurement the pump was tuned to the resonance

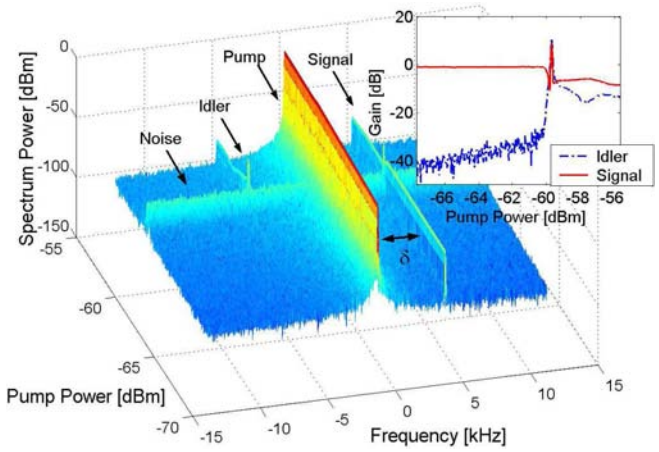

Fig. 3: (Color online) A spectrum power measured by a spectrum analyzer during IM operation as a function of increasing pump power while applying external flux $\Phi \simeq \Phi_0/4$, signal power $P_s = -110\,\mathrm{dBm}$, and frequency offset $\delta = 5\,\mathrm{kHz}$. The spectrum taken at a constant frequency span around f_p was shifted to dc for clarity. At the vicinity of P_c the system exhibits a large amplification. A cross-section of the measurement taken along the pump power axis is shown in the inset. The red line (solid line) and the blue line (dashdot line) exhibit the corresponding gain factors of the transmitted signal and the idler, respectively.

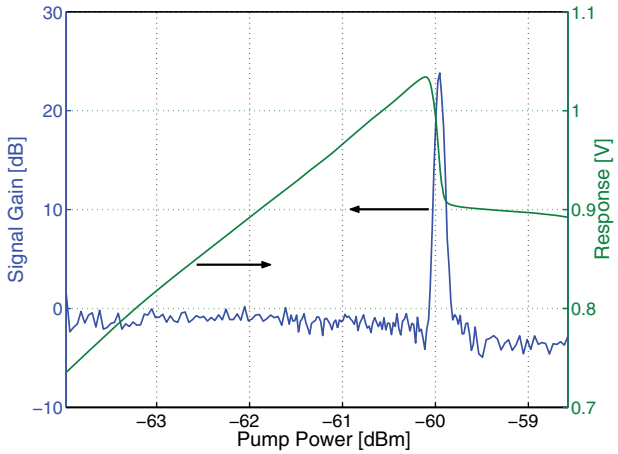

Fig. 4: (Color online) A signal gain (blue line) measured as a function of increasing pump power. The measurement was taken using a homodyne scheme. The signal displays a gain of about 24 dB at P_c. The corresponding dc component of the homodyne detector output (green line) was measured simultaneously using a voltage meter connected in parallel to the spectrum analyzer. In this measurement $\Phi \simeq \Phi_0/2$, $P_s = -110\,\mathrm{dBm}$, $\delta = 5\,\mathrm{kHz}$.

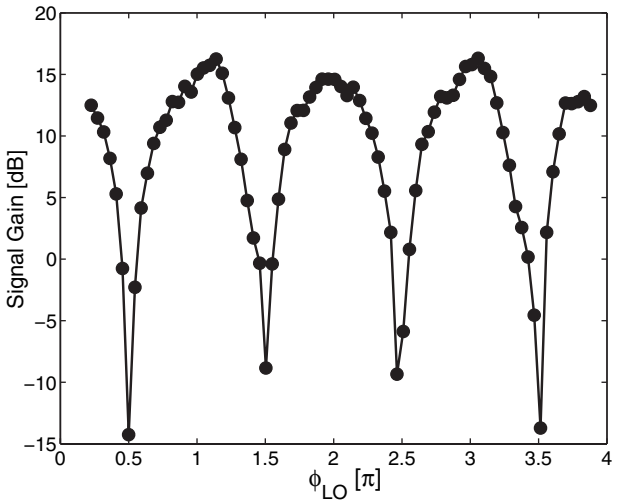

Fig. 5: A periodic dependence of the signal gain on the LO phase difference at the vicinity of P_c. The signal exhibits a large amplification and de-amplification at integer and half-integer multiples of π, respectively. The phase modulation dependency shows up to 30 dB peak-to-peak amplitude. In this measurement Φ, P_s and δ are the same as in the caption of fig. 4.

frequency $f_p = 8.219\,\mathrm{GHz}$. The signal power P_s was set to $-110\,\mathrm{dBm}$, and its frequency offset δ to 5 kHz. As the pump power injected into the resonator is increased, the nonlinearity of the dc-SQUID increases and consequently the frequency mixing between the pump and the signal increases as well. At about P_c the dc-SQUID reaches a critical point at which the idler, the signal and also the noise floor level (within the frequency bandwidth) undergo a large simultaneous amplification. The idler gain measured is 12 dB (see inset of fig. 3), where the signal/idler gain is defined as the ratio between the signal/idler power at the output feedline and the signal power at the input feedline. To this end, the losses and amplifications of the elements along each direction were calibrated with an uncertainty of ± 1 dB.

In order to show that this IM amplifier is also phase sensitive we applied a standard homodyne detection scheme as schematically depicted in fig. 1 (see path (2)), in which the phase difference between the pump and the local oscillator (LO) at the output —having the same frequency— can be varied. In such a scheme the pump is down-converted to dc, whereas both signal and idler are down-converted to the same frequency δ. The largest amplification is obtained when the LO phase (ϕ_{LO}) is adjusted such that the signal and idler tones constructively interfere. Shifting ϕ_{LO} by $\pi/2$ from the point of largest amplification results in destructive interference, which in turn leads to the largest de-amplification [16,17,24].

The IM measurement results, obtained using the homodyne setup while flux-biasing the dc-SQUID with about half-flux-quantum, are shown in figs. 4 and 5. Figure 4 exhibits the signal gain (blue line) *vs.* increasing applied pump power. As can be seen from the figure the signal gain assumes a peak of 24 dB for $P_p \simeq P_c$. Moreover, the response of the resonator at the pump frequency (green line) —measured simultaneously using a voltage meter connected in parallel to the spectrum analyzer— is drawn as well for comparison. The sharp drop in the region $P_p \sim P_c$, coinciding with the amplification of the signal,

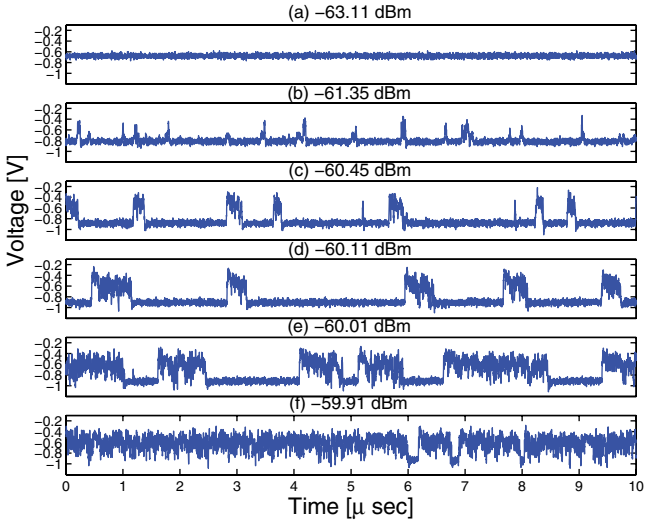

Fig. 6: (Color online) Snapshots of the resonator response measured in the time domain during an IM operation. (a)–(d) display the resonator response at pump powers lower than the critical value. (e) At the critical value. (f) Exceeding the critical value.

indicates that the transmitted pump is depleted and power is transferred to other frequencies.

Figure 5 exhibits a periodic dependence of the signal gain on ϕ_{LO}, having a gain modulation of about 30 dB peak to peak between the amplification and de-amplification quadratures. It is worthwhile mentioning that in this measurement not only the signal shows a periodic dependence on ϕ_{LO} but also the noise floor which exhibits up to 20 dB modulation (measured at $f_p + 1.5\delta$).

Another interesting aspect of this device is revealed by examining its response in the time domain while applying an IM measurement using the homodyne setup shown in fig. 1 (see path (2)). This is achieved by connecting a fast oscilloscope in parallel to the spectrum analyzer at the output. A few representative snapshots of the device behavior measured in the time domain are shown in fig. 6, where each subplot corresponds to a different applied pump power. In subplot (a) the pump power is about 3 dBm lower than the critical value and it displays a constant voltage level. As the pump power is increased (subplot (b)) separated spikes start to emerge. Increasing the power further causes the spikes to start bunching together and as a consequence forming larger groups (subplots (c) and (d)). This bunching process reaches an optimal point at the pump power corresponding to the peak in the IM gain (subplot (e)). Above that value, such as the case in subplot (f), the spikes become saturated and the gain drops.

Such behavior in the time domain reveals also the underlying mechanism responsible for the amplification. As is clear from the measurement traces the rate of spikes strongly depends on P_p at the vicinity of P_c, thus adding a small signal at $f_p + \delta$ (which is effectively equivalent to applying an amplitude modulation of the pump at frequency δ), results in modulation of the rate of spikes at the same frequency, and consequently yields a large response at the signal and the idler tones.

In an attempt to account for the unique temporal response presented in fig. 6, we refer to the two equations of motion governing the dc-SQUID system given by [39]

$$\begin{aligned} \beta_C \frac{\ddot{\delta}_1}{I_c}\left(\frac{\Phi_0}{2\pi R_J}\right)^2 + \dot{\delta}_1\left(\frac{\Phi_0}{2\pi R_J}\right) &= -\frac{\partial U}{\partial \delta_1} + I_{\mathrm{n}1} \\ \beta_C \frac{\ddot{\delta}_2}{I_c}\left(\frac{\Phi_0}{2\pi R_J}\right)^2 + \dot{\delta}_2\left(\frac{\Phi_0}{2\pi R_J}\right) &= -\frac{\partial U}{\partial \delta_2} + I_{\mathrm{n}2}, \end{aligned} \tag{1}$$

where Φ_0 is the flux quantum, R_J is the shunt resistance of the junctions, I_c is the critical current of each junction, δ_1, δ_2 are the gauge-invariant phase differences across junctions 1 and 2, respectively, I_{n1}, I_{n2} are equilibrium noise currents generated in the shunt resistors having —in the limit of high temperature— a spectral density of $S_{I_{\mathrm{n}}} = 4k_BT/R_J$, β_C is a dimensionless parameter defined as $\beta_C \equiv 2\pi I_c R_J^2 C_J/\Phi_0$, where C_J is the junction capacitance (herein we solve for the underdamped SQUID case where $\beta_C \gg 1$) and U is the potential energy of the system which reads

$$\begin{aligned} U = &-\frac{I}{2}(\delta_1+\delta_2) + \frac{2I_c}{\pi\beta_L}\left(\frac{\delta_1-\delta_2}{2} - \frac{\pi\Phi}{\Phi_0}\right)^2 \\ &-I_c(\cos\delta_1 + \cos\delta_2), \end{aligned} \tag{2}$$

where Φ is the applied magnetic flux, I is the bias current flowing through the dc-SQUID, and β_L is a dimensionless parameter defined as $\beta_L \equiv 2L_sI_c/\Phi_0$. While the circulating current flowing in the dc-SQUID loop is given by $I_{\mathrm{circ}}(t) = I_c(\delta_1 - \delta_2 - 2\pi\Phi/\Phi_0)/\pi\beta_L$.

Furthermore, in order to account for the resonator response as well, we make two simplifying assumptions: 1) We model our resonator as a series RLC tank oscillator characterized by an angular frequency $\omega_0 = 1/\sqrt{LC} = 2\pi \cdot 8.219\,\mathrm{GHz}$, and a characteristic impedance $Z_0 = \sqrt{L/C}$, where L and C are the inductance and the capacitance of the resonant circuit respectively. (2) We neglect the mutual inductance that may exist between the inductor and the dc-SQUID.

Under these simplifying assumptions, one can write the following equation of motion for the charge on the capacitor denoted by $q(t)$:

$$\frac{Z_0\ddot{q}}{\omega_0} + R\dot{q} + \omega_0 Z_0 q + V_{sq} + V_{\mathrm{in}} + V_{\mathrm{n}} = 0, \tag{3}$$

where V_{n} is a voltage noise term having —in the limit of high temperature— a spectral density of $S_{V_{\mathrm{n}}} = 4Rk_BT$, $V_{\mathrm{in}}(t) = \mathrm{Re}\,(V_0 e^{-i\omega_p t})$ is an externally applied sinusoidal voltage oscillating at the pump angular frequency ω_p and having a constant voltage amplitude V_0. Whereas, $V_{sq} = \Phi_0(\dot{\delta}_1 + \dot{\delta}_2)/4\pi$ designates the voltage across the dc SQUID. Using these notations the bias current in eq. (2) reads $I = \dot{q}$.

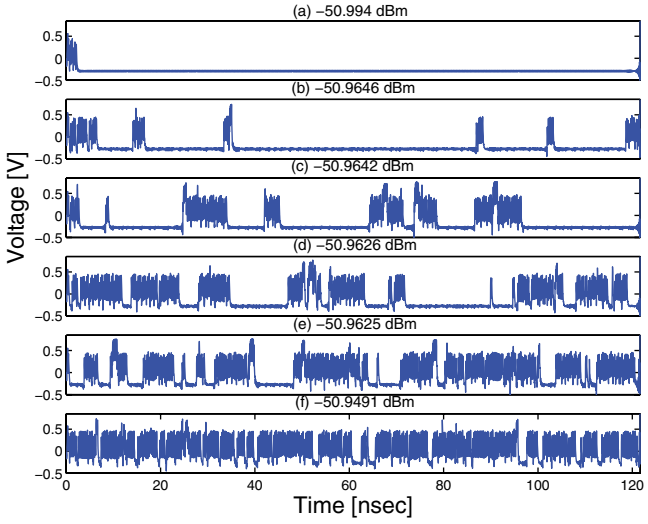

Fig. 7: (Color online) A simulation result. The output field exhibits spikes in the time domain similar to the spikes shown in fig. 6. The spikes occur whenever the system locus jumps from one well to another due to the presence of stochastic noise while driving the system near a critical point. In this simulation run the system was simulated over a period of 1000 time cycles of pump oscillations (one of the constraints set on the simulation was maintaining a reasonable computation time). The parameters that were employed in the simulation (same as experiment) are $\omega_0 = \omega_p = 2\pi \cdot 8.219\,\mathrm{GHz}$, $\beta_L = 3.99$, $R_J = 9.4\,\Omega$, $\Phi = \Phi_0/2$ and $\phi_{LO} = \pi$. The rest of the parameters were set in order to reproduce the measurement result: $\gamma_1 = 10^7\,\mathrm{Hz}$, $R = 3.3\,\Omega$, $\beta_C = 5.86$ and $Z_0 = 10\,\Omega$ (corresponding experimental values are: $\gamma_1 \simeq 2.4 \cdot 10^7\,\mathrm{Hz}$, $Z_0 \simeq 50\,\Omega$, C_J was not measured directly, a capacitance on the order of 0.7 pF was assumed).

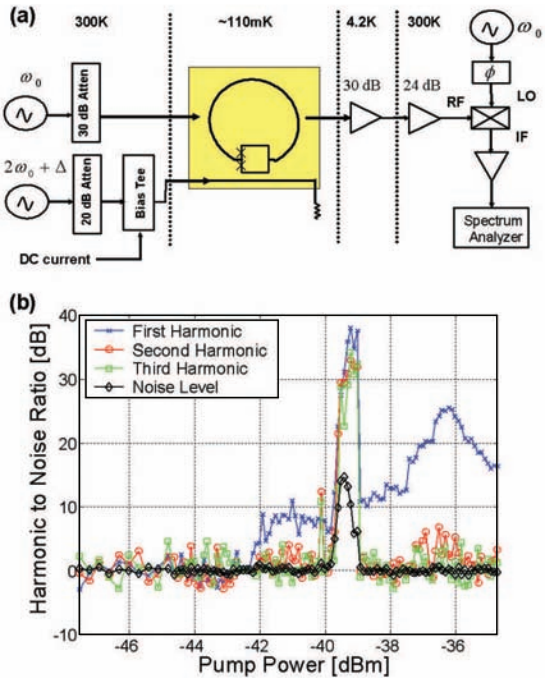

Fig. 8: (Color online) (a) A homodyne setup employed in measuring parametric excitation. Subplot (b) exhibits harmonic-to-noise ratio of the generated three harmonics at $\delta = 5\,\mathrm{kHz}$, 2δ, 3δ, as well as the noise spectral density at 1.5δ as a function of increasing pump power applied at $2f_0 + \delta$. All peaks in the power of the harmonics including the noise rise are measured relative to the noise floor at low pump power. In this measurement a maximum peak of 38 dB is attained at the first harmonic. The signal power applied to the resonator at f_0 is $P_s = -80\,\mathrm{dBm}$, while the external flux is $\Phi \simeq 0.6\Phi_0$.

Finally in order to relate the observed output signal in fig. 6 at the output of the homodyne scheme to the fast oscillating solution q, we first express the charge on the capacitor as $q(t) = \sqrt{2\hbar/Z_0}\mathrm{Re}\,[A(t)e^{-i\omega_p t}]$, where $A(t)$ is a slow envelope function, second, we employ the input-output relation [24], $V_{\mathrm{out}}(t) = V_0 - i\sqrt{32 Z_0 \hbar \gamma_1^2}A(t)$, where γ_1 is the coupling constant between the resonator and the feedline, in order to obtain the field at the output port. Third, we account for the phase shift by evaluating the expression $2V_{LO}\mathrm{Re}\,[V_{\mathrm{out}}(t)e^{i\phi_{LO}}]$, where V_{LO} corresponds to the amplitude of the LO.

By integrating these stochastic coupled equations of motion numerically, while employing device parameters which are relevant for our case, one finds that the observed temporal behavior of the system can be qualitatively explained in terms of noise-induced jumps between different potential wells forming the potential landscape of the dc-SQUID which is given by eq. (2). As a consequence of applying the voltage V_{in} to the integrated system, the potential landscape of the dc-SQUID oscillates at the pump frequency, and its oscillation amplitude grows with the amplitude of the incoming voltage. However, inter-well transitions of the system become most dominant as the oscillation voltage reaches a critical value at which the potential landscape of dc-SQUID becomes tilted enough —due to the current flowing in the system— in order to allow frequent noise-assisted escape events from one well to another or across several wells, which in turn cause a voltage drop to develop across the dc-SQUID and induce jumps in the circulating current. Such hopping of the system state is manifested as well in the homodyne output field response shown in fig. 7, which in a qualitative manner mimics successfully the main temporal features shown in fig. 6.

It is also clear from this inter-well transitions model that the amplification in this case is different from the so-called Josephson Bifurcation Amplifier (JBA) [14], as in the latter case the system is confined to only one well and the bifurcation occurs between two oscillation states having different amplitudes. The extent to which bifurcation amplifiers such as the presently considered one and the JBA are quantum-limited detectors [40,41], is still largely an open problem. As such it will be the subject of a future study [42].

Moreover, just as in the recent experiment by Yamamoto *et al.* [20] we have additionally employed our device as a parametric amplifier. To this end, we have used the parametric excitation scheme exhibited in fig. 8(a) in

which the pump and signal tones are applied to different ports. The main rf signal (pump) is applied to the flux-line at the vicinity of twice the resonance frequency of the resonator $2f_0 + \delta$ ($\delta \equiv \Delta/2\pi = 5\,\mathrm{kHz}$) and $2f_0 = 16.438\,\mathrm{GHz}$ does not coincide with any resonance of the device. Whereas, the signal, being several orders of magnitude lower than the pump, is fed to the resonator port at f_0 and its main purpose is to probe the system response.

In fig. 8(b) we exhibit a parametric excitation measurement result obtained using this device at $\Phi \simeq 0.6\Phi_0$. In this result there is evidence of one of the characteristic fingerprints of a parametric amplifier: the existence of an excitation threshold above which there is a noise rise and an abrupt amplification of the harmonic at δ (which results from a nonlinear frequency mixing at the dc-SQUID). As can be seen in the figure at about $-40\,\mathrm{dBm}$ the first harmonic generated at δ and the two higher-order harmonics at 2δ, 3δ rise abruptly and considerably up to a maximum of 38 dB measured at the first harmonic above the noise floor. Also in a separate measurement result (data not shown) the first harmonic has been found to display $\simeq 20\,\mathrm{dB}$ peak-to-peak modulation as a function of external magnetic field.

In conclusion, in this work we have designed and fabricated a superconducting stripline resonator containing a dc-SQUID. We have shown that this integrated system can serve as a strong sensitive amplifier. We have studied the device using IM measurement and parametric excitation. In both schemes the device exhibited distinct threshold behavior, strong noise rise and large amplification of coherent side-band signals generated due to the nonlinearity of the dc-SQUID. In addition, we have investigated the system response in the time domain during IM measurements. We have found that in the vicinity of the critical input power the system becomes metastable and consequently exhibits noise-activated spikes in the transmitted power. We have shown that this kind of behavior can be explained in terms of noise-assisted hopping of the system state between different potential wells. We have also demonstrated that the main features observed in the time domain can be qualitatively captured by solving the equations of motion for the dc-SQUID in the presence of rf-current bias and stochastic noise. Such a device may be exploited under suitable conditions in a variety of intriguing applications ranging from generating quantum squeezed states to parametric excitation of zero-point fluctuations of the vacuum.

* * *

This work was supported by the Israel Science Foundation, the Deborah Foundation, the Poznanski Foundation, Russel Berrie Nanotechnology Institute, US-Israel Binational Science Foundation and MAFAT. BA was supported by the Ministry of Science, Culture and Sports.

REFERENCES

[1] Nakamura Y. *et al.*, *Nature*, **398** (1999) 786.
[2] Shnirman A. *et al.*, *Phys. Rev. Lett.*, **79** (1997) 2371.
[3] Makhlin Y. *et al.*, *Rev. Mod. Phys.*, **73** (2001) 357.
[4] Bouchiat V. *et al.*, *Phys. Scr.*, **T76** (1998) 165.
[5] Vion D. *et al.*, *Science*, **296** (2002) 886.
[6] Chiorescu I. *et al.*, *Science*, **299** (2003) 1869.
[7] Lupascu A. *et al.*, *Phys. Rev. Lett.*, **93** (2008) 177006.
[8] Wallraff A. *et al.*, *Nature*, **431** (2004) 162.
[9] Martinis J. *et al.*, *Phys. Rev. Lett.*, **89** (2002) 117901.
[10] Yamamato T. *et al.*, *Nature*, **421** (2003) 823.
[11] Claudon J. *et al.*, *Phys. Rev. Lett.*, **93** (2004) 187003.
[12] Zorin A. B., *Phys. Rev. Lett.*, **76** (1996) 4408.
[13] Sillanpaa M. A. *et al.*, *Phys. Rev. Lett.*, **93** (2004) 066805.
[14] Siddiqi I. *et al.*, *Phys. Rev. Lett.*, **93** (2004) 207002.
[15] Schreier J. A. *et al.*, *Phys. Rev. B*, **77** (2008) 180502.
[16] Yurke B. *et al.*, *Phys. Rev. A*, **39** (1989) 2519.
[17] Movshovich R. *et al.*, *Phys. Rev. Lett.*, **65** (1990) 1419.
[18] Yurke B. *et al.*, *IEEE Trans. Magn.*, **25** (1989) 1371.
[19] Spietz L. *et al.*, *Appl. Phys. Lett.*, **93** (2008) 082506.
[20] Yamamoto T. *et al.*, *Appl. Phys. Lett.*, **93** (2008) 042510.
[21] Castellanos-Beltran M. A. and Lehnert K. W., *Appl. Phys. Lett.*, **91** (2007) 83509.
[22] Houck A. A. *et al.*, *Nature*, **449** (2007) 328.
[23] Hofheinz M. *et al.*, *Nature*, **454** (2008) 310.
[24] Yurke B. and Buks E., *J. Lightwave Technol.*, **24** (2006) 5054.
[25] Castellanos-Beltran M. A. *et al.*, *Nat. Phys.*, **4** (2008) 929.
[26] Barton G. *et al.*, *J. Opt. B: Quantum Semiclass. Opt.*, **7** (2005) S1.
[27] Dodonov V. V., *Adv. Chem. Phys.*, **119** (2001) 309.
[28] Segev E. *et al.*, *Phys. Lett. A*, **370** (2007) 202.
[29] Dodonov A. V. *et al.*, quant-ph/0806.4035 (2008).
[30] Sandberg M. *et al.*, *Appl. Phys. Lett.*, **92** (2008) 203501.
[31] Laloy A. P. *et al.*, *J. Low Temp. Phys.*, **151** (2008) 1034.
[32] Nation P. D. *et al.*, *Phys. Rev. B*, **78** (2008) 104516.
[33] Fulton T. A. and Dolan G. J., *Phys. Rev. Lett.*, **59** (1987) 109.
[34] Dahm T. and Scalapino D. J., *J. Appl. Phys.*, **81** (1997) 2002.
[35] Chen C. C. *et al.*, *Phys. Rev. B.*, **45** (1992) 4788.
[36] Monaco R. *et al.*, *J. Appl. Phys.*, **88** (2000) 2898.
[37] Abdo B. *et al.*, *Appl. Phys. Lett.*, **88** (2006) 22508.
[38] Tholen E. A. *et al.*, *Appl. Phys. Lett.*, **90** (2007) 253509.
[39] Koch R. H. *et al.*, *Appl. Phys. Lett.*, **38** (1981) 380.
[40] Nakano H. *et al.*, cond-mat/0808.1798v1 (2008).
[41] Dykman M. I., cond-mat/0810.5016v1 (2008).
[42] Blencowe M. P. *et al.*, in preparation.

Chapter 5

Discussion

We study superconducting stripline resonators coupled to nonlinear elements (weak-links, microbridges and dc-SQUIDs) with emphasis on the resultant nonlinear behavior and nonlinear dynamics.

In the first part of the research, we study a variety of strong nonlinear effects observed in NbN superconducting stripline resonators at relatively low input powers [61, 62]. Namely, sudden and abrupt jumps in the resonance curves, frequency and power hysteresis, resonance frequency shift and self-sustained modulation. To account for these unique effects we consider a theoretical model in which local heating of weak links and thermal instability are responsible for these effects and we show that such model yields a good agreement with the experiments. Moreover, we apply this theoretical model of thermal instability in order to calculate and measure experimentally the noise-activated escape rate of metastable states of the system [72, 73].

Furthermore, we utilize these strong nonlinearities in order to demonstrate two novel amplification schemes in superconducting resonators, the first is what is known as intermodulation amplification, where a small amplitude coherent signal is generated and amplified due to frequency mixing with an intense drive in the vicinity of an instability [63], while the second is the so called stochastic resonance phenomenon, where a weak modulating signal is amplified in the vicinity of a metastable state via coherent interaction with a certain amount of white noise [70, 73].

While, in the second part of the research, we study unique nonlinear effects observed in superconducting stripline resonators integrated with dc-SQUIDs [101], such as intermodulation and parametric amplification, phase-sensitive modulation, and noise-induced spikes in the time domain. To ac-

count for the temporal response of the system we solve numerically the equations of motion for the integrated system, and present theoretical simulations which exhibit a good agreement with the experimental data.

5.1 Nonlinear Dynamics in NbN Superconducting Resonators

5.1.1 Nonlinear Effects

The highlight of manuscripts [61, 62] is the study of novel nonlinear dynamics exhibited by NbN superconducting stripline resonators in the nonlinear region. The measured response which contains some extraordinary features in the resonance curves strongly suggests that the underlying physics is unique and that some conventional theoretical models which are commonly used to account for nonlinear properties in superconductors are inadequate in the present case.

The main contribution of these two papers can be summarized as follows:

1. Studying the nonlinear behavior exhibited by these devices under varying measurement conditions such as, input power, bidirectional frequency sweeps, white noise, magnetic field and rapid frequency sweeps.
2. Carrying a comprehensive comparison with other known nonlinearities and mechanisms.
3. Considering and developing a theoretical model which explains these effects in terms of local heating of weak links and thermal instability.
4. Showing that such model yields a good agreement with the experiments.
5. Demonstrating for the first time that the coupling between the resonator and the feedline can be made amplitude dependent. Hence, allowing tuning the resonator into critical coupling conditions by means of varying the input power or varying the ambient temperature.

Furthermore, the fact that the onset of nonlinear effects in these NbN devices occurs at relatively low input power, typically 2-3 orders of magnitude lower than Nb for example, and the fact that these resonators have a "relatively" high T_c make these devices very attractive in practice.

5.1.2 Intermodulation Amplification

In addition to studying novel nonlinear dynamics in NbN superconducting resonators and revealing the underlying mechanism, we utilize this unique nonlinear response in order to demonstrate some novel applications. In particular, in our letter [63] we operate the resonator as an intermodulation amplifier and find that the gain can be as high as 15 dB for both the idler and the signal tones. To the best of our knowledge, intermodulation gain greater than unity has not been reported before in such systems.

Moreover, following our work a similar effect has been demonstrated by Tholen *et al.* [103] in superconducting coplanar resonators using kinetic inductance mechanism.

5.1.3 Stochastic Resonance

Manuscript [70] reports our experimental study of stochastic resonance in NbN superconducting microwave resonators. To the best of our knowledge SR phenomenon has not been demonstrated before in such devices. It has been heavily studied theoretically, but experimentally the applications considered are relatively few, mainly in, optical [104], analog [105, 106], rf-SQUIDs [107, 108], and nano-mechanical [109, 110] systems.

In addition, our study is novel and original at least in two more aspects: first, the underlying mechanism responsible for metastability in our devices, namely thermal instability is unique and different from other mechanisms studied earlier, second, the nonlinearity characterizing our devices is piecewise linear [111, 112] which is by far less discussed and investigated in the literature (compared to Duffing nonlinearity [71, 109, 110, 113] for instance). Moreover, following this study our group has succeeded also in demonstrating SR phenomenon in similar nonlinear devices with only one single metastable state [73].

Nevertheless, despite the differences listed above the main motivation in all these works is essentially the same, that is to amplify a small modulation signal acting on a metastable system (usually driven into metastability by an intense signal), with the aid of a certain amount of white noise. Thus, consequently achieving two goals, increasing the signal to noise ratio and making use of white noise which is generally considered as an undesired ingredient.

5.1.4 Escape Rate of Metastable States

In manuscript [72] we study both theoretically and experimentally the escape rate between metastable states of a NbN resonator originated by a thermal instability. Theoretically, we address the unique escape rate problem which involves two stochastic physical variables coupled together via their equations of motion, one is B the mode amplitude inside the resonator, and two is T the temperature of the hot spot. As a result of this coupling mechanism the model yields a finite correlation time for the heat power which controls the dynamics of T. To the best of our knowledge this result is new and has not been derived before. Whereas experimentally we utilize stochastic resonance measurements in order to extract the transition rates of the metastable states of the system by means of analyzing the statistics of the jump events. Furthermore, we compare between the experimental and theoretical results brought in the paper and show a partial agreement.

It is also worthwhile mentioning that additional experimental evidence for the validity of the escape rate equation derived theoretically in this paper has been independently provided in a subsequent work of our group Ref. [73] which involves studying SR phenomenon with only one single metastable state.

5.2 Nonlinear Dynamics in a Superconducting Resonator Integrated with a dc-SQUID

In this part of the research, we study unique nonlinear effects observed in superconducting stripline resonators integrated with dc-SQUIDs.

5.2.1 Intermodulation and parametric amplification

In our letter [101] we present intermodulation gain results obtained in a stripline resonator integrated with a dc-SQUID. We show that such system exhibits a signal gain of 24 dB and a phase modulation of 30 dB. In addition, when operated as a parametric amplifier, the device yields an abrupt rise of 38 dB in the generated side-band signal.

Furthermore, by inspecting Fig. 4 in the letter one can see two additional merits characterizing this amplifier: (1) It has a very narrow amplification

band with respect to the pump power. (2) It is ultra-sensitive in the vicinity of the critical power due to the large slope.

A brief comparison with other works

1. It is important to point out here an important difference in the amplification scheme of our device in comparison to the Josephson Bifurcation amplifier (JBA) reported in the papers of Siddiqi *et al.* [114, 115] [1]. The JBA is generally operated in the hysteretic regime and its output is a phase shift in the reflected signal rather than a power quantity. Hence, a straightforward gain comparison between the two schemes is not possible. (Nevertheless, toward the end of Ref. [114] the authors present a power gain expression $2\omega_p/\omega_s$ in the non-hysteretic regime where ω_p is the plasma frequency ($2\pi \times 1.8\,\mathrm{GHz}$) and ω_s is the signal frequency. However, the fact that ω_s is comparable to ω_s sets a boundary on the possible maximum gain.)

2. In the paper of T. Yamamoto *et al.* [83], where the authors have characterized a parametric amplifier consisting of a coplanar waveguide resonator terminated by a dc-SQUID, a maximum gain of 17 dB has been reported.

3. In the paper of M. A. Castellanos-Beltran *et al.* [84], where the authors have measured a JPA consisting of a coplanar-waveguide resonator whose inner conductor is replaced by an array of SQUIDs, a gain on the order of 18-21 dB in the non-degenerate ($f_s \neq f_p$) and the doubly degenerate ($f_s = f_p$) modes is reported while employing homodyne detection scheme. That is, in contrast to our 24 dB measured using a similar setup. The authors also report a maximum gain of 28 dB in a parametric amplification measurement.

4. In the paper of Yurke *et al.* [23], a gain of 17 dB has been measured in their JPA.

[1] The difference in the underlying mechanism is explained in the letter [101], in the paragraph which precedes the parametric amplification discussion in page 5.

Short explanation to the phase sensitive amplification

The dependence on the phase of the local oscillator that appears in Fig. 5 in the letter [101] can be explained as follows. The input signal contains two tones, the intense pump and the relatively weak signal. Due to the nonlinearity of the system frequency mixing occurs and consequently the output contains in addition the idler tone. Obviously, the phase of the idler is strongly correlated with the phase of the signal. This output signal is mixed using a mixer with a local oscillator having the same frequency as the pump, and having an adjustable phase. The down-converted pump tone contributes to the dc in the IF port of the mixer, whereas both the signal and the idler contribute to the component at frequency δ. However, the way in which these two phasors add depends on the phase of the local oscillator. This phase can be tuned such that these two tones add constructively, and consequently the largest output is obtained. Changing the phase of the local oscillator by $\pi/2$ from that point results in destructive interference, and consequently the smallest output is obtained. This behavior is seen in Fig. 5 in the paper.

5.2.2 Noise-induced spikes in the time domain

Studying the system response in the time domain near the intermodulation amplification threshold reveals a unique noise-induced spikes behavior. To account for the temporal response of the system we solved numerically the equations of motion for the integrated system, and present theoretical simulations which exhibit a good agreement with the experimental data (see Fig. 6 and Fig. 7 in the letter [101]).

Bibliography

[1] R. B. Hammond, E. R. Soares, Balam A. Willemsen, T. Dahm, D. J. Scalpino and J. R. Schrieffer, "Intrinsic limits on the Q and intermodulation of low power high temperature superconducting microstrip resonators", J. Appl. Phys. 84, 5662 (1998).

[2] T. P. Orlando and K. A. Delin, Foundations of Applied Superconductivity, Addison Wesley, 1991.

[3] G. J. Chen, P. A. Rosenthal and M. R. Beasley, "Kinetic Inductance Memory Cell", IEEE Trans. Appl. Supercond. 2, 95 (1995).

[4] R. Sobolewski, A. Verevkin, G. N. Gol'tsman, A. Lipatov and K. Wilsher, "Ultrafast Superconducting single-photon optical detectors and their applications", IEEE Trans. Appl. Supercond. 13, 2 (2003).

[5] Z. -Y. Shen, C. Wilker, P. Pang, W. L. Holstein, D. Face and D. J. Kountz, "High T_c superconductor-sapphire microwave resonator with Extremely high Q-values up to 90 K", IEEE Trans. Microwave Theory Tech. 40, 2424 (1992).

[6] C. Wilker, Z-Y. Shen and M. S. Brenner, "A sapphire resonator for microwave characterization of superconducting thin films", IEEE Trans. Appl. Supercond. 3, 1457 (1992).

[7] D. E. Oates, G. F. Dionne, D. H. Temme, J. A. Weiss, "Superconductor Ferrite Phase Shifters and Circulators", IEEE Trans. Appl. Supercond. 7, 2347 (1997).

[8] J. M. Pond, J. H. Claassen and W. L. Carter, "Kinetic inductance microstrip delay lines", IEEE Trans. Magn. 23, 903 (1987).

[9] S. M. Anlage, H. J. Snortland and M. R. Beasley, "A current controlled variable delay superconducting transmission line", IEEE Trans. Magn. 25 (2), 1388 (1989).

[10] C. Benvenuti, N. Circelli and M. Hauer, "Niobium films for superconducting accelerating cavities", Appl. Phys. Lett. 45 (5), 583 (1984).

[11] S. Kosaka, A. Shoji, M. Ayoagi, F. Shinoki, S. Tahara, H. Ohigashi, H. Nakagawa, S. Takada and H. Hayakawa, "An integration of all refractory Josephson logic LSI circuit", IEEE Trans. Magn. 21, 102 (1985).

[12] S. Yano, Y. Tarutani, H. Mori, H. Yamada, M. Hirano and U. Kawabe, "Fabrication and characteristics of NbN-based Josephson junctions for LSI circuits", IEEE Trans. Magn. 23, 1472 (1987).

[13] L. H. Lee, S. M. Ali, W. G. Lyons, D. E. Oates and J. D. Goettee, "Analysis of superconducting transmission-line structures for passive microwave device applications", IEEE Trans. Appl. Supercond. 3, 2782 (1993).

[14] T. Dahm, D.J. Scalapino and B.A. Willemson , "Phenomenological Theory of Intermodulation in HTS resonarors and filters", J. Supercond. 12, 2 (1999).

[15] T. Dahm, D. J. Scalapino, "Analysis and optimization of intermodulation in High T_c superconducting microwave filter design", IEEE Trans. Appl. Supercond. 8 , 149 (1998).

[16] R. Schneider, R. Aidam, A. Zaitsev, J. Geerk, G. Limker, F. Ratzel, R. Smithey, "Resonators and filters made of YBaCuO thin films on sapphire wafers", Physica C 351, 21 (2001).

[17] A. M. Portis, H. Chaloupka, M. Jeck and A. Pischke, "Power-induced switching of an HTS microstrip patch antenna", Superconduct. Sci. & Technol. 4 (9), 436 (1991).

[18] S. Ohshima, K. D. Develos, K. Ehata, Md. I. Ali and M. Mukaida, "Fabrication of low surface resistance YBCO films and its application to microwave devices", Physica C 335, 207 (2000).

[19] U. Salz, St Hofschen and R. Schneider, "Power transmission behavior of coplanar superconducting waveguides", IEEE Trans. Appl. Supercond. 3, 2816 (1993).

[20] Y. Nakamura, Yu. A. Pashkin and J. S. Tsai, "Coherent control of macroscopic quantum states in a single-Cooper-pair box", Nature 398, 786 (1999).

[21] Yu. A. Pashkin, T. Yamamoto, O. Astaflev, Y. Nakamura, D.V. Averin ,and J. S. Tsal, "Quantum oscillations in two coupled charge qubits", Nature 421, 823 (2003).

[22] C. M. Caves, "Quantum limits on noise in linear amplifiers", Phys. Rev. D 26, 1817 (1982).

[23] B. Yurke, L. R. Corruccini, P. G. Kaminsky, L. W. Rupp, A. D. Smith, A. H. Silver, R. W. Simon and E. A. Whittaker, "Observation of parametric amplification and deamplification in a Josephson parameteric amplifier", Phys. Rev. A 39, 2519 (1989).

[24] R. Movshovich, B. Yurke, P. G. Kaminsky, A. D. Smith, A. H. Silver, R. W. Simon and M. V. Schneider, "Observation of zero-point noise squeezing via a Josephson-parametric amplifier", Phys. Rev. Lett. 65, 1419 (1990).

[25] J. Halbritter, "rf residual losses,surface impedance and granularity in superconducting cuprates", J. Appl. Phys. 68, 6315 (1990).

[26] J. Halbritter, "On extrinsic effects in the surface impedance of cuprate superconductors by weak links", J. Appl. Phys. 71, 339 (1992).

[27] M. A. Golosovsky, H. J. Snortland and M. R. Beasley, "Nonlinear microwave properties of superconducting Nb microstrip resonators", Phys. Rev. B. 51, 6462 (1995).

[28] J. S. Herd, D. E. Oates, and J. Halbritter, "Identification and Modeling of microwave loss mechanisms in $YBa_2Cu_3O_{7-x}$", IEEE Trans. Appl. Supercond. 7, 1299 (1997).

[29] J. C. Booth, S. A. Schima, and D. C. DeGroot, "Description of the nonlinear behavior of superconductors using a complex conductivity", IEEE Trans. Appl. Supercond. 13, 315 (2003).

[30] S. Isagawa, "rf superconducting properties of reactively sputtered NbN", J. Appl. Phys. 52, 921 (1980).

[31] Y. M. Shy, L. E. Toth, and R. Somasundaram, "Superconducting properties, electrical resistivities, and structure of NbN thin films", J. Appl. Phys. 44, 5539 (1973).

[32] Y. Saito, T. Anayama, Y. Moto, and Y. Onodera, "Anisotropies in the critical currents of NbN films", J. Appl. Phys. vol. 43, 3842 (1972).

[33] J. Wosik, L.-M. Xie, J. Mazierska and R. Grabovickic, "Influence of columnar defects on surface resistance of YBaCuO superconducting thin films;nonlinear effects", Appl. Phys. Lett. 75, 1781 (1999).

[34] T. L. Hylton, A. Kapitulnik, M. R. Beasley, J. P. Carini, L. Drabeck and G. Gruner, "Weakly coupled grain model of High-frequency losses in high T_c superconducting thin films", Appl. Phys. Lett. 53, 1343 (1988).

[35] P. P. Nguyen, D. E. Oates, G. Dresselhaus, and M. S. Dresselhaus, "Nonlinear surface impedance for $YBa_2Cu_3O_{7-x}$ thin films: Measurements and a coupled-grain model", Phys. Rev. B 48, 6400 (1993).

[36] J. S. Herd, D. E. Oates, H. Xin and S. J. Berkowitz, "Coupled-Grain/RSJ Series array for modeling of nonlinear microwave surface impedance of YBCO thin films", IEEE Trans. Appl. Supercond. 9, 2117 (1999).

[37] D. E. Oates, P. P. Nguyen, Y. Habib, G. Dresselhaus, M. S. Dresselhaus, G. Koren and E. Polturak, "Microwave power dependence of $YBa_2Cu_3O_7$ thin-film Josephson edge junctions", Appl. Phys. Lett. 68, 705 (1996).

[38] Y. M. Habib, D. E. Oates, G. Dresselhaus, M. G. Dresselhaus, "Power dependence of microwave Z_s in High-T_c Josephson junctions: measurements and modeling", IEEE Trans. Appl. Supercond. 7, 2553 (1997).

[39] D. E. Oates, H. Xin, G. Dresselhaus, and M. S. Dresselhaus, "Intermodulation distortion and josephson vortices in YBCO Bicrystal grain boundary", IEEE Trans. Appl. Supercond. 11, 2804 (2001).

[40] S. K. Yip and J. A. Sauls, "Nonlinear meissner effect in CuO Superconductors", Phys. Rev. Lett. 69, 2264 (1992).

[41] T. Dahm and D. J. Scalapino, "Theory of intermodulation in a superconducting microstrip resonator", J. Appl. Phys. 81, 2002 (1997).

[42] T. Dahm and D. J. Scalpino, "Nonlinear current response of a d-wave superfluid", Phys. Rev. B 60, 13125 (1999).

[43] D. E. Oates,S. -H. Park and G. Koren, "Observation of the nonlinear Meissner effect in YBCO thin films: Evidence for a d-wave order parameter in the bulk of the curprates superconductors", Phys. Rev. Lett. 93, 197001 (2004).

[44] J. Halbritter, "Change of eigenstate in a superconducting rf cavity due to a nonlinear response", J. Appl. Phys. 41, 4581 (1970).

[45] J. H. Oates, R. T. Shin, D. E. Oates, M. J. Tsuk, and P. P. Nguyen, "A nonlinear transmission line model for superconducting stripline resonators", IEEE Trans. Appl. Superconduct. 3, 17 (1993).

[46] C.-W. Lam, D. M. Sheen, S. M. Ali and D. E. Oates, "Modeling the nonlinearity of superconducting strip transmission lines", IEEE Trans. Appl. Supercond. 2, 58 (1992).

[47] L. F. Cohen, A. L. Cowie, A. Purnell, N. A. Lindop, S. Thiess and J C Gallop, "Thermally induced nonlinear behavior of HTS films at high microwave power", Supercond. Sci. and Technol. 15, 559 (2002).

[48] A. L. Karuzskii, A. E. Krapivka, A. N. Lykov, A. V. Perestoronin, and A. I. Golovashkin, "Microwave nonlinear effects in He-cooled superconducting microstrip resonators", Physica B 329-333, 1514 (2003).

[49] C. C. Chen, D. E. Oates, G. Dresselhaus, M. S. Dresselhaus, "Nonlinear electrodynamics of superconducting NbN and Nb thin films at microwave frequencies", Phys. Rev. B 45, 4788.

[50] Z. Ma, E. D. Obaldia, G. Hampel, P. Polakos, P. Mankiewich, B. Batlogg, W. Prusseit, H. Kinder, A. Anderson, D. E. Oates, R. Ono, and J. Beall, "RF power dependence study of large area YBCO thin films", IEEE Trans. Appl. Supercond. 7, 1911 (1997).

[51] J. Wosik, L.-M. Xie, J. H. Miller,Jr., S. A. Long, and K. Nesteruk, "Thermally-induced nonlinearities in the surface impedance of superconducting YBCO thin films", IEEE Trans. Appl. Supercond. 7, 1470 (1997).

[52] B. A. Willemsen, J. S. Derov, J. H. Silva, S. Sridhar, "Nonlinear response of suspended high temperature superconducting thin film microwave resonators", IEEE Trans. Appl. Supercond. 5, 1753 (1995).

[53] D.E. Oates, M. A. Hein, P. J. Hirst, R. G. Humphreys, G. Koren and E. Polturak, "Nonlinear microwave surface impedance of YBCO films: latest results and present understanding", Physica C 372-376, 462 (2002).

[54] D. E. Oates, S.-H. Park, M. A. Hein, P. J. Hirst, and R. G. Humphreys, "Intermodulation distribution and third-harmonic generation in YBCO films of varying oxygen content", IEEE Trans. Appl. Supercond. 13, 311 (2003).

[55] A. P. Zhuravel, A. V. Ustinov, K. S. Harshavardhan, and S. M. Anlage, "Influence of $LaAlO_3$ surface topography on rf current distribution in superconducting microwave devices", Appl. phys. Lett. 81, 4979 (2002).

[56] A. V. Velichko, D. W. Huish, M. J. Lancaster, and A. Porch, "Anomalies in nonlinear microwave surface impedance of YBCO thin films on MgO: Superconductor versus substrate effects", IEEE Trans. Appl. Supercond. 13, 3598 (2003).

[57] D. W. Facem, C. Wilker, J. J. Kingston, Z.-Y. Shen, F. M. Pellicone, R. J. Small, S. P. McKenna, S. Sun, and P. J. Martin, "Advances in HTS films for High Power Microwave applications", IEEE Trans. Appl. Supercond. 7, 1283 (1997).

[58] S. Ohshima, K. D. Develos, K. Ehata, Md. I. Ali, M. Mukaida, "Fabrication of law surface resistance YBCO films and its application to microwave devices", Physica C 335, 207 (2000).

[59] S. J. Hedges, M. J. Adams and B. F. Nicholson, "Power dependent effects observed for a superconducting stripline resonator", Elect. Lett. 26, 14 (1990).

[60] J. Wosik, L.-M. Xie, R. Grabovickic, T. Hogan and S. A. Long, "Microwave power handling capability of HTS superconducting thin films: weak links and thermal effects induced limitation", IEEE Trans Appl. Supercond. 9, 2456 (1999).

[61] B. Abdo, E. Segev, O. Shtempluck, and E. Buks, "Observation of bifurcations and hysteresis in nonlinear NbN superconducting microwave resonators", IEEE trans. on appl. superconduct. 16, 1976 (2006).

[62] B. Abdo, E. Segev, O. Shtempluck, and E. Buks, "Nonlinear dynamics in the resonance lineshape of NbN superconducting resonators", Phys. Rev. B 73, 134513 (2006).

[63] B. Abdo, E. Segev, O. Shtempluck, and E. Buks, "Intermodulation gain in nonlinear NbN superconducting microwave resonators", Appl. Phys. Lett. 88, 022508 (2006).

[64] E. Segev, B. Abdo, O. Shtempluck, and E. Buks, "Fast resonance Frequency Modulation in Superconducting Stripline Resonator", IEEE trans. on applied superconduct. 16, 1943 (2006).

[65] E. Segev, B. Abdo, O. Shtempluck, and E. Buks, "Extreme nonlinear phenomena in NbN superconducting stripline resonators", Phys. Lett. A 366, 160 (2007).

[66] E. Segev, B. Abdo, O. Shtempluck, and E. Buks, "Thermal instability and self-sustained modulation in superconducting NbN stripline resonators", J. Phys.: Condens. Matter 19, 096206 (2007).

[67] E. Segev, B. Abdo, O. Shtempluck, and E. Buks, "Novel self-sustained modulation in superconducting stripline resonators", EuroPhys. Lett. 78, 57002 (2007).

[68] R. Monaco, A. Andreone and F. Palomba, "Intermodulation measurements in Nb superconducting microstrip resonators", J. Appl. Phys. 88, 5 (2000).

[69] B. Yurke and E. Buks, "Performance of Cavity-Parametric Amplifiers, Employing Kerr Nonlinearites, in the Presence of Two-Photon Loss", J. Lightwave Technol. 24, 5054 (2006).

[70] B. Abdo, E. Segev, O. Shtempluck, and E. Buks, "Signal amplification in NbN superconducting resonators via Stochastic Resonance", Phys. Lett. A 370, 449 (2007).

[71] L. Gammaitoni, P. Hänggi, P. Jung, F. Marchesoni, "Stochastic resonance", Rev. Mod. Phys. 70, 223 (1998).

[72] B. Abdo, E. Segev, O. Shtempluck, and E. Buks, "Escape rate of metastable states in a driven NbN superconducting microwave resonator", J. Appl. Phys. 101, 083909 (2007).

[73] E. Segev, B. Abdo, O. Shtempluck, and E. Buks, "Stochastic resonance with a single metastable state: Thermal instability in NbN superconducting stripline resonators", Phys. Rev. B 77, 012501 (2008).

[74] P. Hänggi, H. Grabert, G. L. Ingold and U. Weiss, "Quantum theory of activated events in presence of long-time memory", Phys. Rev. Lett. 55, 761 (1985);

[75] M. Grifoni and P. Hänggi, "Nonlinear quantum stochastic resonance", Phys. Rev. E 54, 1390 (1996); M. Grifoni, and P. Hänggi, "Coherent and incoherent quantum stochastic resonance", Phys. Rev. Lett. 76, 1611 (1996).

[76] Á. Rivas, N. P. Oxtoby, and S. F. Huelga, "Stochastic resonance phenomena in qubit arrays", quant-ph/0901.1791v1 (2009).

[77] P. Hänggi, P. Talkner and M. Borkovec, "Reaction-rate theory: fifty years after Kramers", Rev. Mod. Phys. 62, 251 (1990).

[78] T. A. Fulton and L. N. Dunkleberger, "Lifetime of the zero-voltage state in Josephson tunnel junctions", Phys. Rev. B 9, 11 (1974).

[79] M. Devoret, D. Esteve, J. M. Martinis, A. Cleland and J. Clarke, "Resonant activation of a Brownian particle out of a potential well: microwave-enhanced escape from the zero-voltage state of a Josephson junction", Phys. Rev. B 36, 58 (1987).

[80] B. Yurke, P. G. Kaminsky, R. E. Miller, E. A. Whittaker, A. D. Smith, A. H. Silver and R. W. Simson, "Observation of 4.2K equilibrium noise squeezing via a Josephson-parametric amplifier", IEEE Trans. Mag. 25, 1371 (1989).

[81] B. Yurke, M. L. Roukes, R. Movshovich and A. N. Pargellis, "A low-noise series-array Josephson junction parametric amplifier", Appl. Phys. Lett. 69, 3078 (1996).

[82] L. Spietz, K. Irwin and J. Aumentado, "Input impedance and gain of a gigahertz amplifier using a dc-SQUID in a quarter wave resonator", Appl. Phys. Lett. 93, 082506 (2008).

[83] T. Yamamoto., K. Inomata, M. Watanabe, K. Matsuba, T. Miyazaki, W. D. Oliver, Y. Nakamura, and J. S. Tsai, "Flux-driven Josephson parametric amplifier", Appl. Phys. Lett. 93, 042510 (2008).

[84] M. A. Castellanos-Beltran and K. W. Lehnert, "Widely tunable parametric amplifier based on a superconducting quantum interference device array resonator", Appl. Phys. Lett. 91, 83509 (2007).

[85] M. A. Castellanos-Beltran, K. D. Irwin, G. C. Hilton, L. R. Vale and K. W. Lehnert, "Amplification and squeezing of quantum noise with a tunable Josephson metamaterial", Nat. Phys. 4, 929 (2008).

[86] A. A. Abdumalikov, Jr, O. Astafiev, Y. Nakamura, Y. A. Pashkin and J. Tsai, "Vacuum Rabi splitting due to strong coupling of a flux qubit and a coplanar-waveguide resonator", Phys. Rev. B 78, 180502(R) (2008).

[87] E. Buks *et al.* unpublished results.

[88] T. Lindstrom, C. H. Webster, J. E. Healey, M. S. Colclough, C. M. Muirhead and A. Ya Tzalenchuk, "Circuit QED with a flux qubit strongly coupled to a coplanar transmission line resonator", Supercond. Sci. Technol. 20, 814 (2007).

[89] M.-Yu Chen, M. W. Y. Tu and W.-Min Zhang, "Entangling two superconducting LC coherent modes via a superconducting flux qubit", quant-ph/ 0809.0749 (2008).

[90] E. Buks and B. Yurke, "Dephasing due to intermode coupling in superconducting stripline resonators", Phys. Rev. A 73, 023815 (2006).

[91] H. Wang, M. Hofheinz, M. Ansmann, R. C. Bialczak, E. Lucero, M. Neeley, A. D. O'Connell, D. Sank, J. Wenner, A. N. Cleland and J. M.

Martinis, "Generation of Fock states in a superconducting quantum circuit", Nature 454, 310 (2008).

[92] Oren Suchoi, Baleegh Abdo, Eran Segev, Oleg Shtempluck, Miles Blencowe and Eyal Buks, "Intermode dephasing in a superconducting stripline resonator", cond-mat/0901.2865v1, submitted to Physical Review Letters.

[93] R. K. Hoffman, *Handbook of microwave integrated circuits*, Artech House, Norwood,1987.

[94] A. Fukushima, A. Sato, A. Iwasa, Y. Nakamura, T. Komatsuzaki, and Y. Sakamato, "Attenuation of microwave filters for single-electron tunneling experiments", IEEE Trans. Instrum. Meas. 46, 289 (1997).

[95] D. Vion, P. F. Orfila, P. Joyez, D. Esteve, and M. H. Devoret, "Miniature electrical filters for single electron devices", J. Appl. Phys. 77, 2519 (1995).

[96] R. C. Richardson and E. N. Smith, *Experimental techniques in condensed matter physics at low temperatures*, Addison-Wesley 1998.

[97] Z. Wang, A. Kawakami, Y. Uzawa, and B. Komiyama, "Superconducting properties and crystal structures of single-crystal niobium nitride thin films deposited at ambient substrate temperature", J. Appl. Phys. 79, 7837 (1996).

[98] D. D. Bacon, A.T. English, S. Nakahara, F. G. Peters, H. Schreiber, W. R. Sinclair, and R. B. van Dover, "Properties of NbN thin films deposited on ambient temperature substrates", J. Appl. Phys. 54, 6509 (1983).

[99] S. Thakoor, J. L. Lamb, A. P. Thakoor and S. k. Khanna, "High T_c superconducting NbN films deposited at room temperature", J. Appl. Phys. 58, 4643 (1985).

[100] P. Yagoubov, G. Gol'tsman, B. Voronov, L. Seidman, V. Siomash, S. Cherednichenko and E. Gershenzon, "The bandwidth of HEB mixers employing ultrathin NbN films on sapphire substrate", Seventh International Symposium on Space Terahertz Technology, Charlottesville 290 (1996).

[101] Baleegh Abdo, Oren Suchoi, Eran Segev, Oleg Shtempluck, Miles Blencowe and Eyal Buks, "Intermodulation and parametric amplification in a superconducting stripline resonator integrated with a dc-SQUID", Europhys. Lett. 85, 68001 (2009).

[102] T. A. Fulton and G. J. Dolan, "Observation of single-electron charging effects in small tunnel junctions", Phys. Rev. Lett. 59, 109 (1987).

[103] E. A. Tholen, A. Ergül, E. M. Doherty, F. M. Weber, F. Grégis and D. B. Haviland, "Nonlinearities and parametric amplification in superconducting coplanar waveguide resonators", Appl. Phys. Lett. 90, 253509 (2007).

[104] B. McNamara, K. Wiesenfeld, and R. Roy, "Observation of stochastic resonance in a ring laser", Phys. Rev. Lett. 60, 2626 (1988).

[105] S. Fauve and F. Heslot, "Stochastic resonance in a bistable system", Phys. Lett. A 97, 5 (1983).

[106] Ting Zhou and Frank Moss, "Analog simulations of stochastic resonance", Phys. Rev. A 41, 4255 (1990).

[107] A. D. Hibbs, A. L. Singsaas, E. W. Jacobs, A. R. Bulsara, J. J. Pekkedahl, and F. Moss, "Stochastic resonance in superconducting loop with a Josephson junction", J. Appl. Phys. 77, 2582 (1995).

[108] R. Rouse, S. Han, and J. E. Lukens, "Flux amplification using stochastic superconducting quantum interference devices", Appl. Phys. Lett. 66, 108 (1995).

[109] R. L. Badzey and P. Mohanty, "Coherent signal amplification in bistable nanomechanical oscillators by stochastic resonacne", Nature 437, 995 (2005).

[110] R. Almog, S. Zaitsev, O. Shtempluck and E. Buks, "Signal amplification in a nanomechanical Duffing resonator via stochastic resonance", Appl. Phys. Lett. 90, 013508 (2007).

[111] M. Bier and R. D. Astumian, "Matching a diffusive and a kinetic approach for escape over a fluctuating barrier", Phys. Rev. Lett. 71, 1649 (1993).

[112] M. Bier and R. D. Astumian, "What is adiabaticity? suggestions from a fluctuating linear potential", Phys. Lett. A 247, 385 (1998).

[113] H. B. Chan and C. Stambaugh, "Fluctuation-enhanced frequency mixing in a nonlinear micromechanical oscillator", Phys. Rev. B 73, 224301 (2006).

[114] I. Siddiqi, R. Vijay, F. Pierre, C. M. Wilson, M. Metcalfe, C. Riggetti, L. Frunzio, and M. H. Devoret, "RF-driven Josephson bifurcation amplifier for quantum measurement", Phys. Rev. Lett. 93, 207002 (2004).

[115] I. Siddiqi, R. Vijay, F. Pierre, C. M. Wilson, L. Frunzio, M. Metcalfe, C. Riggetti, R. J. Schoelkopf, M. H. Devoret, D. Vion and D. Esteve, "Direct observation of dynamical bifurcation between two driven oscillation states of a Josephson junction", Phys. Rev. Lett. 94, 027005 (2005).

דינמיקה לא ליניאריות במהודים על מוליכים והתקני התאבכות

בליר' עבדו

דינמיקה לא ליניאריות במהודים על מוליכים והתקני התאבכות

חיבור על מחקר

לשם מילוי חלקי של הדרישות לקבלת התואר
דוקטור לפילוסופיה

בליר' עבדו

הוגש לסנט הטכניון- מכון טכנולוגי לישראל
אייר תשס''ט חיפה מאי 2009

המחקר נעשה בהנחיית פרופ' אייל בוקס בפקולטה להנדסת חשמל

אני מודה לטכניון ולמשרד המדע התרבות והספורט על התמיכה
הכספית הנדיבה בהשתלמותי

תקציר

נושא המחקר הינו דינאמיקה לא ליניארית של מהודים על-מוליכים אשר מצומדים לאלמנטים לא ליניאריים כגון: נקודות חלשות (weak-links), מיקרו-גשרים (micro-bridges) והתקני התאבכות (SQUIDs).

הבנת המנגנונים והגורמים הפיסיקליים שעומדים מאחורי האפקטים הלא ליניאריים בעל-מוליכים בתחום המיקרוגל, הינו נושא שזוכה למחקרים אינטנסיביים ולתשומת לב מדעית מוגברת בשל חשיבותו הרבה, הן מהבחינה המעשית והן מהבחינה התיאורטית. מהבחינה המעשית זיהוי הגורמים הפיסיקליים שאחראים להופעת תופעות לא ליניאריות בעל-מוליכים ולהתגברותם תאפשר שליטה והקטנה יזומה של האפקטים הללו למינימום ברכיבי מיקרוגל פסיביים שממומשים בעזרת על-מוליכים כמו מסננים וקווי תמסורת, ושסובלים מירידה חדה בביצועים בהספקים בינוניים יחסית בגלל התגברות האפקטים הלא ליניאריים. מהבחינה התיאורטית הבנה כזו תאפשר הבנה עמוקה יותר של תופעת העל-מוליכות בתחום המיקרוגל, וגם תאפשר לפי ניסויים וחישובים שונים שנעשו בשנים האחרונות לנצל את האפקטים הללו למימוש מספר אפליקציות לא ליניאריות כגון: (1) מגבר פרמטרי שרגיש לפאזה שיש לו את הפוטנציאל ליצור מצבים קוונטים מיוחדים שנקראים Squeezed States של השדה האלקטרומגנטי. (2) מגבר פרמטרי בעל רעש נמוך שיאפשר לקרוא את המצב הקוונטי של קיוביט (Qubit) שהינו אבן הבניין הבסיסי למימוש מחשב קוונטי או לחילופין לאפשר מדידה מאוד רגישה של אופני תנודה של קורות ננו-מכאניות. (3) להציג Dephasing של פוטונים באחד המודים של רזונטורים על-מולכים בתחום המיקרוגל תוך שימוש בצימוד לא ליניארי למוד אחר.

במסגרת המחקר הזה, בניגוד לרוב העבודות בתחום המעשי, לא נעשה מאמץ להקטין את האפקטים הלא-ליניאריים בעל-מוליכים, אלא להיפך חיפשנו דרכים להגביר אותם, במטרה אולי לממש בעתיד את אחת האפליקציות הלא-ליניאריות, שהוזכרו לעיל.

בחלק הראשון של המחקר חקרנו אפקטים לא ליניאריים חזקים ומפתיעים שנמדדו ברזונטורים על-מוליכים העשויים מ- Niobium Nitride (NbN) אשר מצומדים לנקודות חלשות ומיקרו-גשרים.

הרזונטורים מומשו בגיאומטריית סטרפליין (Stripline) על מצעי ספייר (Sapphire) באמצעות תהליך פוטוליתוגרפיה ואיכול פלזמה. ואילו הנקודות החמות ברזונטורים נוצרו באופן ספונטני מסביב למבנה העמודות של NbN או שנוצרו בצורה מתוכננת על ידי איכול בעזרת Focused ion beam (FIB). הרזונטורים קוררו על ידי שימוש בהיליום נוזלי ונמדדו בטווח הטמפרטורות 12 K - 4.

התופעות הלא-לינאריות שנמדדו ברזונטורים האלו בהספקים נמוכים יחסית כללו בין היתר: קפיצות חדות ופתאומיות בשני צידי עקומות התהודה, הזזות תדר, לולאות חשל (hysteresis) בשני צידי עקומות התהודה כפונקציה של התדר, לולאות חשל שמשנות כיוון עם הגדלת הספק הכניסה, רגישות לרעש ליד הקפיצות, צימוד קריטי, אזורי אי-יציבות (Astability), אוסילציות או מודולציות עצמיות באזור הלא-יציב (Astable).

המודל התיאורטי ששימש אותנו להסברת התופעות הנ"ל עם התאמה די טובה לתוצאות הניסוי כלל בעיקר שתי משוואות דיפרנציאליות מצומדות: משוואת תנועה עבור המעטפת האיטית של אמפליטודת המוד בתוך הרזונטור B, ומשוואת חום עבור הטמפרטורה T של הנקודה החמה בתוך הרזונטור. כאשר הצימוד בין שתי המשוואות נובע מהפרמטרים של הרזונטור (תדר התהודה וקבועי הצימוד לאמבט ולקו-כניסה) ושתלויים בטמפרטורה T של הנקודה החמה בצורת מדרגה.

יתר על כן, מאחר והמערכת הלא-ליניארית שלנו הינה מיטאסטבילית (metastable) מסוג מיוחד שידוע בשם "ליניארי בחלקים" (piecewise linear) קיימת חשיבות רבה למדידה וחישוב קצב המעבר (escape rate) בין המצבים המיטאסטביליים של המערכת או לחילופין זמן החיים (lifetime) של המצבים הללו. ועל כן במסגרת העבודה שלנו פיתחנו משוואה תיאורטית למציאת קצב המעבר בין מצבים מיטאסטביליים, ומצאנו התאמה די טובה לתוצאות הניסוי.

בנוסף, הצלחנו לנצל את האי-ליניאריות החזקה בהתקנים שלנו כדי להדגים שני מנגנוני הגברה: (1) הגברת אינטר-מודולציה (intermodulation amplification), שבמסגרתה מוזרקים לתוך הרזונטור שני סיגנלים קרובים בתדר, אחד חזק pump ואחד חלש signal ומראים איך בתחום הלא-לינארי של הרזונטור בנוסף להיווצרות סיגנל idler כתוצאה מערבוב תדרים, מתקבל הגבר חיובי גבוה בכ-15 dB גם ב- idler וגם ב- signal, וזאת קרוב לנקודות קפיצה של ה-pump. (2) הגברת אות מודולציה מחזורי חלש על ידי עירור הרזונטור לתוך תחום מיטאסטבילי והזנת המערכת ברעש לבן "בינוני" בכניסה, מה שידוע בשפה המדעית כתופעת תהודה סטוכסטית (stochastic resonance).

בחלק השני של המחקר חקרנו אפקטים לא ליניאריים ייחודיים ברזונטורים על-מוליכים העשויים מאלומיניום אשר מצומדים להתקני התאבכות מסוג (dc-SQUIDs).

ההתקנים האלו יוצרו על גבי מצעי סיליקון בעלי התנגדות גבוהה בעזרת ליתוגרפיית אלקטרונים (e-beam lithography), ונידוף אלומיניום בזווית (angle shadow evaporation) , כולל שלב ביניים של חמצון לשם יצירת צמתי-הג'וספסון (Josephson junctions) של ה-dc-SQUID בתוך הרזונטור.

לצורך מדידת ההתקנים האלו שעשויים מאלומיניום ושמאופיינים על ידי טמפרטורה קריטית נמוכה (קרובה ל- 1 K) ושרגישים לרעש, נעשה שימוש במקרר dilution במעבדה שלנו שמאפשר מדידת דגמים בטמפרטורת בסיס של 30 mK. כמו כן נעשה מאמץ גדול במהלך התכנון של מערך הניסוי ומימושו במטרה להגדיל את הצימוד התרמי בין רכיבי המיקרוגל לדרגות הקירור השונות, וכדי למזער כמה שניתן את הרעשים האלקטרומגנטיים והתרמיים המגיעים מטמפרטורת החדר ולסנן אותם.

יתר על כן, בדומה לרזונטורים הלא-לינאריים מ-NbN הצלחנו להפעיל את המערכת המשולבת שלנו (מהוד-dc-SQUID) כמגבר אינטר-מודולציה עם הגבר signal של כ- 24 dB קרוב להספק הקריטי של ה-pump (ההספק שבו מופיעים האפקטים הלא-ליניאריים ונמדד הגבר אינטר-מודולציה), כאשר הפעם ה- dc-SQUID הוא שמתפקד כאלמנט לא-ליניארי במערכת. כמו כן הראינו שהמגבר הנ"ל מפגין רגישות לפאזה

במדידת homodyne, ומודולציית פאזה של עד 30 dB. בנוסף הראינו שההתקן המשולב הנ"ל ניתן להפעילו כמגבר פרמטרי שמראה עלייה גדולה וסימולטנית בהרמוניות שמתאימות להפרש התדרים בין ה-signal ל-pump. וזאת בהספק סף מסוים של ה-pump שבאופן שונה ממדידת אינטר-מודולציה הינו בעל תדר כפול מתדר התהודה ומשודר לתוך קו-שטף (flux-line) (המצומד ל-dc-SQUID), ולא דרך קו-כניסה (feedline) של המהוד.

תוצאות חשובות ומעניינות נוספות שראויות לציון התקבלו במערכת המשולבת שלנו גם בתחום הזמן. במדידות שעשינו כפונקציה של הזמן, במקביל לאינטר-מודולציה, מצאנו שהמערכת המשולבת עוברת בכמה מצבים וזאת כאשר סורקים את הספק ה-pump בסביבת ההספק הקריטי: (1) עבור הספק pump שנמוך משמעותית מהספק הסף סיגנל היציאה של מערך ה-homodyne הינו קבוע כתלות בזמן. (2) עבור הספק שמתקרב להספק הסף, קפיצות וספייקים (spikes) אקראיים בסיגנל היציאה מתחילים להופיע. (3) עבור הספקים מספיק קרובים להספק הסף הקפיצות האקראיות מתחילות להצטופף לקבוצות הולכות וגדלות. (4) עבור הספק שמתאים להספק הסף ולשיא בהגבר האינטר-מודולציה קצב ההצטופפות (והספייקים) מגיע לאופטימום. ואילו בשלב האחרון (5) עבור הספקי pump שגדולים מההספק הקריטי קצב הספייקים מגיע לרוויה ונמדדת ירידה סימולטנית בהגבר האינטר-מודולציה.

בניסיון להסביר את התופעות הנ"ל בתחום הזמן אנו ממדלים את הרזונטור כמעגל RLC טורי בעל תדר תהודה ועקבה אופיינית (characteristic impedance) זהים לזה של הרזונטור. את ה-dc-SQUID המחובר לרזונטור אנו מתארים באמצעות שתי משוואות תנועה כולל רעש, משוואה אחת עבור כול אחד מהצמתים של ה-dc-SQUID. ואילו את הצימוד ביניהם אנו מייצגים בעיקר בעזרת זרם rf שזורם דרכו. סימולציות שנעשו לפי המודל הנ"ל הניבו תוצאות טובות, ושיחזרו בהצלחה את המאפיינים והמצבים העיקריים של תגובת המערכת המשולבת בתחום הזמן.